

Numerical Study of Two-Dimensional Flows of Nanofluids



By

Zahid Ahmed

*Department of Mathematics
Quaid-I-Azam University
Islamabad, Pakistan
2020*

Numerical Study of Two-Dimensional Flows of Nanofluids



By

Zahid Ahmed

Supervised By

Prof. Dr. Sohail Nadeem

*Department of Mathematics
Quaid-I-Azam University
Islamabad, Pakistan
2020*

Numerical Study of Two-Dimensional Flows of Nanofluids



By

Zahid Ahmed

A THESIS SUBMITTED IN THE PARTIAL FULFILLMENT OF THE REQUIREMENT FOR

THE DEGREE OF

DOCTOR OF PHILOSOPHY

IN

MATHEMATICS

Supervised By

Prof. Dr. Sohail Nadeem

Department of Mathematics

Quaid-I-Azam University

Islamabad, Pakistan

2020

Certificate of Approval

This is to certify that the research work presented in this thesis entitled **Numerical Study of Two-Dimensional Flows of Nanofluids** was conducted by Mr. **Zahid Ahmed** under the kind supervision of **Prof. Dr. Sohail Nadeem**. No part of this thesis has been submitted anywhere else for any other degree. This thesis is submitted to the Department of Mathematics, Quaid-i-Azam University, Islamabad in partial fulfillment of the requirements for the degree of Doctor of Philosophy in field of Mathematics from Department of Mathematics, Quaid-i-Azam University Islamabad, Pakistan.

Student Name: **Zahid Ahmed**

Signature: 


External committee:

a) **External Examiner 1:**

Name: **Prof. Dr. Rahmat Ellahi**

Designation: Professor

Office Address: Department of Mathematics, International Islamic University, Islamabad.

Signature: 

b) **External Examiner 2:**

Name: **Dr. Noreen Sher Akbar**

Designation: Associate Professor

Office Address: National University of Sciences and Technology, Islamabad.

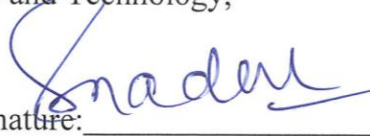
Signature: 

c) **Internal Examiner**

Name: **Prof. Dr. Sohail Nadeem**

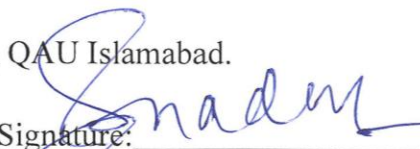
Designation: Professor

Office Address: Department of Mathematics, QAU Islamabad.

Signature: 

Supervisor Name:

Prof. Dr. Sohail Nadeem

Signature: 

Name of Dean/ HOD

Prof. Dr. Sohail Nadeem

Signature: 

Numerical Study of Two-Dimensional Flows of Nanofluids

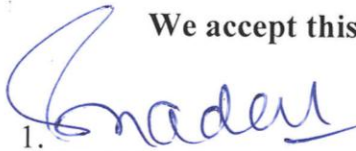
By

Zahid Ahmed

CERTIFICATE

A THESIS SUBMITTED IN THE PARTIAL FULFILLMENT OF THE
REQUIREMENTS FOR THE DEGREE OF THE
DOCTOR OF PHILOSOPHY IN MATHEMATICS

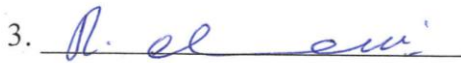
We accept this thesis as conforming to the required standard

1. 

Prof. Dr. Sohail Nadeem
(Chairman)

2. 

Prof. Dr. Sohail Nadeem
(Supervisor)

3. 

Prof. Dr. Rahmat Ellahi
(External Examiner)

4. 

Dr. Noreen Sher Akbar
(External Examiner)

Department of Mathematics, International
Islamic University, Islamabad.

National University of Sciences and
Technology, Islamabad

Department of Mathematics
Quaid-I-Azam University
Islamabad, Pakistan

2020

Author's Declaration

I, **Zahid Ahmed**, hereby state that my PhD thesis titled **Numerical Study of Two-Dimensional Flows of Nanofluids** is my own work and has not been submitted previously by me for taking any degree from the Quaid-I-Azam University Islamabad, Pakistan or anywhere else in the country/world.

At any time if my statement is found to be incorrect even after my graduation, the university has the right to withdraw my PhD degree.



Name of Student: **Zahid Ahmed**

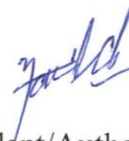
Date: **04-June-2020**

Plagiarism Undertaking

I solemnly declare that research work presented in the thesis titled “**Numerical Study of Two-Dimensional Flows of Nanofluids**” is solely my research work with no significant contribution from any other person. Small contribution/help wherever taken has been duly acknowledged and that complete thesis has been written by me.

I understand the zero tolerance policy of the HEC and **Quaid-i-Azam University** towards plagiarism. Therefore, I as an Author of the above titled thesis declare that no portion of my thesis has been plagiarized and any material used as reference is properly referred/cited.

I undertake that if I am found guilty of any formal plagiarism in the above titled thesis even afterward of PhD degree, the University reserves the rights to withdraw/revoke my PhD degree and that HEC and the University has the right to publish my name on the HEC/University Website on which names of students are placed who submitted plagiarized thesis.



Student/Author Signature

Name: **Zahid Ahmed**

Dedication

*I would like to dedicate this thesis to my late grandfather **Mr. Abdul Wahid**. A teacher of my life. Baba taught me to own myself, carved a path of living that is a valued response to social norms and responsibilities with self-dignity. He would share it open-heartedly when happy and stay calm and peaceful when life is not easy.*

Acknowledgment

*I would like to express my heartiest gratitude to my research supervisor and mentor **Prof. Dr. Sohail Nadeem**. Without his selfless support, generous guidance, and intellectual enrichment, this dissertation would not have accomplished.*

*I am grateful to my family especially my beloved parents, **Mr. Noor Ahmed**, and **Mrs. Salma Begum** for their continuous, unconditional love and support throughout my career. Also, I am thankful to my wife **Safia Bano** and brother **Fawad** for always believes in me and be there for me whenever I need encouragement and moral support.*

*I am extremely thankful to **Naeem ullah**, **Noor Muhammed**, **Zahid Nisar**, and **Arif ullah Khan** to be always around whenever I need them. I always feel fortunate to be blessed with such friends and colleagues.*

Zahid Ahmed

January 2020

Contents

| | | |
|----------|---|-----------|
| 1 | Introduction..... | 7 |
| 2 | Numerical solution of CNT based nanofluid flowing through squeezing channel..... | 15 |
| 2.1 | Introduction..... | 15 |
| 2.2 | Mathematical Modelling..... | 15 |
| 2.3 | Solution Procedure..... | 18 |
| 2.4 | Results and Discussion..... | 24 |
| 3 | Micropolar nanofluid flow passing through squeezing walls..... | 30 |
| 3.1 | Introduction..... | 30 |
| 3.2 | Mathematical Description..... | 30 |
| 3.3 | Solution procedure..... | 33 |
| 3.4 | Graphical Results..... | 41 |
| 4 | Carbon Nanotubes based nanofluid flow over a stretching Curved surface..... | 49 |
| 4.1 | Introduction..... | 49 |
| 4.2 | Mathematical Description..... | 49 |
| 4.3 | Solution Technique..... | 52 |
| 4.4 | Results and Discussion..... | 53 |
| 5 | Unsteady flow of a Carbon Nanotubes based nanofluid over a porous shrinking curved surface | 59 |
| 5.1 | Introduction..... | 59 |
| 5.2 | Mathematical description..... | 59 |
| 5.3 | <i>Solution procedure</i>..... | 63 |
| 5.4 | Results and Analysis..... | 66 |
| 6 | Computational study of CNT based nanofluid flow over a curved surface with micro-rotational inertia..... | 73 |
| 6.1 | Introduction..... | 73 |
| 6.2 | Mathematical description..... | 73 |
| 6.3 | Solution procedure:..... | 77 |
| 6.4 | Results and Analysis..... | 77 |
| 7 | Thesis Conclusion..... | 85 |

Tables List

| | |
|---|----|
| Table 1.1 Experimental values for thermo-physical quantities used in the study[17]..... | 11 |
| Table 2.1 Comparison Table for Keller box and BVP4C methods. $Ha = 1.0, Rd = 1.0, S = 1.0$. | 23 |
| Table 2.2 Variations in Nusselt number and Skin-friction with volume fraction and viscosity parameter. $Ha = 1.0, Rd = 1.0, S = 1.0$ | 26 |
| Table 2.3 Variations in Nusselt number and Skin-friction with the Squeezing parameter and viscosity parameter. $Ha = 1.0, Rd = 1.0, \varphi = 0.05$ | 27 |
| Table 2.4 Variations in Nusselt number and Skin-friction with the Radiations parameter and viscosity parameter. $Ha = 1, S = 2, \varphi = 0.05$ | 28 |
| Table 2.5 Variations in Nusselt number and Skin-friction with Hartman number and viscosity parameter. $Rd = 1.0, S = 2, \varphi = 0.05$ | 28 |
| Table 3.1 Comparison Table for velocity gradient near the plates $Ha = 0, Rd = 0, \varphi = 0$,..... | 41 |
| Table 4.1 Comparison Table for $-CfRes^{1/2}$ with different values of the curvature parameter. $\lambda = 1, M = 0, \phi = 0.0, \theta r \rightarrow \infty$ | 57 |
| Table 4.2 Numerical values of $-CfRes - 1/2$ with different values of curvature and variable viscosity parameters. $\lambda = 1, M = 2, \phi = 0$ | 58 |
| Table 5.1 Comparison of $f''(0)$ for existing analytical and our numerical solutions $\kappa \rightarrow \infty, \beta = 0, S = 2, \phi = 0, M = 0$,..... | 66 |

Figures List

| | |
|---|----|
| Figure 2.1 Flow geometry of fluid passing through squeezing plates..... | 16 |
| Figure 2.2 Mesh points functional diagram..... | 20 |
| Figure 2.3 Velocity variations with Magnetic parameter..... | 24 |
| Figure 2.4 Velocity variations with Squeezing parameter..... | 24 |
| Figure 2.5 Velocity variations with variable Viscosity parameter..... | 24 |
| Figure 2.6 Velocity variations with Radiation parameter..... | 24 |
| Figure 2.7 Temperature variations versus Squeezing parameter..... | 25 |
| Figure 2.8 Temperature variations versus Volume fraction of SWCNT..... | 25 |
| Figure 2.9 Temperature variations versus variable Viscosity parameter..... | 25 |
| Figure 2.10 Temperature variations versus Radiation parameter..... | 25 |
| Figure 3.1 Streamlines patterns..... | 42 |
| Figure 3.2 Velocity vectors..... | 42 |
| Figure 3.3 Velocity distribution profile with Magnetic parameter..... | 42 |
| Figure 3.4 Velocity distribution profile with Squeezing parameter..... | 42 |
| Figure 3.5 Velocity distribution profile with variable Viscosity parameter..... | 43 |
| Figure 3.6 Velocity distribution profile with Radiation parameter..... | 43 |
| Figure 3.7 Velocity distribution profile with Micropolar parameter..... | 44 |
| Figure 3.8 Variations in Temperature with Squeezing parameter..... | 44 |
| Figure 3.9 Variations in Temperature with Volume fraction parameter..... | 44 |
| Figure 3.10 Variations in Temperature with Radiation parameter..... | 44 |
| Figure 3.11 Angular velocity variations with Magnetic parameter..... | 45 |
| Figure 3.12 Angular velocity variations with Micropolar parameter..... | 45 |
| Figure 3.13 Angular velocity variations with variable Viscosity parameter..... | 45 |
| Figure 3.14 Angular velocity variations with Radiation parameter..... | 45 |
| Figure 3.15 Angular velocity variations with Squeezing parameter..... | 46 |
| Figure 3.16 Nusselt number profile with Magnetic parameter..... | 46 |
| Figure 3.17 Nusselt number profile with Radiation parameter..... | 46 |
| Figure 3.18 Nusselt number profile with Squeezing parameter..... | 46 |
| Figure 3.19 Skin friction versus Magnetic parameter..... | 47 |
| Figure 3.20 Skin friction versus Micropolar parameter..... | 47 |
| Figure 3.21 Skin friction versus variable Viscosity parameter..... | 47 |
| Figure 3.22 Skin friction versus Magnetic parameter..... | 47 |
| Figure 4.1 Functional diagram..... | 50 |
| Figure 4.2 Pressure distribution versus Curvature parameter..... | 54 |
| Figure 4.3 Pressure distribution versus Stretching parameter..... | 54 |
| Figure 4.4 Velocity variations with variable Viscosity parameter..... | 55 |
| Figure 4.5 Velocity variations with Volume fraction parameter..... | 55 |
| Figure 4.6 Velocity variations with Magnetic parameter..... | 55 |
| Figure 4.7 Velocity variations with Curvature parameter..... | 55 |
| Figure 4.8 Temperature variations with variable Viscosity parameter..... | 56 |
| Figure 4.9 Temperature variations with Volume fraction parameter..... | 56 |
| Figure 4.10 Temperature variations with Magnetic parameter..... | 56 |

| | |
|--|----|
| Figure 4.11 Temperature variations with Curvature parameter | 56 |
| Figure 4.12 Velocity gradient with Curvature parameter | 57 |
| Figure 4.13 Velocity gradient with Stretching parameter | 57 |
| Figure 5.1 Flow diagram | 60 |
| Figure 5.2 Pressure variations with Shrinking parameter | 67 |
| Figure 5.3 Pressure variations with Suction parameter | 67 |
| Figure 5.4 Skin friction versus Curvature parameter | 69 |
| Figure 5.5 Skin friction versus variable Viscosity parameter | 69 |
| Figure 5.6 Skin friction versus Porosity parameter | 69 |
| Figure 5.7 Skin friction versus Curvature and Suction parameter | 69 |
| Figure 5.8 Skin friction versus Shrinking parameter | 70 |
| Figure 5.9 Skin friction versus variable Viscosity parameter | 70 |
| Figure 5.10 Velocity and Velocity gradient with Shrinking parameter (Lower Solution) | 70 |
| Figure 5.11 Velocity and Velocity gradient with Shrinking parameter (Upper Solution) | 70 |
| Figure 5.12 Velocity and Velocity gradient versus Suction parameter (Lower Solution) | 71 |
| Figure 5.13 Velocity and Velocity gradient versus Suction parameter (Upper Solution) | 71 |
| Figure 5.14 Velocity along r-direction | 71 |
| Figure 5.15 Velocity along s-direction | 71 |
| Figure 5.16 Temperature variation versus Curvature parameter | 72 |
| Figure 5.17 Temperature variation versus CNT volume fraction | 72 |
| Figure 5.18 Temperature variation versus Suction parameter | 72 |
| Figure 5.19 Temperature variation versus variable Viscosity parameter | 72 |
| Figure 6.1 Streamlines patterns | 78 |
| Figure 6.2 Pressure distribution with variable Viscosity parameter | 78 |
| Figure 6.3 Isotherm with $k = 5$ | 79 |
| Figure 6.4 Isotherm with $k = 10$ | 79 |
| Figure 6.5 Isotherm with $k = 15$ | 79 |
| Figure 6.6 Isotherm with $\varphi = 0.05$ | 79 |
| Figure 6.7 Isotherm with $\varphi = 0.10$ | 79 |
| Figure 6.8 Isotherm with $\varphi = 0.15$ | 79 |
| Figure 6.9 Isotherm with $S = 0.50$ | 79 |
| Figure 6.10 Isotherm with $S = 2.0$ | 79 |
| Figure 6.11 Isotherm with $S = 3.0$ | 79 |
| Figure 6.12 Velocity variations versus Curvature parameter | 80 |
| Figure 6.13 Velocity variations versus Magnetic parameter | 80 |
| Figure 6.14 Velocity variations versus variable viscosity parameter | 80 |
| Figure 6.15 Velocity variations versus Porosity parameter | 80 |
| Figure 6.16 Skin friction versus Micropolar parameter | 81 |
| Figure 6.17 Skin friction versus Curvature parameter | 81 |
| Figure 6.18 Skin friction versus Variable viscosity parameter | 81 |
| Figure 6.19 Skin friction versus Porosity parameter | 81 |
| Figure 6.20 Couple stress variations with Micropolar parameter | 82 |
| Figure 6.21 Couple stress variations with Curvature parameter | 82 |
| Figure 6.22 Couple stress variations with Magnetic parameter | 82 |

| | |
|--|-----------|
| Figure 6.23 Couple stress variations with variable Viscosity parameters | 82 |
| Figure 6.24 Couple stress variations with Porosity parameter | 83 |
| Figure 6.25 Nusselt number variations with Prandtl number for SWCNT and MWCNT | 83 |
| Figure 6.26 Nusselt number variations with Curvature parameter | 83 |
| Figure 6.27 Nusselt number variations with variable viscosity parameters | 83 |
| Figure 6.28 Nusselt number variations with Porosity parameter..... | 84 |

Nomenclature

| | | | |
|-------------|--|---------------|---|
| μ_{nf} | Effective dynamic viscosity of nanofluid | f | Dimensionless velocity |
| ν_{nf} | Effective kinematic viscosity of nanofluid | g | Dimensionless Angular velocity |
| ρ_{nf} | Effective density of nanofluid | θ | Dimensionless Temperature |
| p | Fluid pressure | θ_r | Variable viscosity parameter |
| C_{nf} | Effective heat capacitance | K_{nf} | Effective thermal conductivity of nanofluid |
| $B(t)$ | Magnetic field | α_{nf} | Effective heat diffusivity of nanofluid |
| K | Micropolar parameter | ϕ | Volume fraction of nanofluid |
| σ_e | Stfan Boltzmann constant | β_R | Mean absorption constant |
| κ | Curvature parameter | M | Magnetic parameter |
| T | Fluid temperature | Pr | Prandtl number |
| σ | Electric charge density | q_r | Radiative heat flux |
| S | Squeezing parameter | Rd | Radiation parameter |
| H | Hartmann number | λ | Stretching or shrinking parameter |
| Nu | Nusselt number | C_f | Skin friction coefficient |

1 Introduction

Heat management crises in various industrial applications demanded alternative technology. Choi and Eastman[1] introduced the idea of nanofluids in 1995 for the very first time. These novel fluids types were synthesized in laboratories by endowing solid particles of nano-sized in the base-fluid. The resulting formation was now a fluid with upgraded effective physical and thermal characteristics such as thermal conductivity or heat capacitance. Very soon after the emergence of these newly invented types of fluids, they capture the attention of researchers, engineers, and scientists to utilize this idea in real-world applications, such as the cooling system of vehicles, heat exchangers, manufacturing tools, paints, electronics devices and in medical engineering tools. In all these widespread applications, nanofluids have proved themselves capable to handle the significantly critical problems by enhancing the effective heat transfer ability of fluid material at a lower cost. Due to its adjustable physical and thermal properties such as effective density, heat capacitance or thermal conductivity nanotechnology is expected to cater as an effective and efficient medium of heat transfer. Following Choi many researchers have been contributed in the field of nanofluid, mention may be made to some very recent and important works. Ghadikolaei et al.[2] shows the effects of magnetism and porosity on micropolar dusty fluids with metallic nanoparticles. Nadeem et al.[3] presented a study that reveals the impact of magnetism and slips on the dynamics of a micropolar hybrid nanofluid over a cylindrical body. Alamri et al.[4] studied convective Poiseuille flow of a nanofluid on a plane porous medium. A heat convection case on a wavy surface was considered by Hassan et al.[5]. Malvandi et al.[6] presented a study that shows the effects of nano-particles transportation at film boiling of nanofluid over a vertical plate. Nadeem et al.[7] presented a theoretical investigation of nanofluid implications as a drug carrier in stenosed arteries with the MHD field. Sheikholeslami et al.[8] disclosed the influence of magnetism on nanofluid flow under forced convection in a lid-driven cavity. Nanofluid flow under natural convection in the presence of thermal radiations is also presented by Sheikholeslami et al.[9]. Shiekhalipour et al.[10] numerically analyzed the flow of a nanofluid in a trapezoidal microchannel. They investigated the results obtained with different models and compared them with the available experimental results. It is concluded in the study that the Eulerian model predicted outcomes are more comparable to the experimental observations. Nadeem et al.[11] solved the problem of Falkner-Skan for static as well as moving wedge numerically. Chakraborty et al.[12] discussed the effects of an applied magnetic field for bioconvection in nanofluid

possessing gyrotactic microorganisms. Most of the commonly used models are lack of predicting the distortions of nano-particles size on the effective nanofluid's viscosity. They concluded that rising numeric for the parameter of surface convection enhances the number of self-moving microorganisms. Koca et al.[13] reviewed the change in nanofluid's viscosity by varying the size of the nano-particle and compared them with proposed models for effective viscosity of nanofluids. They found that the variation of almost 40% in the viscosity can be seen only by changing the particle size of nanofluids. Diglio et al.[14] suggested a geophysical application of the nanofluid as a heat carrier in Borehole heat exchangers. They conducted a numerical study to assess the use of different nanofluids instead of conventionally used fluids like glycol and water mixtures. The work aimed to find the best medium that can reduce borehole thermal resistance efficiently. They investigated the case with different types of solid particles including silver, copper, alumina, etc. and found that copper-based nanofluid provides a significant reduction in borehole thermal resistance. Carbon nanotubes are among the types of solid nano-particles that are frequently used as solid constituent in the nanofluid. These sheets of graphite soiled in cylindrical shape has tremendous application in medical and thermal engineering tools. They are used in drugs delivery system within the body[15]. Also, these nano particles have proven ability of penetrating into cell membrane and target tumor affected cells very effectively[16]. Experimental studies proved that they are less cytotoxic and do not harm the body immune system in side effects. Biosensing for disease diagnostic systems and health monitoring is another implication of tools that prevalently utilized CNT's benefits. These materials have very distinctive thermo-physical properties as compared to other solid constituents of nanofluids. Carbon nanotubes are less dense as compared to metallic nanoparticles whereas they possess higher thermal conductivity. All these materials are environment friendly. Nadeem et al.[17] presented the mass and heat flow of a CNT based nanofluids. In this study, they have differentiated the impacts of single-walled and multi-walled carbon nanotubes on the heat flow phenomena. Akbar et al.[18] conducted a numerical investigation to the problem of CNT based nanofluid flow over a sensor sheet keeping fluid properties variable. Hussain et al.[19] presented a study that analyzed the case of CNT based nanofluid flow under forced convection between two rotating surfaces. They have found in their study that single-walled carbon nanotubes produce less drag and acquire a relatively high heat transfer rate as compared to multi-walled carbon nanotubes. Shahzadi et al.[20] examined the use of single-walled carbon nanotubes based nanofluid for the peristaltic flow through annulus. In this

study, the effective dynamic viscosity is considered as a function of radial distance from the boundaries and nanoparticle concentration. The results depicted that the highest velocity of SWCNT-based blood rises for ascending magnitude of viscosity parameter.

Possessing two different phases, Nanofluids may produce rotational inertia at the micro-level. The Navier-Stokes model in its classical form is limited to the motion of fluids as a whole. This theory does not bother the intrinsic motion of fluid particles due to its microstructure. In many practical applications, however, these intrinsic motion plays a vital role in developing various dimensions of flow. On contrary to the Navier-Stokes model Eringen theory of micropolar [21,22] fluids take into account the inner structure and discusses the resulting intrinsic motion of fluid particles such as rotational or spin motion. This theory generalizes the classical Navier-Stokes model. Mathematically stress tensor is presented as the symmetric and asymmetric part. In addition, an equation representing the law of angular momentum conservation is also added to the system of regulation of equations. Researchers have contributed to the field considering that this is the theory that meticulously describes fluid motion. Nadeem et al.[23] studied the flow involving the stagnation point of a micropolar nanofluid on a cylindrical solid body. Shadloo et al.[24] worked out a solution of the heat and mass transfer on a continuous stretching sheet of a micropolar fluid. Subhani and Nadeem[25] conducted a numerical study of unsteady magnetohydrodynamics of hybrid micropolar nanofluid. They found that the rate at which heat transfer for a hybrid nanofluid is much larger in magnitude than that for a simple nanofluid. Akbar et al.[26] analytically studied the pressure-driven flow of a micropolar biological fluid passing through oscillatory walls. They considered metachronal wave propulsion due to cilia beating and concluded that axial velocity in their case decreases with ascending values of the micropolar parameter while the same parameter rises the magnitude of micro-rotations.

Magnetofluids are very important types of fluids that have a range of industrial applications. A relatively novel study namely magnetohydrodynamic was initiated by Hannes Alfvén for electrically conducting fluids. The field of study can be analyzed by considering Maxwell's equations of electromagnetism with that of other governing equations such as momentum or energy equations. Ma et al.[27] gave the numerical solution to the problem of the natural convective flow of a nanofluid in a U-shaped cavity with MHD considerations. Haq et al. [28] discussed the magnetohydrodynamics of fluid in a corrugated cavity with natural convection. They

have applied the finite element technique to solve the problem and found that velocity and temperature tend to increase with corrugated frequency. Rashidi et al.[29] investigated the case of MHD nanofluid flow due to peristaltic motion with entropy generation phenomena.

In dealing with viscous fluids researcher normally considers the case of constant viscosity. In real life situations however dynamic viscosity either depends on space or temperature variables as in the case of liquid fluids, It can be a function of pressure or stresses as in the case of solids or non-Newtonian fluids, or it can exhibit variations with a density as in case of gases. In liquid materials however dynamic viscosity often varies with changing temperature. The variation in fluid temperature during heat passing through boundaries or variation due to heat production during the internal friction of fluid molecules can affect the dynamic viscosity and hence in result disturb the flow behavior. This phenomenon can be observed in a wide range of fluid materials. Water and Coal slurries, for example, depicts the above scenario with variation in temperature. The viscosity of such fluids normally depends inversely on temperature. A rise in temperature may, therefore, fasten the mass transport phenomena. The situation is encountered very frequently in experimental studies hence the flow study of fluids with temperature-dependent dynamic viscosity is unavoidable most of the time. Ellahi et al.[30] discussed the effects of variable fluid viscosity on non-Newtonian fluid flow in a pipe. Xun et al.[31] investigated the bioconvection flow of nanofluids across two rotating surfaces with variable fluid viscosity. The result shows a remarkable variation in Nusselt number and Skin friction with viscosity variation of the fluid. Kharat et al.[32] investigated a nanofluid flow with solid-constituent as Cobalt Ferrite and Ethylene glycol under the influence of temperature-dependent dynamic viscosity. It is concluded from the study that viscosity increases with an increasing fraction of Cobalt Ferrite. Babu et al.[33] analyzed the flow across a slandering stretching sheet with variable viscosity. Convective boundary conditions are employed for both mass and heat transfer. A numerical solution is obtained for the problem under consideration. The study reveals that viscosity variation and the parameter for chemical reactions act oppositely on the concentration profile. Sobamowo et al.[34] studied the flow of a fourth-grade fluid with dynamic viscosity varying with temperature. The problem is solved with the perturbation technique.

The governing equations of fluid dynamics in two-dimensional flow consist of a couple of equations that represent the law of conservation for linear momentum, an equation that describes

the heat flow through the system based on the laws of thermodynamics and an equation that embed the conservation of angular momentum when rotational inertia case is considered. In general form, these mathematical statements are higher-order non-linear partial differential equations. Although researchers have presented the exact solution of some very special cases of these equations by analytical techniques. These equations are cumbersome to deal with in most of the time due to its higher nonlinearity. Convective acceleration term is a source of nonlinearity in momentum equations for instance. The analytical techniques never yielded an explicit exact solution for most of the cases. In fact, neither the exact solution nor the existence of it in general form has yet been presented. Even for very special cases, the analytical solution is hard to find. Instead, researchers find the approximate solution with numerical methods. These numerical techniques are more promising to search for the solution with relatively less effort. Researchers have employed many effective numerical techniques to uncover different flow problems. We have set the central objective of this work to model different nanofluid flow problems keeping most of the involved parameters variable and solved the governing highly nonlinear differential equations with effective numerical methods. Different geometrical situations of the bounded and semi-infinite domain through which fluid flows are assumed such as the flow of fluid through squeezing channel and boundary layer flows. Throughout this work, we have considered a magnetic field acting along normal to the flow direction of the fluid. It has been observed that this field acts differently with both cases of boundary layer and of the flow between plates at a finite distance. Equations are modeled such that nanofluid's effective viscosity is assumed as temperature-dependent.

Table 1.1 Experimental values for thermo-physical quantities used in the study[17]

| Thermo-physical properties | Pure water | SWCNT | MWCNT |
|-----------------------------|------------|-------|-------|
| C_p (J/kgK) | 4179.0 | 425 | 796 |
| ρ (kg/m ³) | 997.10 | 2600 | 1600 |
| k (W/mK) | 0.6130 | 6600 | 3000 |

Carbon nanotubes are taken as a solid constituent of water-based nanofluid for all of our assumed problems. Xue[35] model for thermal conductivity is taken into account. Standard values of

thermo-physical quantities associated with nanoparticles and base fluid that is used in our computations can be seen in **Table. 1. 1**.

Pressure dependence of fluids flow, viscosity variation with temperature and existence of magnetic field added into the non-linearity and complex form of governing equations. For most of the cases, these equations are in need of an effective numerical technique that has the capability to handle complex mathematical situations and non-linearity. Two different finite-difference numerical approaches are conducted to analyze the various assumed flow situations in this thesis. For the cases when the embedded governing equations can be written explicitly with a relatively smaller order of non-linearity, a built-in algorithm of MATLAB BVP4C package is incorporated. This method solves systems of nonlinear ordinary differential equations by applying the Lobatto IIIa formula. This technique solves the differential system by collocation approach. A continuous first-order differentiable polynomial is guessed as the solution and then solves the governing system. The above solution guess is taken by keeping in mind the boundary conditions. In this thesis, the above technique is used mostly to authenticate our solution by providing a comparative study for relatively simple cases with that of the main numerical technique used. For original problems that arose in this thesis, we have incorporated 2nd order accurate finite difference scheme called Keller box. It is an implicit numerical scheme the algorithm of which can effectively be used on complex, high order non-linear, coupled systems of differential equations. This method is unconditionally stable. The idea is to shape the differential equation system into a linear algebraic equation system. This algebraic system is then set into matrix-vector forms, such as the coefficient matrix at each iterating stage is a banded matrix of order three. The next part of the scheme procedure is to split this banded coefficient matrices into distinguished upper and lower triangular matrices, which are manipulated algebraically to solve the system. The detailed procedure can be differentiated into four discrete steps. In the very beginning, the equations are written into a set of differential equations of the first order. Secondly, this resulting equation system is discretized using a finite difference scheme. The third stage is to implement Newton's linearization technique to linearize the set of algebraic equations. The final step is to apply matrix algebra to the linearized system. This very last job is accomplished by programming the algorithm in MATLAB software. Error tolerance for all of the problems considered in this thesis is set as 10^{-6} . Since it was possible to find the transformations that transformed the ruling partial differential equations to similar ordinary differential equations, therefore, we write all problems included in this thesis as a similar

system of coupled nonlinear ordinary differential equations and then solve by the above method. Grid independence of the solution is also checked for all the problems. The step size and the boundary length is set such that the grid numbers do not affect the solution to six decimal places above the boundary length. For unbounded boundary layer problems, this length is set at $\eta = 16$. For this length, all the problems have passed the grid independence test. The present Thesis consist of six chapters in which the first chapter is an introductory chapter while all others are expressed as:

Chapter 2 includes the topic of hydromagnetic nanofluid flow across two parallel squeezing plates. Carbon nanotubes are assumed as the solid part of the water-based nanofluid flow. Nanofluid exhibit unsteady flow through squeezing solid boundaries. Radiative heat flux is also taken into considerations. Fluid dynamic viscosity is taken inversely related to the fluid temperature. The solution is obtained numerically with the Keller box method. In addition to the original problem, a simple case of constant viscosity is also solved with BVP4C MATLAB. Results obtained by both of these techniques are in very good agreement with each other. This work is **submitted for publication in “AIP Advances”**.

Chapter 3 aims to present the squeezing flow of a micropolar viscous nanofluid with variable dynamic viscosity. Carbon nanotubes are taken as the solid constituent of nanofluid. Water is assumed as base fluid. It is assumed that the presence of carbon nanotubes in the base fluid may cause the inertial difference between the two phases of the nanofluid, which in result can produce rotational and spin motion within the fluid body. Graphical and numerical results of important physical quantities are determined using MATLAB and Tecplot software. A second-order finite difference scheme is implemented to solve our problem. A Comparison study with previous literature is also done to authenticate our solution. The results obtained are published in “**Physica Scripta**”[36]. **(2019):19;12**.

Chapter 4 considered a viscous nanofluid flow on a curved stretching surface, the dynamic viscosity of the fluid inversely depending on fluid temperature. In addition, a uniform MHD field acting perpendicular to the curved surface is taken into considerations, Temperature and velocity of viscous nanofluid are analyzed for sparsely distributed values of involved parameters such as magnetic parameter, nano-particles volume fraction or curvature parameters. The solution is obtained numerically by transforming the equations that governed the system to similar nonlinear

coupled ordinary differential equations and then solved the resulting similar differential equations with a finite difference implicit scheme. A comparison study is also presented for results validation with previous literature. An article that represents the contents of this chapter is published in “**Microsystem Technologies**”[37]. (2019):25;2881-2888.

Chapter 5 includes the unsteady flow of a viscid nano-liquid above a permeable curved shrinking sheet with variable viscosity and magnetic field. On Navier stokes equations the boundary layer approximation is implemented also for thermal characteristics of the nanofluid the energy equation is used to model the flow problem. Keller box method is incorporated to reveal the characteristics of the proposed flow situation. Dual solutions are obtained, which are characterized as the upper and lower solution. The skin friction coefficient, velocity, and velocity gradient graphs are plotted. Distinguished critical points have been obtained. It is found that at one side of these critical points multiple solutions exist, On the other side only a single (stable) solution exists, whereas on these particular points no solution exists at all. A Comparison study is also represented with that of previous literature. The temperature and pressure profiles are also plotted opposite to various effective parameters. The work is published in the “**International Journal of Numerical Methods for Heat & Fluid Flow**” [38]. (2019) DOI: 10.1108/HFF-04-2019-0346

The main objective of **Chapter 6** is to analyze the impact of temperature-dependent viscosities on the nanofluid flow while considering rotational inertia over the curvilinear surface. The governing set of equations are first transformed to similar ordinary differential equations and then these extremely nonlinear differential equations are unraveled numerically with the help of the finite difference sheme. A detailed explanation of the mathematical procedure that has been followed is also mentioned in the study. A reasonable comparison is also given for the simplest case with that of previous literature. This chapter is published as an article in “**Processes**”[39]. (2019):7;6;387

2 Numerical solution of CNT based nanofluid flowing through squeezing channel.

2.1 Introduction

In this chapter, we have presented a computational investigation of a nanofluid unsteady flow passing through parallel plates of infinite length. The plates are squeezing towards with certain velocity. In addition, with thermal radiations, an unsteady magnetic field normal to the plates are taken into account. Fluid dynamic viscosity is sensitive to temperature. Navier stokes model for viscous fluids is used to model the physical situation. The governing equations are partial differential equations which have a high nonlinearity. Appropriate variables of similarity are used to transform these equations into identical ordinary differential equations which are nonlinear coupled equations. Such reduced, extremely non-linear differential equations would then be numerically worked out using the Keller box technique. It is an implicit numerical scheme with second-order accuracy which is stable unconditionally. Moreover, for the simplest case of no volume fraction of carbon nanotubes and constant viscosity, An another numerical method ‘BVP4c’ solves the problem. For investigating the flow behavior with the specified physical situations, computational and graphical results are obtained.

2.2 Mathematical Modelling

Let us assume a viscous nanofluid flowing through a squeezing channel. The edges of the channel are two parallel plates of infinite length. Both plates are at a distance $h(t) = l(1 - \beta t)^{1/2}$ from the origin, O. For $\beta > 0$ the plates squeezed till they meet at $t = 1/\beta$. An unsteady magnetic field acting in a perpendicular direction to the plates are taken into considerations with strength $B(t) = B_0(1 - \beta t)^{-1/2}$, where B_0 represents the initial magnetic intensity. Radiative heat transfer is also considered. **Figure 2.1** represents the geometry of the assumed problem.

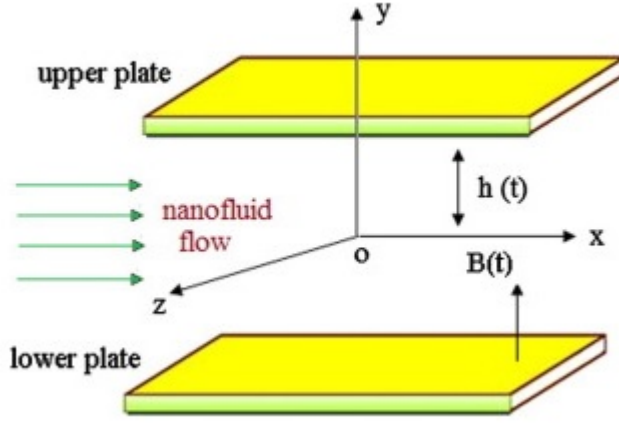


Figure 2.1 Flow geometry of fluid passing through squeezing plates

The respective governing equations are given as:

$$\frac{\partial \bar{U}}{\partial x} + \frac{\partial \bar{V}}{\partial y} = 0, \quad (2.1)$$

$$\frac{\partial \bar{U}}{\partial t} + \bar{V} \frac{\partial \bar{U}}{\partial y} + \bar{U} \frac{\partial \bar{U}}{\partial x} = -\frac{1}{\rho_{nf}} \frac{\partial p}{\partial x} + \frac{1}{\rho_{nf}} \frac{\partial}{\partial y} \left(\mu_{nf} \frac{\partial \bar{U}}{\partial y} \right) - \sigma B^2(t) \bar{U}, \quad (2.2)$$

$$\frac{\partial \bar{V}}{\partial t} + \bar{V} \frac{\partial \bar{V}}{\partial y} + \bar{U} \frac{\partial \bar{V}}{\partial x} = -\frac{1}{\rho_{nf}} \frac{\partial p}{\partial y} + \frac{1}{\rho_{nf}} \frac{\partial}{\partial x} \left(\mu_{nf} \frac{\partial \bar{V}}{\partial x} \right) + \frac{1}{\rho_{nf}} \frac{\partial}{\partial y} \left(\mu_{nf} \frac{\partial \bar{V}}{\partial y} \right) \quad (2.3)$$

$$\frac{\partial \bar{T}}{\partial t} + \bar{V} \frac{\partial \bar{T}}{\partial y} + \bar{U} \frac{\partial \bar{T}}{\partial x} = -\frac{1}{(\rho C_p)_{nf}} \frac{\partial q_r}{\partial y} + \alpha_{nf} \left(\frac{\partial^2 \bar{T}}{\partial y^2} \right), \quad (2.4)$$

Where Equation (2.1) is mass conservation, Equation (2.2) and (2.3) are mathematical expressions to embed linear momentum conservation along x and y directions with \bar{U} and \bar{V} are the respective velocities in x and y directions. Equation (2.4) represents energy conservation phenomena. \bar{T} is used for fluid temperature profile, p symbolized the pressure distribution. The effective density is calculated as $\rho_{nf} = \phi \rho_{CNT} + (1 - \phi) \rho_{f\infty}$, where the effective heat capacity is taken as $(\rho C_p)_{nf} = \phi (\rho C_p)_{CNT} + (1 - \phi) (\rho C_p)_{f\infty}$. Since we have used Carbon nanotubes in the base fluid as a solid constituent, the thermal conductivity is computed by the model proposed by Xue et al.[35] which in mathematical form is written as:

$$\frac{K_{nf}}{K_{f\infty}} = \frac{1-\phi+2\phi\frac{K_{CNT}}{K_{CNT}-K_{f\infty}}\ln\frac{K_{CNT}+K_{f\infty}}{2K_{f\infty}}}{1-\phi+2\phi\frac{K_{f\infty}}{K_{CNT}-K_{f\infty}}\ln\frac{K_{CNT}+K_{f\infty}}{2K_{f\infty}}}. \mu_{nf} \text{ represent the nanofluid viscosity, which is defined as:}$$

$\mu_{nf} = \frac{\mu_{f\infty}}{(1-\phi)^{2.5}}$, where $\mu_{f\infty}$ is the symbol used for base fluid viscosity which in our case vary inversely with temperature i.e. $\frac{1}{\mu_{f\infty}} = a(\bar{T} - T_r)$, Since $a = \frac{\delta}{\mu_{f\infty}}$, $T_r = T_\infty - \frac{1}{\delta}$, δ and a are constants, and $a > 0$ for liquids. The heat flux through radiations is calculated on the bases of Rosseland approximation which is: $q_r = -\frac{4\sigma_e}{3\beta_R} \frac{\partial \bar{T}^4}{\partial y}$, σ_e be Stefan Boltzmann constant and β_R be the mean absorption parameter. The thermal difference of the fluid phases are so small that \bar{T}^4 is taken as a linear function of fluid temperature \bar{T}^4 is replaced by a linear function of fluid temperature. i.e: We expand \bar{T}^4 in Taylor series about the temperature T_c such that $\bar{T}^4 = 4T_c^3\bar{T} - T_c^3$.

For the above system the relevant boundary conditions are:

$$\left. \begin{array}{l} \frac{\partial \bar{U}}{\partial y} = 0, \quad \bar{V} = 0, \quad \frac{\partial \bar{T}}{\partial y} = 0 \quad \text{at} \quad y = 0, \\ \bar{U} = 0, \quad \bar{V} = \frac{dh}{dt}, \quad \bar{T} = T_h \quad \text{at} \quad y = h(t). \end{array} \right\} \quad (2.5)$$

The differential equations presented in equations (2.1-2.4) are mold t a set of similar ordinary differential equations. For the purpose, we introduced two new dimensionless functions f , θ and a similarity variable η such as,

$$\begin{aligned} \bar{V} &= \frac{-\beta l}{2(1-\beta t)^{\frac{1}{2}}} f(\eta), & \bar{U} &= \frac{\beta x}{2(1-\beta t)} f'(\eta), \\ \theta &= \frac{\bar{T} - T_c}{T_h - T_c}, & \eta &= \frac{y}{l(1-\beta t)^{\frac{1}{2}}} \end{aligned} \quad (2.6)$$

Applying the above transformations, the equation of continuity identically satisfies while the equations representing momentum and the energy conservations reduced to the form below:

$$f^{iv} + \frac{f''\theta'^2}{\theta_r^2 \left(1 - \frac{\theta}{\theta_r}\right)^2} + \frac{f'''\theta'}{\theta_r \left(1 - \frac{\theta}{\theta_r}\right)} + \frac{f''\theta''}{\theta_r \left(1 - \frac{\theta}{\theta_r}\right)} - Ha^2 f'' - A_1 S \left(1 - \frac{\theta}{\theta_r}\right) (\eta f'''' + 3f''' + f'f'' - ff''') = 0 \quad (2.7)$$

$$\left(1 + \frac{4}{3\epsilon_1} Rd\right) \theta'' - S \frac{\epsilon_2}{\epsilon_1} Pr(f\theta' + \eta\theta') = 0 \quad (2.8)$$

$$\begin{aligned} f = 0, \quad f'' = 0, \quad \theta' = 0 \text{ at } \eta = 0 \\ f = 1, \quad f' = 0, \quad \theta = 1 \text{ at } \eta = 1 \end{aligned} \quad (2.9)$$

Where,

$$\left. \begin{aligned} A_1 &= (1 - \phi)^{2.5} \left[\phi \frac{\rho_{CNT}}{\rho_{f\infty}} + (1 - \phi) \right], \quad Rd = \frac{4\sigma_e \bar{T}^3}{K_{f\infty} \beta_R}, \quad S = \frac{\beta l^2}{2\nu_{f\infty}}, \quad \alpha_{nf} = \frac{K_{nf}}{(\rho C_p)_{nf}}, \\ Pr &= \frac{\mu_{f\infty} (\rho C_p)_{f\infty}}{\rho_{f\infty} K_{f\infty}}, \quad \epsilon_1 = \frac{1 - \phi + 2\phi \frac{K_{CNT}}{K_{CNT} - K_{f\infty}} \ln \frac{K_{f\infty} + K_{CNT}}{2K_{f\infty}}}{1 - \phi + 2\phi \frac{K_f}{K_{CNT} - K_{f\infty}} \ln \frac{K_{f\infty} + K_{CNT}}{2K_{f\infty}}}, \\ \epsilon_2 &= (1 - \phi) + \phi \frac{(\rho C_p)_{CNT}}{(\rho C_p)_{f\infty}}, \end{aligned} \right\}$$

The mathematical assertions derived for Skin-friction and Nusselt number are $C_f = \left(\frac{\mu_{nf}}{\rho_{nf} \left(\frac{dh}{dt}\right)^2} \frac{\partial \bar{u}}{\partial y}\right)_{y=h(t)}$ and $Nu = \left(\left(1 + \frac{4}{3\epsilon_1} Rd\right) \frac{l K_{nf}}{K_{f\infty} T_h} \frac{\partial \bar{T}}{\partial y}\right)_{y=h(t)}$, respectively, which is the dimensionless form is given as

$$C_f^* = \frac{l^2 Re_x}{2x^2} C_f \sqrt{1 - \beta t} = \frac{1}{A_1 \left(1 - \frac{1}{\theta_r}\right)} f''(1), \quad N_u^* = \epsilon_1 \left(1 + \frac{4}{3\epsilon_1} Rd\right) \theta'(1)$$

2.3 Solution Procedure

Boundary layer approximation has brought in to handle the general Naiver Stokes equation to model the desired physical problem. The obtained equations are nonlinear partial differential equations that are remodeled by implementing effective transformations. These transformations

convert the equations to similar ordinary differential equations. To find the numerical solution of the transformed non-linear differential equations, the Keller-box scheme is used. This numerical technique is composed of four separate procedures given in the proceeding sections. At the very beginning, the equations are transformed into a set of first-order differential equations, as mentioned below:

$$f' = u \quad (2.10)$$

$$u' = v \quad (2.11)$$

$$v' = w \quad (2.12)$$

$$\theta' = m \quad (2.13)$$

$$\begin{aligned} w' - \frac{2}{\theta_r} w' \theta + \frac{1}{\theta_r^2} w' \theta^2 + \frac{1}{\theta_r} w m + \frac{1}{\theta_r} v m' - \frac{1}{\theta_r^2} w m \theta - \frac{1}{\theta_r^2} v m' \theta + \frac{1}{\theta_r^2} v m^2 - H a^2 v \\ + \frac{2}{\theta_r} H a^2 v \theta - \frac{1}{\theta_r} H a^2 v \theta^2 - A_1 S \eta w - 3 A_1 S v - 5 A_1 S u v - A_1 S f v + \frac{3}{\theta_r} A_1 S \eta w \theta \\ + \frac{9}{\theta_r} A_1 S v \theta + \frac{15}{\theta_r} A_1 S u v \theta + \frac{3}{\theta_r} A_1 S f v \theta - \frac{9}{\theta_r^2} A_1 S v \theta^2 - \frac{15}{\theta_r^2} A_1 S u v \theta^2 \\ - \frac{3}{\theta_r^2} A_1 S f v \theta^2 + \frac{1}{\theta_r^3} A_1 S \eta \theta^3 + \frac{3}{\theta_r^3} A_1 S v \theta^3 + \frac{5}{\theta_r^3} A_1 S u v \theta^3 + \frac{1}{\theta_r^3} A_1 S f v \theta^3 \\ + \frac{1}{\theta_r} A_1 S \eta v m + \frac{2}{\theta_r} A_1 S u m + \frac{2}{\theta_r} A_1 S u^2 m - \frac{2}{\theta_r^2} A_1 S \eta v m \theta - \frac{4}{\theta_r^2} A_1 S u m \theta \\ - \frac{4}{\theta_r^2} A_1 S u^2 m \theta + \frac{1}{\theta_r^3} A_1 S \eta v m \theta^2 + \frac{2}{\theta_r^3} A_1 S u m \theta^2 + \frac{2}{\theta_r^3} A_1 S u^2 m \theta^2 = 0 \end{aligned} \quad (2.14)$$

$$A_2 m' - A_3 \eta m - A_3 f m = 0 \quad (2.15)$$

Where u, v, w and m are the new variables adopted to write the above differential equations system as a set of first-order, ordinary differential equations. It sets out the respective boundary conditions as follows:

$$v = 0, \quad f = 0, \quad m = 0 \quad \text{at } \eta = 0$$

$$u = 0, \quad f = 1, \quad \theta = 1 \quad \text{at } \eta = 1$$

We now find the finite difference approximation of the governing system of 1st order equations. For the purpose let us consider the working domain as a rectangular net in the (x, η) -plan consist of mesh points as shown in the schematic diagram in **Figure 2.2**.

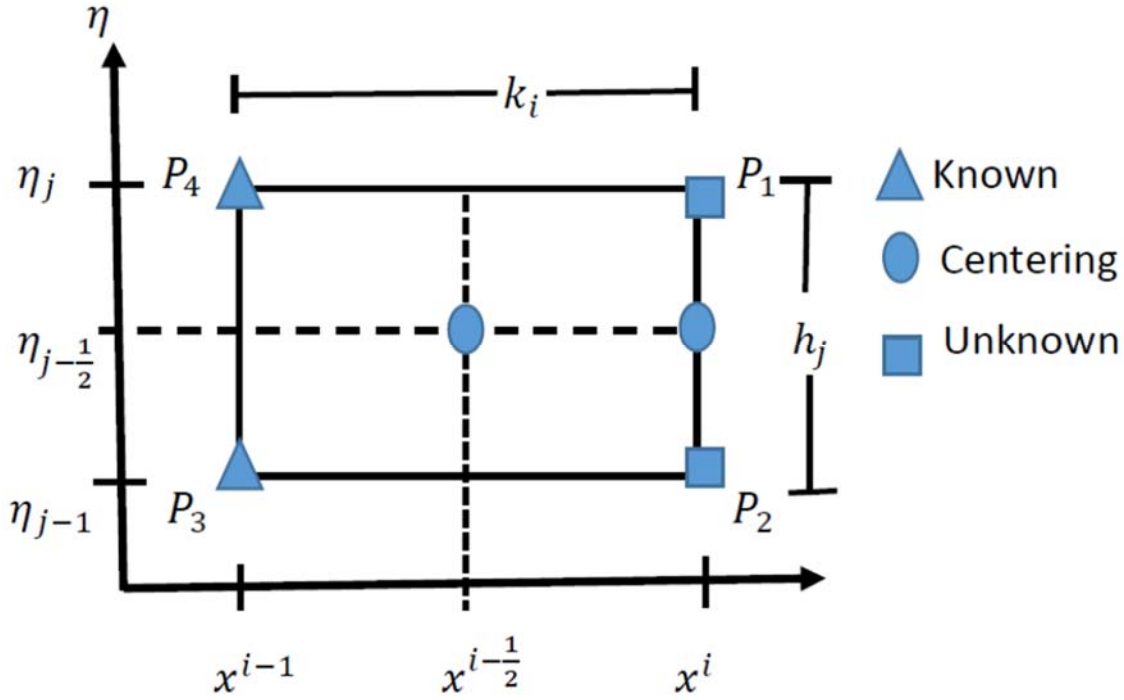


Figure 2.2 Mesh points functional diagram

i and j are progressions of numbers that imply the coordinate's position. The finite-difference form of any point will be $(\)_{j-1/2}^i = \frac{1}{2}[(\)_{j-1}^i + (\)_j^i]$ and $(\)_j^{i-1/2} = \frac{1}{2}[(\)_j^{i-1} + (\)_j^i]$.

Now applying the above scheme on the system of equations. The leading four equations are discretized by centering at $(x^i, \eta_{j-1/2})$ where the last two equations are discretized by centering at $(x^{i-1/2}, \eta_{j-1/2})$. The resulting equations are given below:

$$f_j^i = f_{j-1}^i + \frac{h_j}{2}(u_j^i + u_{j-1}^i) \tag{2.16}$$

$$u_j^i = u_{j-1}^i + \frac{h_j}{2}(v_j^i + v_{j-1}^i) \tag{2.17}$$

$$v_j^i = v_{j-1}^i + \frac{h_j}{2}(w_j^i + w_{j-1}^i) \quad (2.18)$$

$$\theta_j^i = \theta_{j-1}^i + \frac{h_j}{2}(m_j^i + m_{j-1}^i) \quad (2.19)$$

$$\begin{aligned} & \left[\frac{(w_j - w_{j-1})}{h_j} + \frac{1}{\theta_r^2} \frac{(w_j - w_{j-1})}{h_j} \frac{(\theta_j + \theta_{j-1})^2}{4} - \frac{2}{\theta_r} \frac{(w_j - w_{j-1})}{h_j} \frac{(\theta_j + \theta_{j-1})}{2} \right. \\ & + \frac{1}{\theta_r} \frac{(w_j + w_{j-1})}{2} \frac{(m_j + m_{j-1})}{2} - \frac{1}{\theta_r^2} \frac{(w_j + w_{j-1})}{2} \frac{(\theta_j + \theta_{j-1})}{2} \frac{(m_j + m_{j-1})}{2} \\ & + \frac{1}{\theta_r} \frac{(v_j + v_{j-1})}{2} \frac{(m_j - m_{j-1})}{h_j} - \frac{1}{\theta_r^2} \frac{(v_j + v_{j-1})}{2} \frac{(\theta_j + \theta_{j-1})}{2} \frac{(m_j - m_{j-1})}{h_j} \\ & + \frac{1}{\theta_r^2} \frac{(v_j + v_{j-1})}{2} \frac{(m_j + m_{j-1})^2}{4} - Ha^2 \frac{(v_j + v_{j-1})}{2} \\ & + \frac{2}{\theta_r} Ha^2 \frac{(v_j + v_{j-1})}{2} \frac{(\theta_j + \theta_{j-1})}{2} - \frac{1}{\theta_r^2} Ha^2 \frac{(v_j + v_{j-1})}{2} \frac{(\theta_j + \theta_{j-1})^2}{4} \\ & - A_1 S \eta \frac{(w_j + w_{j-1})}{2} - \frac{3}{2} A_1 S \frac{(v_j + v_{j-1})}{2} + A_1 S \frac{(f_j + f_{j-1})}{2} \frac{(w_j + w_{j-1})}{2} \\ & + \frac{3}{\theta_r} A_1 S \eta \frac{(w_j + w_{j-1})}{2} \frac{(\theta_j + \theta_{j-1})}{2} + \frac{9}{\theta_r} A_1 S \frac{(v_j + v_{j-1})}{2} \frac{(\theta_j + \theta_{j-1})}{2} \\ & - \frac{3}{\theta_r} A_1 S \frac{(f_j + f_{j-1})}{2} \frac{(w_j + w_{j-1})}{2} \frac{(\theta_j + \theta_{j-1})}{2} \\ & - \frac{3}{\theta_r^2} A_1 S \eta \frac{(w_j + w_{j-1})}{2} \frac{(\theta_j + \theta_{j-1})^2}{4} - \frac{9}{2\theta_r^2} \frac{(v_j + v_{j-1})}{2} \frac{(\theta_j + \theta_{j-1})^2}{4} \\ & + \frac{3}{\theta_r^2} A_1 S \frac{(f_j + f_{j-1})}{2} \frac{(w_j + w_{j-1})}{2} \frac{(\theta_j + \theta_{j-1})^2}{4} \\ & + \frac{1}{\theta_r^3} A_1 S \eta \frac{(w_j + w_{j-1})}{2} \frac{(\theta_j + \theta_{j-1})^3}{8} + \frac{3}{2\theta_r^3} A_1 S \eta \frac{(v_j + v_{j-1})}{2} \frac{(\theta_j + \theta_{j-1})^3}{8} \\ & \left. - \frac{1}{\theta_r^3} A_1 S \frac{(f_j + f_{j-1})}{2} \frac{(v_j + v_{j-1})}{2} \frac{(\theta_j + \theta_{j-1})^3}{8} \right]^i = M_{j-1/2} \end{aligned}$$

(2.20)

$$[A_2 \frac{(m_j - m_{j-1})}{h_j} - A_3 \eta \frac{(m_j + m_{j-1})}{2} - A_3 \frac{(f_j + f_{j-1})}{2} \frac{(m_j + m_{j-1})}{2}]^i = P_{j-1/2} \quad (2.21)$$

Where

$$\begin{aligned} M_{j-1/2} = & -[(w')_{j-\frac{1}{2}} - \frac{2}{\theta_r} (w'\theta)_{j-\frac{1}{2}} + \frac{1}{\theta_r^2} (w'\theta^2)_{j-\frac{1}{2}} + \frac{1}{\theta_r^2} (wm)_{j-\frac{1}{2}} + \frac{1}{\theta_r} (vm')_{j-\frac{1}{2}} \\ & - \frac{1}{\theta_r^2} (wm\theta)_{j-\frac{1}{2}} - \frac{1}{\theta_r^2} (vm'\theta)_{j-\frac{1}{2}} + \frac{1}{\theta_r^2} (vm^2)_{j-\frac{1}{2}} - Ha^2 v_{j-\frac{1}{2}} + \frac{2}{\theta_r} Ha^2 (v\theta)_{j-\frac{1}{2}} \\ & - \frac{1}{\theta_r} Ha^2 (v\theta^2)_{j-\frac{1}{2}} - A_1 S(\eta w)_{j-\frac{1}{2}} - 3A_1 S v_{j-\frac{1}{2}} - 5A_1 S(uv)_{j-\frac{1}{2}} - A_1 S(fv)_{j-\frac{1}{2}} \\ & + \frac{3}{\theta_r} A_1 S(\eta w\theta)_{j-\frac{1}{2}} + \frac{9}{\theta_r} A_1 S(v\theta)_{j-\frac{1}{2}} + \frac{15}{\theta_r} A_1 S(uv\theta)_{j-\frac{1}{2}} + \frac{3}{\theta_r} A_1 S(fv\theta)_{j-\frac{1}{2}} \\ & - \frac{9}{\theta_r^2} A_1 S(v\theta^2)_{j-\frac{1}{2}} - \frac{15}{\theta_r^2} A_1 S(uv\theta^2)_{j-\frac{1}{2}} - \frac{3}{\theta_r^2} A_1 S(fv\theta^2)_{j-\frac{1}{2}} + \frac{1}{\theta_r^3} A_1 S(\eta\theta^3)_{j-\frac{1}{2}} \\ & + \frac{3}{\theta_r^3} A_1 S(v\theta^3)_{j-\frac{1}{2}} + \frac{5}{\theta_r^3} A_1 S(uv\theta^3)_{j-\frac{1}{2}} + \frac{1}{\theta_r^3} A_1 S(fv\theta^3)_{j-\frac{1}{2}} + \frac{1}{\theta_r} A_1 S(\eta vm)_{j-\frac{1}{2}} \\ & + \frac{2}{\theta_r} A_1 S(um)_{j-\frac{1}{2}} + \frac{2}{\theta_r} A_1 S(u^2 m)_{j-\frac{1}{2}} - \frac{2}{\theta_r^2} A_1 S(\eta vm\theta)_{j-\frac{1}{2}} - \frac{4}{\theta_r^2} A_1 S(um\theta)_{j-\frac{1}{2}} \\ & - \frac{4}{\theta_r^2} A_1 S(u^2 m\theta)_{j-\frac{1}{2}} + \frac{1}{\theta_r^3} A_1 S(\eta vm\theta^2)_{j-\frac{1}{2}} + \frac{2}{\theta_r^3} A_1 S(um\theta^2)_{j-\frac{1}{2}} \\ & + \frac{2}{\theta_r^3} A_1 S(u^2 m\theta^2)_{j-\frac{1}{2}}]^{i-1} \end{aligned} \quad (2.22)$$

$$P_{j-1/2} = -[A_2 (m')_{j-\frac{1}{2}} - A_3 \eta m_{j-\frac{1}{2}} - A_3 (fm)_{j-\frac{1}{2}}]^{i-1} \quad (2.23)$$

$M_{j-1/2}$ and $P_{j-1/2}$ are the terms that are already known.

Newton's linearization is the very next step to follow. We replace variables f, u, v, w, θ and m with $f + \delta f, u + \delta u, v + \delta v, w + \delta w, \theta + \delta \theta$ and $m + \delta m$ respectively. The resulting linear set of equations are then written as:

$$\delta f_j - \delta f_{j-1} - \frac{h_j}{2} (\delta u_{j-1} + \delta u_j) = (r_1)_j \quad (2.24)$$

$$\delta u_j - \delta u_{j-1} - \frac{h_j}{2}(\delta v_{j-1} + \delta v_j) = (r_2)_j \quad (2.25)$$

$$\delta v_j - \delta v_{j-1} - \frac{h_j}{2}(\delta w_{j-1} + \delta w_j) = (r_3)_j \quad (2.26)$$

$$\delta \theta_j - \delta \theta_{j-1} - \frac{h_j}{2}(\delta m_{j-1} + \delta m_j) = (r_5)_j \quad (2.27)$$

$$(a_1)_j \delta v_j + (a_2)_j \delta v_{j-1} + (a_3)_j \delta u_j + (a_4)_j \delta u_{j-1} + (a_5)_j \delta f_j + (a_6)_j \delta f_{j-1} + (a_7)_j \delta w_j + (a_8)_j \delta w_{j-1} + (a_9)_j \delta \theta_j + (a_{10})_j \delta \theta_{j-1} + (a_{11})_j \delta m_j + (a_{12})_j \delta m_{j-1} = (r_6)_j \quad (2.28)$$

$$(b_1)_j \delta v_j + (b_2)_j \delta v_{j-1} + (b_3)_j \delta u_j + (b_4)_j \delta u_{j-1} + (b_5)_j \delta f_j + (b_6)_j \delta f_{j-1} + (b_7)_j \delta w_j + (b_8)_j \delta w_{j-1} + (b_9)_j \delta \theta_j + (b_{10})_j \delta \theta_{j-1} + (b_{11})_j \delta m_j + (b_{12})_j \delta m_{j-1} = (r_7)_j \quad (2.29)$$

At the very end, the system of above-linearized equations is solved algebraically by setting these equations into matrix form, which are decomposed and written into banded matrices of upper and lower triangular types. A MATLAB script is programmed to solve the system by block elimination technique. A very fine step size of $\Delta\eta = 0.005$ is taken as a step size for all computations. Error tolerance is fixed at 10^{-6} . Scheme results are authenticated by comparing them with the solution obtained from another MATLAB built-in solver BVP4C for the simplest case of constant dynamic viscosity. The data obtained from both methods appeared to be in good agreement with each other. **Table 2.1** presents the comparison of said methods.

Table 2.1 Comparison Table for Keller box and BVP4C methods. $Ha = 1.0$, $Rd = 1.0$, $S = 1.0$

| φ | $f''(1)$ | | $\theta'(1)$ | |
|-----------|------------|---------|--------------|--------|
| | Keller Box | BVP4C | Keller Box | BVP4C |
| 0.025 | -5.0517 | -5.0521 | 3.3159 | 3.3145 |
| 0.05 | -4.9977 | -4.9985 | 2.7623 | 2.7616 |
| 0.10 | -4.8769 | -4.8779 | 1.9801 | 1.9785 |

2.4 Results and Discussion

Numerical, as well as graphical results, are determined in the presence of different involved parameters. The main theme of our work is to find the behavior in the presence of a temperature-dependent viscosity parameter.

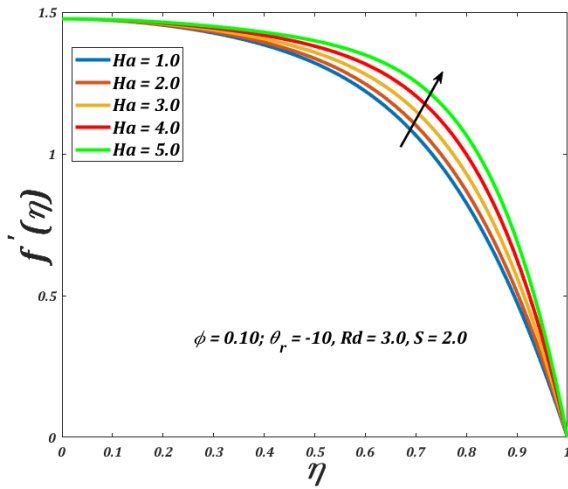


Figure 2.3 Velocity variations with Magnetic parameter

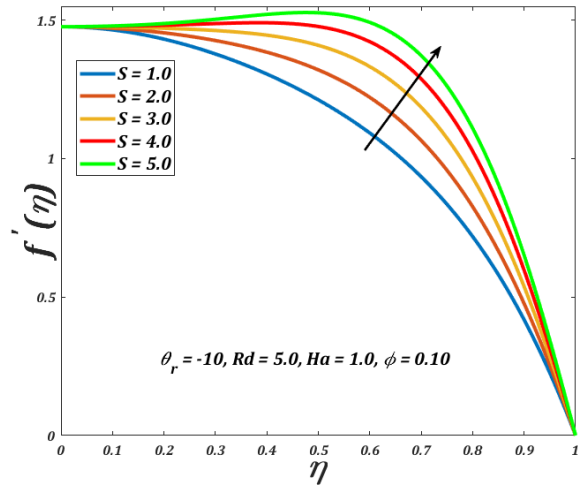


Figure 2.4 Velocity variations with Squeezing parameter

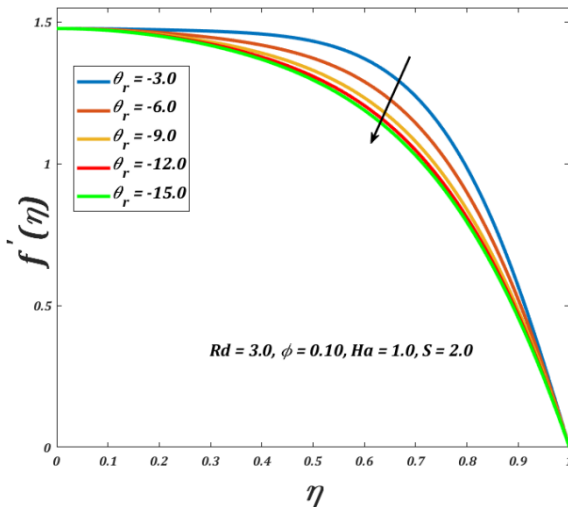


Figure 2.5 Velocity variations with variable Viscosity parameter

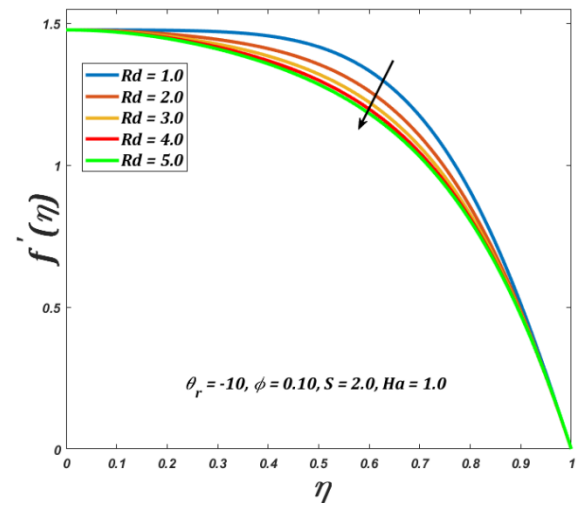


Figure 2.6 Velocity variations with Radiation parameter

Figure (2.2-2.5) represents the velocity profile variations with different physical parameters. Figure 2.2 depicts a boost in velocity with the magnitude of the Hartmann number. The same is

the case of the squeezing parameter as can be noticed in **Figure 2.3**. The velocity profile rises as the squeezing parameters get larger as squeezing walls provide a push to the fluid body along the moving direction. **Figure 2.4** manifests a decline in velocity with a rise in the viscosity parameter.

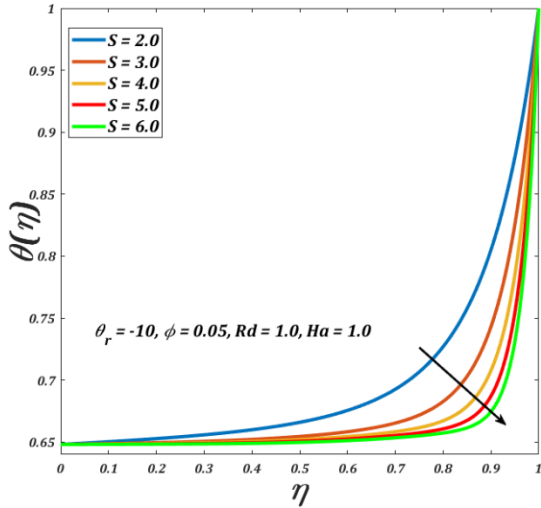


Figure 2.7 Temperature variations versus Squeezing parameter

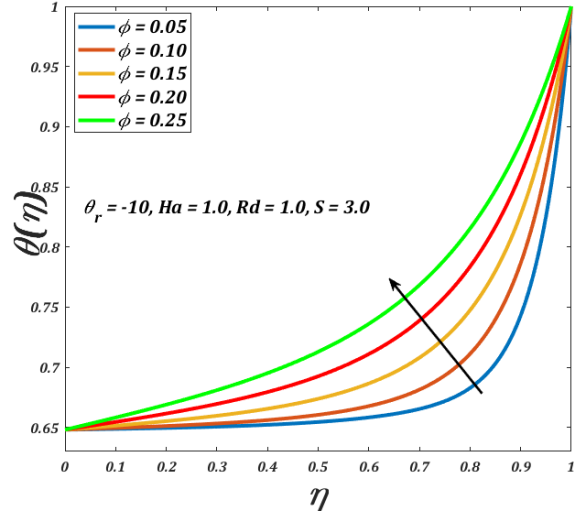


Figure 2.8 Temperature variations versus Volume fraction of SWCNT

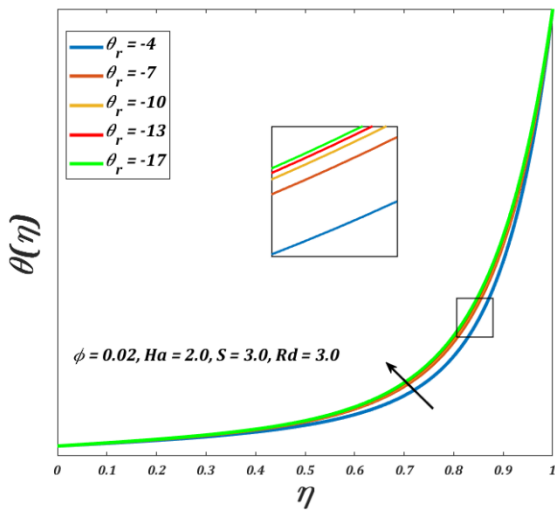


Figure 2.9 Temperature variations versus variable Viscosity parameter

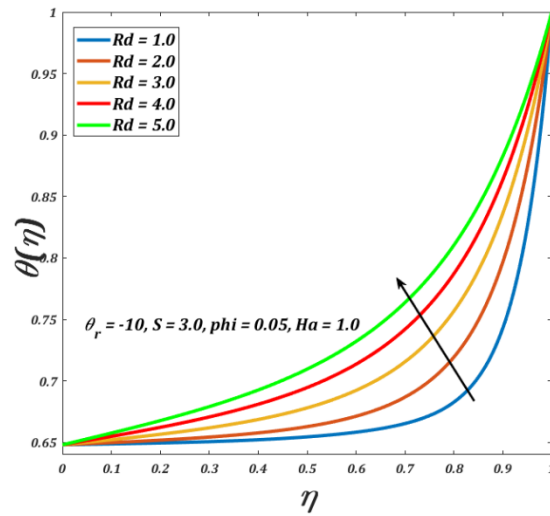


Figure 2.10 Temperature variations versus Radiation parameter

With an increase in radiation parameter heat loss from fluid mass occurs causing fluid more resistive to motion. **Figure 2.5**, therefore shows a decline in velocity with radiation parameters. **Figures (2.6-2.9)** determines the variation of temperature profile with all involve physical

parameters. Since by increasing volume fraction of CNT's, thermal conductivity of nanofluid raise, consequently fluid temperature increases as can be validated from **Figure 2.7**, while a decrease in temperature distribution is observed with rising values of squeezing parameter as can be observed in **Figure 2.6**. A rise in the viscosity parameter heightens the temperature distribution of the nanofluid as evident in **Figure 2.8**. The present study concluded that temperature distribution magnifies with ascending values of radiation parameters as represented in **Figure 2.9**.

Table 2.2 shows that for fixed values of the variable viscosity parameter the Skin-friction coefficient increases with CNT concentration values while the same parameter decreases the intensity of the Nusselt number. **Table 2.3**. Presents the effect on the Nusselt number and skin-friction of the squeezing parameters. The results show that both increase while keeping the variable viscosity parameter constant with the increase in the squeezing parameters.

Table 2.2 Variations in Nusselt number and Skin-friction with volume fraction and viscosity parameter.

$$Ha = 1.0, Rd = 1.0, S = 1.0$$

| θ_r | φ | $-C_f^*$ | N_u^* |
|------------|-----------|----------|---------|
| -10 | 0.025 | 4.47373 | 4.23771 |
| | 0.05 | 4.54218 | 4.08374 |
| | 0.10 | 4.81952 | 3.94902 |
| -15 | 0.025 | 4.32488 | 4.17088 |
| | 0.05 | 4.42293 | 4.03927 |
| | 0.10 | 4.71370 | 3.92875 |
| -20 | 0.025 | 4.27463 | 4.13924 |
| | 0.05 | 4.37796 | 4.01767 |
| | 0.10 | 4.66196 | 3.91836 |

The radiation parameter, when raised in magnitude, increases the strength of Skin friction as well as Nusselt number as shown in **Table 2.4**. A rise in the Skin friction can be observed with a hike in the magnitude of Hartmann's number.

Table 2.3 Variations in Nusselt number and Skin-friction with the Squeezing parameter and viscosity parameter.
 $Ha = 1.0, Rd = 1.0, \varphi = 0.05$

| θ_r | S | $-C_f^*$ | N_u^* |
|------------|------------|----------------|-----------------|
| | 1.0 | 4.54218 | 4.08374 |
| -10 | 2.0 | 5.47507 | 9.49879 |
| | 3.0 | 6.38270 | 15.60775 |
| | 1.0 | 4.42293 | 4.03927 |
| -15 | 2.0 | 5.21024 | 9.15755 |
| | 3.0 | 6.04474 | 14.8807 |
| | 1.0 | 4.37796 | 4.01767 |
| -20 | 2.0 | 5.16436 | 9.01385 |
| | 3.0 | 6.00441 | 14.59559 |

A decrease in Nusselt number can be seen for viscosity parameter magnitude less than 10, where it increases for values of magnitude greater than or equal to 10 as shown in **Table 2.5**. For all numeric obtained for the problem, it is very clear that with a rise in viscosity parameter a decrease in Nusselt number, as well as in Skin friction is observed.

Table 2.4 Variations in Nusselt number and Skin-friction with the Radiations parameter and viscosity parameter.

$$Ha = 1, S = 2, \varphi = 0.05$$

| θ_r | Rd | $-C_f^*$ | N_u^* |
|------------|------|----------|----------|
| | 0.5 | 5.90485 | 10.11312 |
| -10 | 1.0 | 5.47507 | 9.49879 |
| | 2.0 | 5.19173 | 8.67924 |
| | 0.5 | 5.41991 | 9.61867 |
| -15 | 1.0 | 5.21024 | 9.15755 |
| | 2.0 | 5.11223 | 8.51033 |
| | 0.5 | 5.30290 | 9.41917 |
| -20 | 1.0 | 5.16436 | 9.01385 |
| | 2.0 | 5.11572 | 8.43422 |

Table 2.5 Variations in Nusselt number and Skin-friction with Hartman number and viscosity parameter.

$$Rd = 1.0, S = 2, \varphi = 0.05$$

| θ_r | Ha | $-C_f^*$ | N_u^* |
|------------|------|----------|---------|
| | 0.5 | 5.40040 | 9.51577 |
| -10 | 1.0 | 5.47507 | 9.49879 |
| | 2.0 | 5.79730 | 9.45223 |
| | 0.5 | 5.08277 | 9.15113 |

| | | | |
|------------|------------|----------------|----------------|
| -15 | 1.0 | 5.21024 | 9.15755 |
| | 2.0 | 5.70840 | 9.18559 |
| | 0.5 | 5.01713 | 8.99891 |
| -20 | 1.0 | 5.16436 | 9.01385 |
| | 2.0 | 5.73055 | 9.06988 |

3 Micropolar nanofluid flow passing through squeezing walls.

3.1 Introduction

This chapter deals with the inner structure of the fluid material that plays a vital role in fluid flow and thermal behavior of a fluid body. For instance, the existence of two different phases of nanofluids can produce rotational inertia in addition to the linear inertia. The classical Navier stokes equations, however, possess the very limited capability to analyze the flow of fluid based on inner structure. In contrast to the Navier stokes model, the Eringen theory for micropolar fluid can be utilized to discuss the dynamics of the fluid with rotational and spin inertia meticulously. This chapter deals with the effects of rotational and spin motion on the dynamics of fluid in the presence of temperature-dependent viscosity and unsteady MHD field acting in the normal direction to the solid surface.

3.2 Mathematical Description

Let us consider the flow of a micropolar viscous nanofluid between two infinite squeezing plates as shown in **Figure 2.1**. The plates are parallel and are at distant $h(t) = l(1 - \beta t)^{1/2}$ from the origin. The two plates squeezed till they meet at $t = 1/\beta$, where $\beta > 0$. Radiative heat transfer and an unsteady magnetic field is taken into consideration, which is directed normal to the plates, $B(t) = B_0(1 - \beta t)^{-1/2}$ is the applied magnetic field, B_0 is the initial intensity of the applied magnetic field. The effective dynamic viscosity varies with temperature. **Figure 2.1** describes the geometry of the problem.

Taking into considerations the intrinsic mobility of fluid particles, the two-dimensional flow equations are:

$$\frac{\partial \vec{U}}{\partial x} + \frac{\partial \vec{V}}{\partial y} = 0 \tag{3.1}$$

$$\begin{aligned}
& \frac{\partial \bar{U}}{\partial t} + \bar{U} \frac{\partial \bar{U}}{\partial x} + \bar{V} \frac{\partial \bar{U}}{\partial y} \\
&= -\frac{1}{\rho_{nf}} \frac{\partial p}{\partial x} + \frac{1}{\rho_{nf}} \frac{\partial}{\partial x} \left((\mu_{nf} + \kappa) \frac{\partial \bar{U}}{\partial x} \right) + \frac{1}{\rho_{nf}} \frac{\partial}{\partial y} \left((\mu_{nf} + \kappa) \frac{\partial \bar{U}}{\partial y} \right) \\
&+ \frac{\kappa}{\rho_{nf}} \frac{\partial \bar{N}}{\partial y} - \sigma B^2(t) \bar{U}
\end{aligned} \tag{3.2}$$

$$\begin{aligned}
& \frac{\partial \bar{V}}{\partial t} + \bar{U} \frac{\partial \bar{V}}{\partial x} + \bar{V} \frac{\partial \bar{V}}{\partial y} \\
&= -\frac{1}{\rho_{nf}} \frac{\partial p}{\partial y} - \frac{1}{\rho_{nf}} \frac{\partial}{\partial x} \left((\mu_{nf} + \kappa) \frac{\partial \bar{V}}{\partial x} \right) - \frac{\kappa}{\rho_{nf}} + \frac{1}{\rho_{nf}} \frac{\partial}{\partial y} \left((\mu_{nf} + \kappa) \frac{\partial \bar{V}}{\partial y} \right) \\
&- \frac{\kappa}{\rho_{nf}} \frac{\partial \bar{N}}{\partial x}
\end{aligned} \tag{3.3}$$

$$\frac{\partial \bar{N}}{\partial t} + \bar{U} \frac{\partial \bar{N}}{\partial x} + \bar{V} \frac{\partial \bar{N}}{\partial y} = \frac{1}{\rho_{nf} j} \frac{\partial}{\partial y} \left(\gamma^* \frac{\partial \bar{N}}{\partial y} \right) - \frac{\kappa}{\rho_{nf} j} \left(2\bar{N} + \frac{\partial \bar{U}}{\partial y} \right) \tag{3.4}$$

$$\frac{\partial \bar{T}}{\partial t} + \bar{U} \frac{\partial \bar{T}}{\partial x} + \bar{V} \frac{\partial \bar{T}}{\partial y} = \alpha_{nf} \left(\frac{\partial^2 \bar{T}}{\partial y^2} \right) - \frac{1}{(\rho C_p)_{nf}} \frac{\partial q_r}{\partial y} \tag{3.5}$$

For the above system the relevant boundary conditions are:

$$\begin{aligned}
& \frac{\partial \bar{U}}{\partial y} = 0, \quad \bar{V} = 0, \quad \frac{\partial \bar{N}}{\partial y} = 0, \quad \frac{\partial \bar{T}}{\partial y} = 0 \quad \text{at} \quad y = 0, \\
& \bar{U} = 0, \quad \bar{V} = \frac{dh}{dt}, \quad \bar{N} = -s \frac{\partial \bar{U}}{\partial y}, \quad \bar{T} = T_h \quad \text{at} \quad y = h(t)
\end{aligned} \tag{3.6}$$

Here \bar{N} represents angular velocity of fluid particles.

We introduce dimensionless functions f , θ , g , and a similarity variable η to convert the governing set of partial differential equations to a system of similar ordinary differential equations with the transformations, defined as:

$$\vec{U} = \frac{\beta x}{2(1-\beta t)} f'(\eta), \quad \vec{V} = \frac{-\beta l}{2(1-\beta t)^{\frac{1}{2}}} f(\eta), \quad \vec{N} = \frac{-\beta x}{2l(1-\beta t)^{\frac{3}{2}}} g(\eta),$$

$$\theta = \frac{\vec{T} - T_c}{T_h - T_c}, \quad \eta = \frac{y}{l(1-\beta t)^{\frac{1}{2}}}$$

Implicating the above transformations and dropping out the pressure gradient term by increasing the order of differentiation, the continuity equation satisfies identically while the momentum and the energy equations reduce to the below nonlinear differential system:

$$\begin{aligned} f^{iv} + \frac{f''\theta''}{\theta_r \left(1 - \frac{\theta}{\theta_r}\right)} + \frac{f'''\theta'}{\theta_r \left(1 - \frac{\theta}{\theta_r}\right)} + \frac{f''\theta'^2}{\theta_r^2 \left(1 - \frac{\theta}{\theta_r}\right)^2} - Ha^2 f'' \\ - A_1 S \left(1 - \frac{\theta}{\theta_r}\right) (\eta f'''' + 3f'' + f'f'' - ff''') + K(1-\phi)^{2.5} f''' \\ + K(1-\phi)^{2.5} g' = 0 \end{aligned} \quad (3.7)$$

$$\begin{aligned} \frac{1}{A_1} \left(\frac{1}{\left(1 - \frac{\theta}{\theta_r}\right)} + \frac{K(1-\phi)^{2.5}}{2} \right) g'' + \frac{1}{A_1} \frac{\theta' g'}{\theta_r \left(1 - \frac{\theta}{\theta_r}\right)^2} + \frac{2S}{A_1} K(1-\phi)^{2.5} (f'' - 2g) \\ + S(fg' - f'g - 3g - \eta g') = 0 \end{aligned} \quad (3.8)$$

$$A_2 \theta'' - A_3 (f\theta' + \eta\theta') = 0 \quad (3.9)$$

$$\begin{aligned} f'' = 0, f = 0, g' = 0, \theta' = 0 \text{ at } \eta = 0 \\ f' = 0, f = 1, g = -N_0 f''(1), \theta = 1 \text{ at } \eta = 1 \end{aligned} \quad (3.10)$$

Where,

$$\begin{aligned} A_1 = (1-\phi)^{2.5} \left[(1-\phi) + \phi \frac{\rho_{CNT}}{\rho_{f\infty}} \right], A_2 = \left(1 + \frac{4}{3\epsilon_1} Rd \right), A_3 = S \frac{\epsilon_2}{\epsilon_1} Pr, \\ Rd = \frac{4\sigma_e T^3}{K_{f\infty} \beta_R}, S = \frac{\beta l^2}{2\nu_{f\infty}}, Pr = \frac{\mu_{f\infty} (\rho C_p)_{f\infty}}{\rho_{f\infty} K_{f\infty}} \end{aligned}$$

The dimensionless shear stress and the thermal gradient coefficient is determined by the expression

$$C_f = \frac{1}{\rho_{nf} \left(\frac{dh}{dt}\right)^2} \left((\mu_{nf} + \kappa) \frac{\partial \bar{U}}{\partial y} + \kappa N_0 \right)_{y=h(t)} \text{ and } Nu = \left(\left(1 + \frac{4}{3\epsilon_1} Rd\right) \frac{lK_{nf}}{K_f T_h} \frac{\partial \bar{T}}{\partial y} \right)_{y=h(t)}, \text{ respectively,}$$

which is the dimensionless form given as

$$C_f^* = C_f \frac{Re_x l^2}{2x^2} \sqrt{1 - \beta t} = \frac{1}{A_1 \left(1 - \frac{1}{\theta_r}\right)} \left(1 + (1 - N_0)K\right) f''(1), \quad N_u^* = \epsilon_1 \left(1 + \frac{4}{3\epsilon_1} Rd\right) \theta'(1)$$

3.3 Solution procedure

The extremely non-linear partial differential equations enforcing assumed physics are written in dimensionless form and then transformed by selecting appropriate transformations into a set of similar ordinary differential equations. Equations (3.7 – 3.9) are the transformed differential equations and (3.10) represent the considered boundary conditions. The proceeding step is to work out a solution to the above equations numerically. The equation governing linear momentum is an ordinary differential equation of the fourth order, while the equation of energy and angular momentum are ordinary differential equations of the second order. Five new dependent variables $u, v, w, q, \text{ and } m$ is introduced to convert the governing system of equations into a set of first-order ordinary differential equations, which are given below:

$$f' = u \tag{3.11}$$

$$u' = v \tag{3.12}$$

$$v' = w \tag{3.13}$$

$$g' = q \tag{3.14}$$

$$\theta' = m \tag{3.15}$$

$$\begin{aligned}
& w' - \frac{2}{\theta_r} w' \theta + \frac{1}{\theta_r^2} w' \theta^2 + \frac{1}{\theta_r^2} w m + \frac{1}{\theta_r} v m' - \frac{1}{\theta_r^2} w m \theta - \frac{1}{\theta_r^2} v m' \theta + \frac{1}{\theta_r^2} v m^2 - H a^2 v \\
& + \frac{2}{\theta_r} H a^2 v \theta - \frac{1}{\theta_r} H a^2 v \theta^2 - A_1 S \eta w - 3 A_1 S v - 5 A_1 S u v - A_1 S f v + \frac{3}{\theta_r} A_1 S \eta w \theta \\
& + \frac{9}{\theta_r} A_1 S v \theta + \frac{15}{\theta_r} A_1 S u v \theta + \frac{3}{\theta_r} A_1 S f v \theta - \frac{9}{\theta_r^2} A_1 S v \theta^2 - \frac{15}{\theta_r^2} A_1 S u v \theta^2 \\
& - \frac{3}{\theta_r^2} A_1 S f v \theta^2 + \frac{1}{\theta_r^3} A_1 S \eta \theta^3 + \frac{3}{\theta_r^3} A_1 S v \theta^3 + \frac{5}{\theta_r^3} A_1 S u v \theta^3 + \frac{1}{\theta_r^3} A_1 S f v \theta^3 \\
& + \frac{1}{\theta_r} A_1 S \eta v m + \frac{2}{\theta_r} A_1 S u m + \frac{2}{\theta_r} A_1 S u^2 m - \frac{2}{\theta_r^2} A_1 S \eta v m \theta - \frac{4}{\theta_r^2} A_1 S u m \theta \\
& - \frac{4}{\theta_r^2} A_1 S u^2 m \theta + \frac{1}{\theta_r^3} A_1 S \eta v m \theta^2 + \frac{2}{\theta_r^3} A_1 S u m \theta^2 + \frac{2}{\theta_r^3} A_1 S u^2 m \theta^2 + K_1 (w \\
& - \frac{2}{\theta_r} w \theta + \frac{1}{\theta_r^2} w \theta^2 + q - \frac{2}{\theta_r} \theta q + \frac{1}{\theta_r^2} \theta^2 q) = 0
\end{aligned} \tag{3.16}$$

$$\begin{aligned}
& q' - \frac{1}{\theta_r} \theta q' + \frac{1}{2} K_1 q' - \frac{1}{\theta_r} K_1 \theta q' + \frac{1}{2 \theta_r^2} \theta^2 q' + \frac{1}{\theta_r} m q \\
& + 2 S K_1 \left(v - \frac{2}{\theta_r} v \theta + \frac{1}{\theta_r^2} v \theta^2 - 2 g + \frac{4}{\theta_r} g \theta - \frac{2}{\theta_r^2} g \theta^2 \right) \\
& + A_1 S \left(f q - f g - 3 g - \eta q - \frac{2}{\theta_r} f q \theta + \frac{2}{\theta_r} f g \theta + \frac{6}{\theta_r} g \theta + \frac{2}{\theta_r} \eta q \theta + \frac{1}{\theta_r^2} f q \theta^2 \right. \\
& \left. - \frac{1}{\theta_r^2} f g \theta^2 - \frac{3}{\theta_r^2} g \theta^2 - \frac{1}{\theta_r^2} \eta q \theta^2 \right) = 0
\end{aligned} \tag{3.17}$$

$$A_2 m' - A_3 \eta m - A_3 f m = 0 \tag{3.18}$$

The associated boundary conditions are:

$$v = 0, \quad f = 0, \quad q = 0, \quad m = 0 \text{ at } \eta = 0$$

$$u = 0, \quad f = 1, \quad g = -N_0 f''(1), \quad \theta = 1 \text{ at } \eta = 1$$

We now find the finite difference replacement, which will switch a set of algebraic equations in place of the above differential equations. For the purpose, we reconsider the working domain as a rectangular net in the (x, η) -plan as in **Figure 2.2**.

Applying the finite difference scheme as discussed in chapter 2 on the above system of equations. The first five equations are discretized by centering at $(x^i, \eta_{j-1/2})$ where the last three equations are discretized by centering at $(x^{i-1/2}, \eta_{j-1/2})$. The resulting system of equations becomes

$$f_j^i = f_{j-1}^i + \frac{h_j}{2} (u_j^i + u_{j-1}^i) \quad (3.19)$$

$$u_j^i = u_{j-1}^i + \frac{h_j}{2} (v_j^i + v_{j-1}^i) \quad (3.20)$$

$$v_j^i = v_{j-1}^i + \frac{h_j}{2} (w_j^i + w_{j-1}^i) \quad (3.21)$$

$$g_j^i = g_{j-1}^i + \frac{h_j}{2} (q_j^i + q_{j-1}^i) \quad (3.22)$$

$$\theta_j^i = \theta_{j-1}^i + \frac{h_j}{2} (m_j^i + m_{j-1}^i) \quad (3.23)$$

$$\begin{aligned}
& \left[\frac{(w_j - w_{j-1})}{h_j} + \frac{1}{\theta_r^2} \frac{(w_j - w_{j-1})(\theta_j + \theta_{j-1})^2}{h_j} - \frac{2}{\theta_r} \frac{(w_j - w_{j-1})(\theta_j + \theta_{j-1})}{h_j} \right. \\
& + \frac{1}{\theta_r} \frac{(w_j + w_{j-1})(m_j + m_{j-1})}{2} - \frac{1}{\theta_r^2} \frac{(w_j + w_{j-1})(\theta_j + \theta_{j-1})(m_j + m_{j-1})}{2} \\
& + \frac{1}{\theta_r} \frac{(v_j + v_{j-1})(m_j - m_{j-1})}{2} - \frac{1}{\theta_r^2} \frac{(v_j + v_{j-1})(\theta_j + \theta_{j-1})(m_j - m_{j-1})}{2} \\
& + \frac{1}{\theta_r^2} \frac{(v_j + v_{j-1})(m_j + m_{j-1})^2}{2} - Ha^2 \frac{(v_j + v_{j-1})}{2} \\
& + \frac{2}{\theta_r} Ha^2 \frac{(v_j + v_{j-1})(\theta_j + \theta_{j-1})}{2} - \frac{1}{\theta_r^2} Ha^2 \frac{(v_j + v_{j-1})(\theta_j + \theta_{j-1})^2}{4} \\
& - A_1 S \eta \frac{(w_j + w_{j-1})}{2} - \frac{3}{2} A_1 S \frac{(v_j + v_{j-1})}{2} + A_1 S \frac{(f_j + f_{j-1})(w_j + w_{j-1})}{2} \\
& + \frac{3}{\theta_r} A_1 S \eta \frac{(w_j + w_{j-1})(\theta_j + \theta_{j-1})}{2} + \frac{9}{\theta_r} A_1 S \frac{(v_j + v_{j-1})(\theta_j + \theta_{j-1})}{2} \\
& - \frac{3}{\theta_r} A_1 S \frac{(f_j + f_{j-1})(w_j + w_{j-1})(\theta_j + \theta_{j-1})}{2} \\
& - \frac{3}{\theta_r^2} A_1 S \eta \frac{(w_j + w_{j-1})(\theta_j + \theta_{j-1})^2}{2} - \frac{9}{2\theta_r^2} \frac{(v_j + v_{j-1})(\theta_j + \theta_{j-1})^2}{2} \\
& + \frac{3}{\theta_r^2} A_1 S \frac{(f_j + f_{j-1})(w_j + w_{j-1})(\theta_j + \theta_{j-1})^2}{2} \\
& + \frac{1}{\theta_r^3} A_1 S \eta \frac{(w_j + w_{j-1})(\theta_j + \theta_{j-1})^3}{2} + \frac{3}{2\theta_r^3} A_1 S \eta \frac{(v_j + v_{j-1})(\theta_j + \theta_{j-1})^3}{2} \\
& - \frac{1}{\theta_r^3} A_1 S \frac{(f_j + f_{j-1})(v_j + v_{j-1})(\theta_j + \theta_{j-1})^3}{2} + K_1 \left(\frac{(w_j + w_{j-1})}{2} \right. \\
& - \frac{2}{\theta_r} \frac{(w_j + w_{j-1})(\theta_j + \theta_{j-1})}{2} + \frac{1}{\theta_r^2} \frac{(w_j + w_{j-1})(\theta_j + \theta_{j-1})^2}{2} + \frac{(q_j + q_{j-1})}{2} \\
& \left. - \frac{2}{\theta_r} \frac{(q_j + q_{j-1})(\theta_j + \theta_{j-1})}{2} + \frac{1}{\theta_r^2} \frac{(q_j + q_{j-1})(\theta_j + \theta_{j-1})^2}{2} \right)^i = M_{j-1/2} \tag{3.24}
\end{aligned}$$

$$\begin{aligned}
& \frac{(q_j - q_{j-1})}{h_j} - \frac{1}{\theta_r} \frac{(q_j - q_{j-1})(\theta_j + \theta_{j-1})}{h_j} + \frac{1}{2} K_1 \frac{(q_j - q_{j-1})}{h_j} - \frac{1}{\theta_r} K_1 \frac{(q_j - q_{j-1})(\theta_j + \theta_{j-1})}{2} \\
& + \frac{1}{2\theta_r^2} K_1 \frac{(q_j - q_{j-1})(\theta_j + \theta_{j-1})^2}{h_j} + \frac{1}{\theta_r} \frac{(m_j + m_{j-1})(q_j + q_{j-1})}{2} \\
& + 2SK_1 \left(\frac{(v_j + v_{j-1})}{2} - \frac{2}{\theta_r} \frac{(v_j + v_{j-1})(\theta_j + \theta_{j-1})}{2} \right. \\
& + \frac{1}{\theta_r^2} \frac{(v_j + v_{j-1})(\theta_j + \theta_{j-1})^2}{2} - (g_j + g_{j-1}) + \frac{1}{\theta_r} (g_j + g_{j-1})(\theta_j + \theta_{j-1}) \\
& \left. - \frac{1}{\theta_r^2} (g_j + g_{j-1}) \frac{(\theta_j + \theta_{j-1})^2}{4} \right) \\
& + A_1 S \left(\frac{(f_j + f_{j-1})(q_j + q_{j-1})}{2} - \frac{(f_j + f_{j-1})(g_j + g_{j-1})}{2} - 3 \frac{(g_j + g_{j-1})}{2} \right. \\
& - \eta \frac{(q_j + q_{j-1})}{2} - \frac{2}{\theta_r} \frac{(f_j + f_{j-1})(q_j + q_{j-1})(\theta_j + \theta_{j-1})}{2} \\
& + \frac{2}{\theta_r} \frac{(f_j + f_{j-1})(\theta_j + \theta_{j-1})(g_j + g_{j-1})}{2} + \frac{6}{\theta_r} \frac{(g_j + g_{j-1})(\theta_j + \theta_{j-1})}{2} \\
& + \frac{2}{\theta_r} \eta \frac{(q_j + q_{j-1})(\theta_j + \theta_{j-1})}{2} + \frac{1}{\theta_r^2} \frac{(f_j + f_{j-1})(q_j + q_{j-1})(\theta_j + \theta_{j-1})^2}{2} \\
& - \frac{1}{\theta_r^2} \frac{(f_j + f_{j-1})(\theta_j + \theta_{j-1})^2 (g_j + g_{j-1})}{2} - \frac{3}{\theta_r^2} \frac{(g_j + g_{j-1})(\theta_j + \theta_{j-1})^2}{2} \\
& \left. - \frac{1}{\theta_r^2} \eta \frac{(q_j + q_{j-1})(\theta_j + \theta_{j-1})^2}{2} \right) = N_{j-1/2} \tag{3.25}
\end{aligned}$$

$$[A_2 \frac{(m_j - m_{j-1})}{h_j} - A_3 \eta \frac{(m_j + m_{j-1})}{2} - A_3 \frac{(f_j + f_{j-1})(m_j + m_{j-1})}{2}]^i = P_{j-1/2} \tag{3.26}$$

Where

$$\begin{aligned}
M_{j-1/2} = & -[(w')_{j-\frac{1}{2}} - \frac{2}{\theta_r}(w'\theta)_{j-\frac{1}{2}} + \frac{1}{\theta_r^2}(w'\theta^2)_{j-\frac{1}{2}} + \frac{1}{\theta_r^2}(wm)_{j-\frac{1}{2}} + \frac{1}{\theta_r}(vm')_{j-\frac{1}{2}} \\
& - \frac{1}{\theta_r^2}(wm\theta)_{j-\frac{1}{2}} - \frac{1}{\theta_r^2}(vm'\theta)_{j-\frac{1}{2}} + \frac{1}{\theta_r^2}(vm^2)_{j-\frac{1}{2}} - Ha^2v_{j-\frac{1}{2}} + \frac{2}{\theta_r}Ha^2(v\theta)_{j-\frac{1}{2}} \\
& - \frac{1}{\theta_r}Ha^2(v\theta^2)_{j-\frac{1}{2}} - A_1S(\eta w)_{j-\frac{1}{2}} - 3A_1Sv_{j-\frac{1}{2}} - 5A_1S(uv)_{j-\frac{1}{2}} - A_1S(fv)_{j-\frac{1}{2}} \\
& + \frac{3}{\theta_r}A_1S(\eta w\theta)_{j-\frac{1}{2}} + \frac{9}{\theta_r}A_1S(v\theta)_{j-\frac{1}{2}} + \frac{15}{\theta_r}A_1S(uv\theta)_{j-\frac{1}{2}} + \frac{3}{\theta_r}A_1S(fv\theta)_{j-\frac{1}{2}} \\
& - \frac{9}{\theta_r^2}A_1S(v\theta^2)_{j-\frac{1}{2}} - \frac{15}{\theta_r^2}A_1S(uv\theta^2)_{j-\frac{1}{2}} - \frac{3}{\theta_r^2}A_1S(fv\theta^2)_{j-\frac{1}{2}} + \frac{1}{\theta_r^3}A_1S(\eta\theta^3)_{j-\frac{1}{2}} \\
& + \frac{3}{\theta_r^3}A_1S(v\theta^3)_{j-\frac{1}{2}} + \frac{5}{\theta_r^3}A_1S(uv\theta^3)_{j-\frac{1}{2}} + \frac{1}{\theta_r^3}A_1S(fv\theta^3)_{j-\frac{1}{2}} + \frac{1}{\theta_r}A_1S(\eta vm)_{j-\frac{1}{2}} \\
& + \frac{2}{\theta_r}A_1S(um)_{j-\frac{1}{2}} + \frac{2}{\theta_r}A_1S(u^2m)_{j-\frac{1}{2}} - \frac{2}{\theta_r^2}A_1S(\eta vm\theta)_{j-\frac{1}{2}} - \frac{4}{\theta_r^2}A_1S(um\theta)_{j-\frac{1}{2}} \\
& - \frac{4}{\theta_r^2}A_1S(u^2m\theta)_{j-\frac{1}{2}} + \frac{1}{\theta_r^3}A_1S(\eta vm\theta^2)_{j-\frac{1}{2}} + \frac{2}{\theta_r^3}A_1S(um\theta^2)_{j-\frac{1}{2}} \\
& + \frac{2}{\theta_r^3}A_1S(u^2m\theta^2)_{j-\frac{1}{2}} + K_1(w_{j-\frac{1}{2}} - \frac{2}{\theta_r}(w\theta)_{j-\frac{1}{2}} + \frac{1}{\theta_r^2}(w\theta^2)_{j-\frac{1}{2}} + q_{j-\frac{1}{2}} \\
& - \frac{2}{\theta_r}(\theta q)_{j-\frac{1}{2}} + \frac{1}{\theta_r^2}(\theta^2 q)_{j-\frac{1}{2}})]^{i-1} \tag{3.27}
\end{aligned}$$

$$\begin{aligned}
N_{j-1/2} = & -[q'_{j-\frac{1}{2}} - \frac{1}{\theta_r}(\theta q')_{j-\frac{1}{2}} + \frac{1}{2}K_1q'_{j-\frac{1}{2}} - \frac{1}{\theta_r}K_1(\theta q')_{j-\frac{1}{2}} + \frac{1}{2\theta_r^2}(\theta^2 q')_{j-\frac{1}{2}} + \frac{1}{\theta_r}(mq)_{j-\frac{1}{2}} \\
& + 2SK_1\left(v_{j-\frac{1}{2}} - \frac{2}{\theta_r}(v\theta)_{j-\frac{1}{2}} + \frac{1}{\theta_r^2}(v\theta^2)_{j-\frac{1}{2}} - 2g_{j-\frac{1}{2}} + \frac{4}{\theta_r}(g\theta)_{j-\frac{1}{2}} \right. \\
& \left. - \frac{2}{\theta_r^2}(g\theta^2)_{j-\frac{1}{2}}\right) \\
& + A_2S\left((fq)_{j-\frac{1}{2}} - (fg)_{j-\frac{1}{2}} - 3g_{j-\frac{1}{2}} - (\eta q)_{j-\frac{1}{2}} - \frac{2}{\theta_r}(fq\theta)_{j-\frac{1}{2}} + \frac{2}{\theta_r}(fg\theta)_{j-\frac{1}{2}} \right. \\
& + \frac{6}{\theta_r}(g\theta)_{j-\frac{1}{2}} + \frac{2}{\theta_r}(\eta q\theta)_{j-\frac{1}{2}} + \frac{1}{\theta_r^2}(fq\theta^2)_{j-\frac{1}{2}} - \frac{1}{\theta_r^2}(fg\theta^2)_{j-\frac{1}{2}} - \frac{3}{\theta_r^2}(g\theta^2)_{j-\frac{1}{2}} \\
& \left. - \frac{1}{\theta_r^2}(\eta q\theta^2)_{j-\frac{1}{2}}\right)]^{i-1} \tag{3.28}
\end{aligned}$$

$$P_{j-1/2} = -[A_2(m')_{j-\frac{1}{2}} - A_3\eta m_{j-\frac{1}{2}} - A_3(fm)_{j-\frac{1}{2}}]^{i-1} \quad (3.29)$$

Since the superscripts “ i ” represent unknown terms and “ $i - 1$ ” represents terms that are already known, where $0 \leq j \leq J$ shows the number of iterations along η direction. Hence $M_{j-1/2}$ and $N_{j-1/2}$ and $P_{j-1/2}$ contains only known terms.

We now incorporate Newton’s linearization technique. We replace f, u, v, w, g, q, θ and m by $f + \delta f, u + \delta u, v + \delta v, w + \delta w, g + \delta g, q + \delta q, \theta + \delta \theta$ and $m + \delta m$ respectively, and write the resulting equations into the form given below:

$$\delta f_j - \delta f_{j-1} - \frac{h_j}{2}(\delta u_j + \delta u_{j-1}) = (r_1)_j \quad 3.30$$

$$\delta u_j - \delta u_{j-1} - \frac{h_j}{2}(\delta v_j + \delta v_{j-1}) = (r_2)_j \quad 3.31$$

$$\delta v_j - \delta v_{j-1} - \frac{h_j}{2}(\delta w_j + \delta w_{j-1}) = (r_3)_j \quad 3.32$$

$$\delta g_j - \delta g_{j-1} - \frac{h_j}{2}(\delta q_j + \delta q_{j-1}) = (r_4)_j \quad 3.33$$

$$\delta \theta_j - \delta \theta_{j-1} - \frac{h_j}{2}(\delta m_j + \delta m_{j-1}) = (r_5)_j \quad 3.34$$

$$\begin{aligned} (a_1)_j \delta v_j + (a_2)_j \delta v_{j-1} + (a_3)_j \delta u_j + (a_4)_j \delta u_{j-1} + (a_5)_j \delta f_j + (a_6)_j \delta f_{j-1} + (a_7)_j \delta w_j \\ + (a_8)_j \delta w_{j-1} + (a_9)_j \delta \theta_j + (a_{10})_j \delta \theta_{j-1} + (a_{11})_j \delta m_j + (a_{12})_j \delta m_{j-1} \\ + (a_{13})_j \delta g_j + (a_{14})_j \delta g_{j-1} + (a_{15})_j \delta q_j + (a_{16})_j \delta q_{j-1} = (r_6)_j \end{aligned} \quad 3.35$$

$$\begin{aligned} (b_1)_j \delta v_j + (b_2)_j \delta v_{j-1} + (b_3)_j \delta u_j + (b_4)_j \delta u_{j-1} + (b_5)_j \delta f_j + (b_6)_j \delta f_{j-1} + (b_7)_j \delta w_j \\ + (b_8)_j \delta w_{j-1} + (b_9)_j \delta \theta_j + (b_{10})_j \delta \theta_{j-1} + (b_{11})_j \delta m_j + (b_{12})_j \delta m_{j-1} \\ + (b_{13})_j \delta g_j + (b_{14})_j \delta g_{j-1} + (b_{15})_j \delta q_j + (b_{16})_j \delta q_{j-1} = (r_7)_j \end{aligned} \quad 3.36$$

$$\begin{aligned}
& (c_1)_j \delta v_j + (c_2)_j \delta v_{j-1} + (c_3)_j \delta u_j + (c_4)_j \delta u_{j-1} + (c_5)_j \delta f_j + (c_6)_j \delta f_{j-1} + (c_7)_j \delta w_j \\
& + (c_8)_j \delta w_{j-1} + (c_9)_j \delta \theta_j + (c_{10})_j \delta \theta_{j-1} + (c_{11})_j \delta m_j + (c_{12})_j \delta m_{j-1} + (c_{13})_j \delta g_j \\
& + (c_{14})_j \delta g_{j-1} + (c_{15})_j \delta q_j + (c_{16})_j \delta q_{j-1} = (r_8)_j
\end{aligned} \tag{3.37}$$

The above system of linearized equations is now set into matrix-vector form as:

$$A\varphi = R \tag{3.38}$$

A is a block tri-diagonal matrix system given below:

$$A = \begin{bmatrix} [A_1] & [C_1] & & & & & & & \\ [B_1] & [A_2] & \ddots & & & & & & \\ & & \ddots & \ddots & & & & & \\ & & & \ddots & \ddots & & & & \\ & & & & [B_{j-1}] & & [A_{j-1}] & & [C_{j-1}] \\ & & & & & & [B_j] & & [A_j] \end{bmatrix}$$

$$\varphi = \begin{bmatrix} [\delta_1] \\ [\delta_2] \\ \vdots \\ [\delta_j] \end{bmatrix}, R = \begin{bmatrix} [R_1] \\ [R_2] \\ \vdots \\ [R_j] \end{bmatrix}, [R_j] = \begin{bmatrix} (r_1)_j \\ (r_2)_j \\ \vdots \\ (r_8)_j \end{bmatrix}, \text{where } [\delta_1] = \begin{bmatrix} \delta w_0 \\ \delta q_0 \\ \delta m_0 \\ \delta f_1 \\ \delta v_1 \\ \delta w_1 \\ \delta q_1 \\ \delta m_1 \end{bmatrix}, [\delta_j] = \begin{bmatrix} \delta u_{j-1} \\ \delta g_{j-1} \\ \delta \theta_{j-1} \\ \delta f_j \\ \delta v_j \\ \delta w_j \\ \delta q_j \\ \delta m_j \end{bmatrix}, \quad 2 \leq j \leq J$$

This system is then solved with the block elimination technique by splitting A into a lower and upper triangular matrix and implementing matrix algebra. This very last step is programmed in MATLAB.

For the purpose of solution verification a numerical comparison with C.Y.Wang[40] is presented, who solved the squeezing problem with the same conditions by a series solution method. Statistics obtained in both studies are in very good agreement with each other as can be observed in **Table 3.1**.

Table 3.1 Comparison Table for velocity gradient near the plates $Ha = 0$, $Rd = 0$, $\varphi = 0$,

| S | $f''(1)$ | |
|---------|----------------|------------|
| | C. Y. Wang[40] | Keller Box |
| -0.9952 | -2.410 | -2.13709 |
| -0.4997 | -2.7161 | -2.53844 |
| -0.100 | -2.9452 | -2.86887 |
| 0.0 | -3.000 | -2.95249 |
| 0.11576 | -3.0622 | -3.05085 |
| 0.4138 | -3.2160 | -3.31582 |
| 2.081 | -3.910 | -4.9530 |

3.4 Graphical Results

Computational results are plotted using MATLAB plot facility and with Tecplot software. These graphical results represent the behavior of quantities of physical interest such as temperature, velocity, Nusselt number and Skin friction with various parameters that are considered in the problem.

Figure 3.1 and **Figure 3.2** depicts the streamlines pattern and velocity vector behavior of the assumed flow situation respectively. The flow is analyzed in the region between the origin and plates. Since origin split the channel into two symmetrical geometry with identical flow conditions, the graphical results are plotted only for one portion *i. e* $0 \leq \eta \leq 1$.

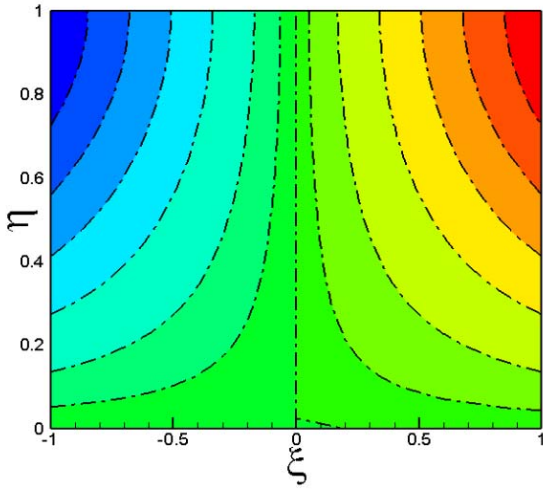


Figure 3.1 Streamlines patterns

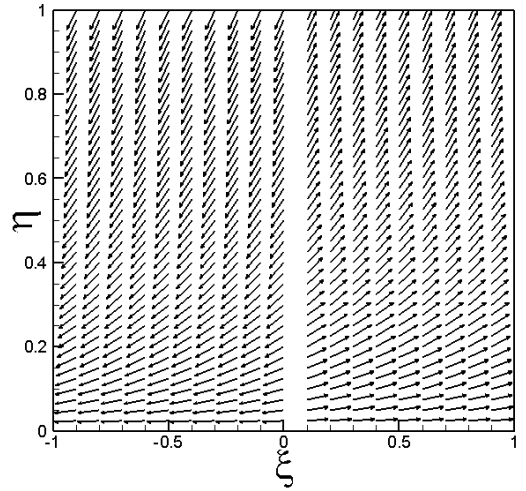


Figure 3.2 Velocity vectors

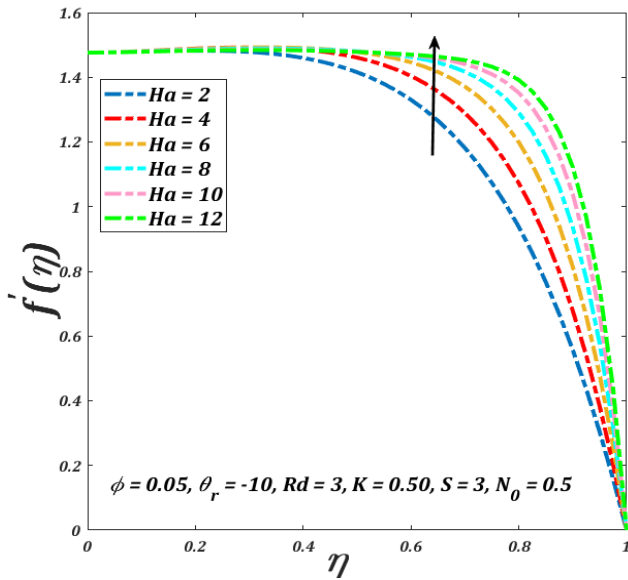


Figure 3.3 Velocity distribution profile with Magnetic parameter

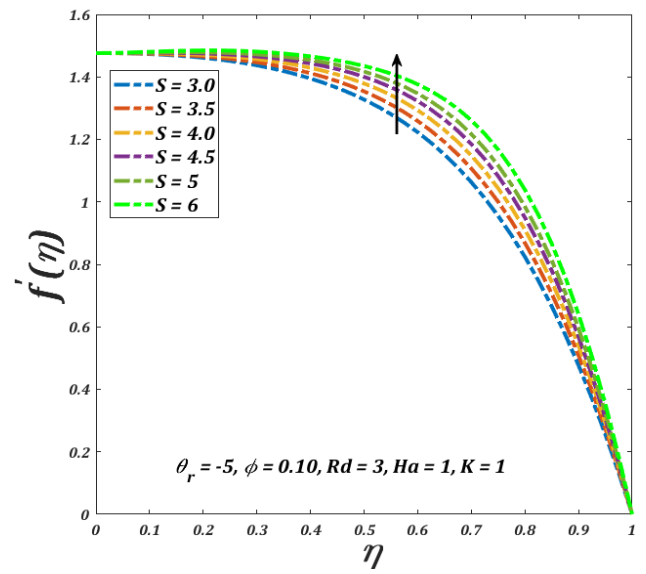


Figure 3.4 Velocity distribution profile with Squeezing parameter

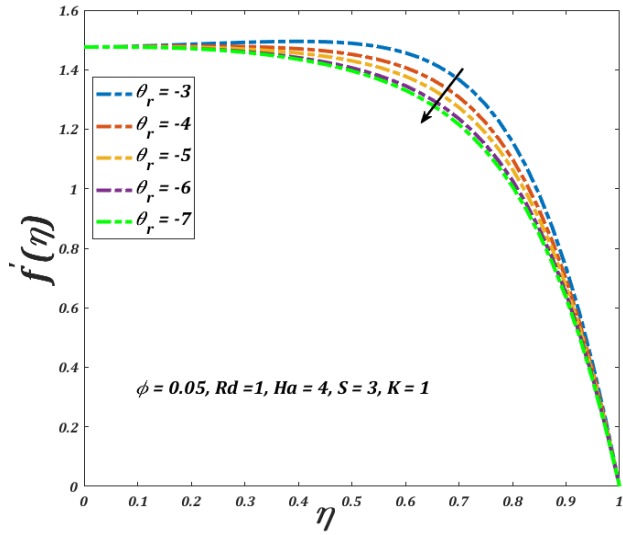


Figure 3.5 Velocity distribution profile with variable Viscosity parameter

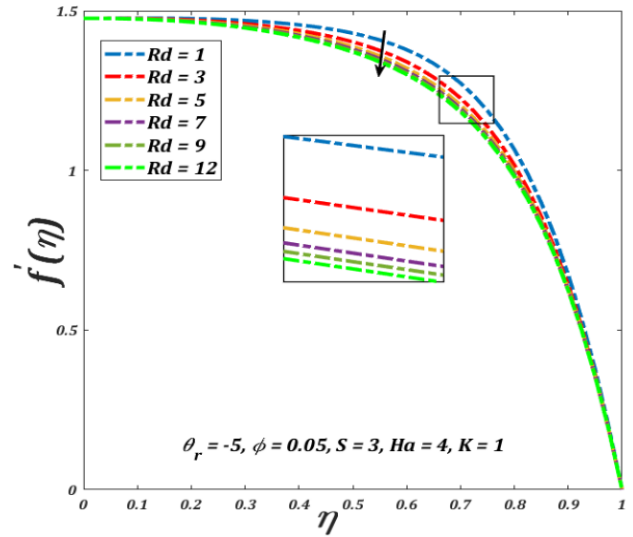


Figure 3.6 Velocity distribution profile with Radiation parameter

It has been observed that for squeezing plates the flow momentum away from the origin is strengthened with the magnitude of the applied magnetic field. Fluid velocity is maximum near the origin while it reduces toward the solid walls. $S > 0$ represents the case when both plates move towards each other. Evidently from **Figure 3.4**, the velocity distribution in the field rises with values of the squeezing parameter. The behavior can be justified with the development of pressure by the moving walls on the incompressible fluid material. The cohesive forces of the fluid material enhance the resisting strength of solid boundaries, the velocity profile as shown in **Figure 3.5** falls with the rise in the magnitude of the viscosity parameter. Since viscosity is inversely proportional to temperature, the loss of heat through radiation amplifies the cohesive forces. An increase in radiation parameter, therefore, resists the flow. The same is the case with the micro-rotational parameter as the rotational inertia affects the linear flow potential inversely.

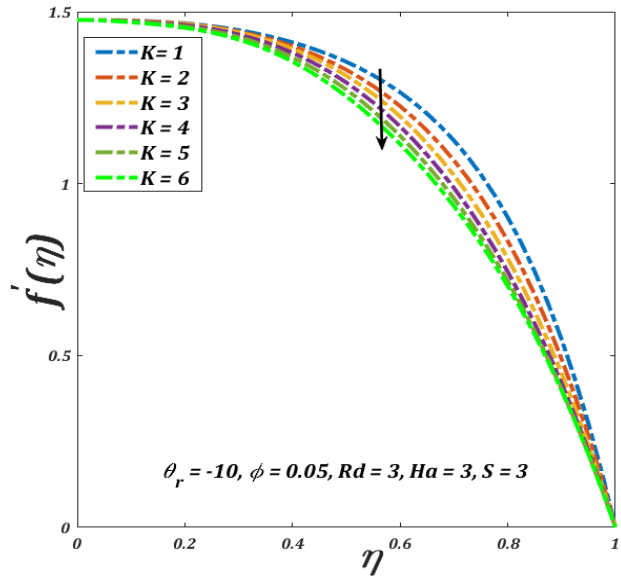


Figure 3.7 Velocity distribution profile with Micropolar parameter

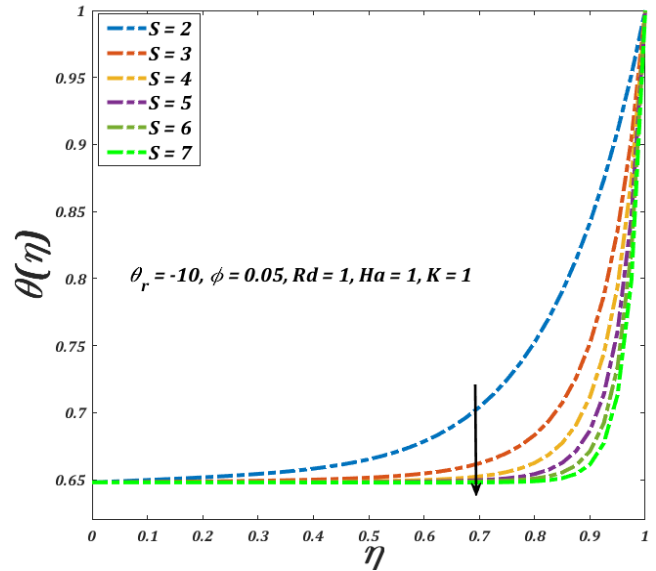


Figure 3.8 Variations in Temperature with Squeezing parameter

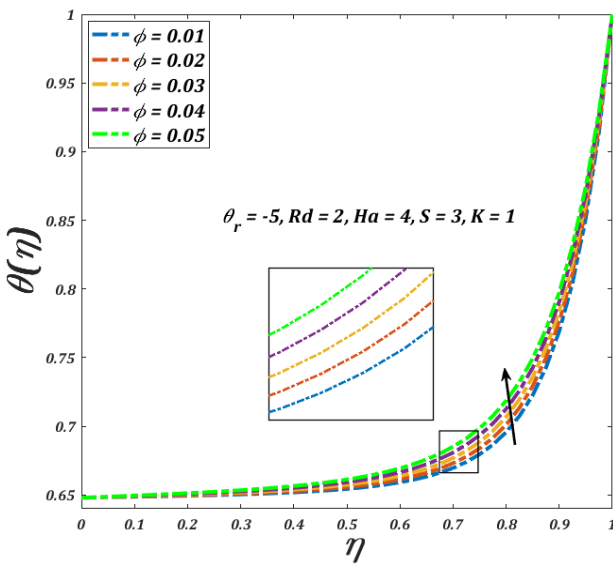


Figure 3.9 Variations in Temperature with Volume fraction parameter

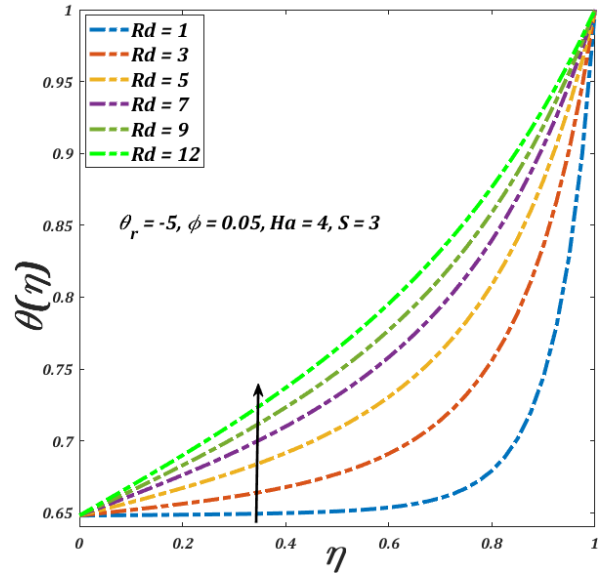


Figure 3.10 Variations in Temperature with Radiation parameter

Fluid temperature is lowest near the origin while it is maximum at the solid boundaries. The temperature distribution of the fluid decreases for squeezing parameters and enhances for rising values of volume fraction and radiation parameter. **Figures (3.8-3.10)** are plots for temperature profile varying with different physical parameters.

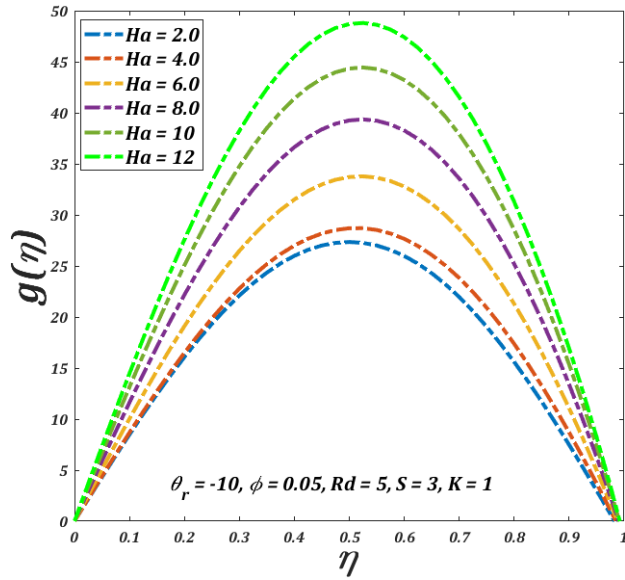


Figure 3.11 Angular velocity variations with Magnetic parameter

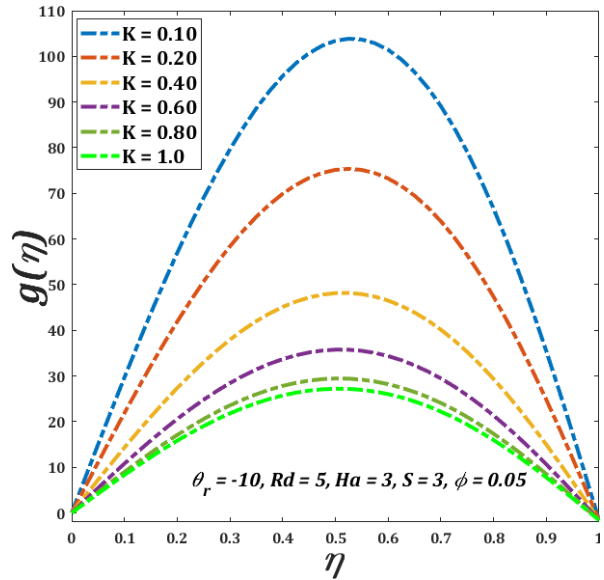


Figure 3.12 Angular velocity variations with Micropolar parameter

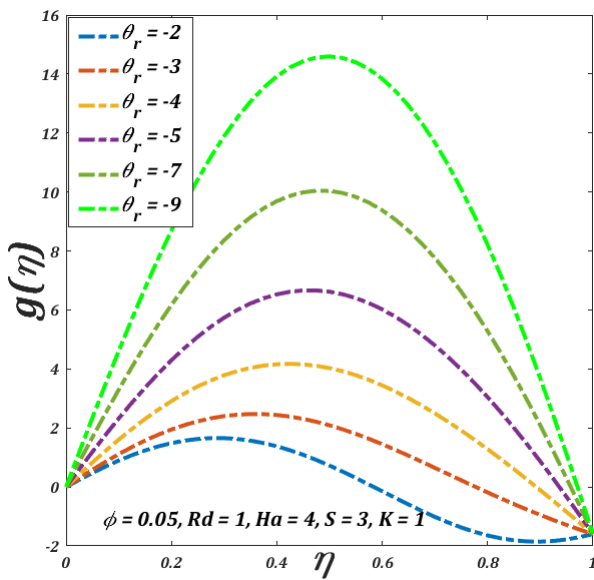


Figure 3.13 Angular velocity variations with variable Viscosity parameter

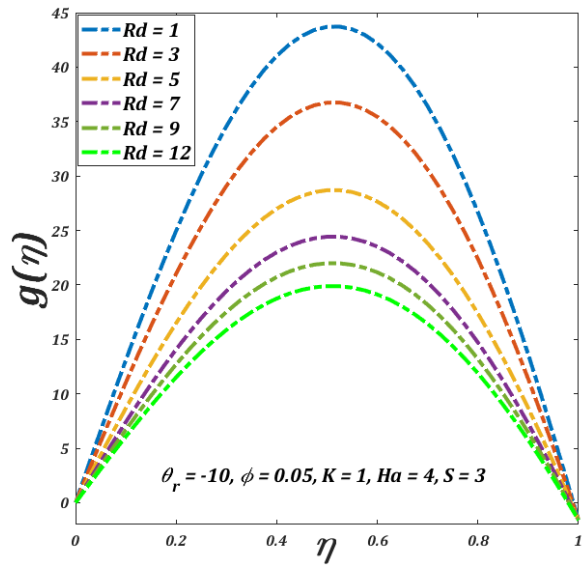


Figure 3.14 Angular velocity variations with Radiation parameter

Figures (3.11-3.15) are the Angular velocity profile of Micro-rotations plotted with respect to different parameters. Angular velocity profile attains its maximum amplitude in the very middle of the region while it reduces towards the solid boundaries. A flow reversal phenomenon can be seen as exhibited due to the rotational inertial very near to the plates. Similar to the case of linear

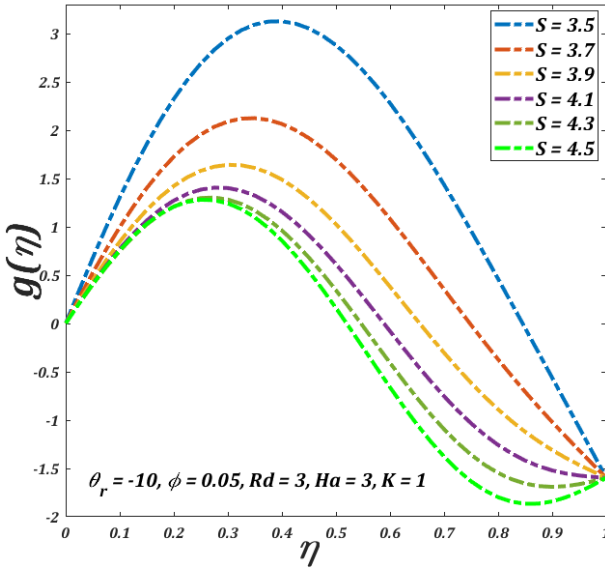


Figure 3.15 Angular velocity variations with Squeezing parameter

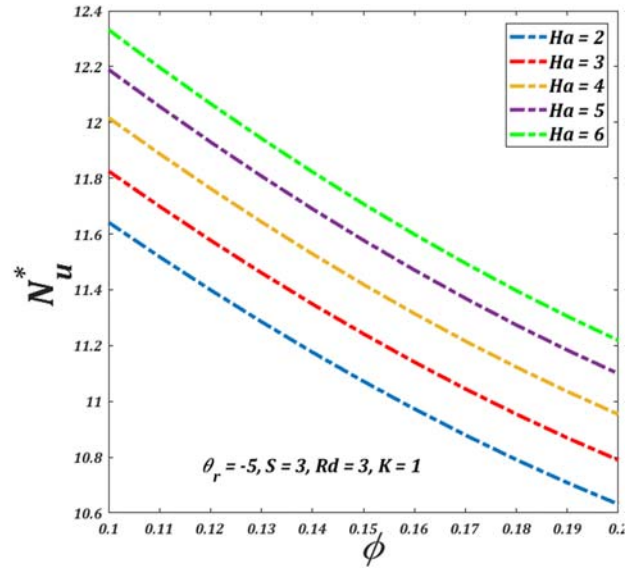


Figure 3.16 Nusselt number profile with Magnetic parameter

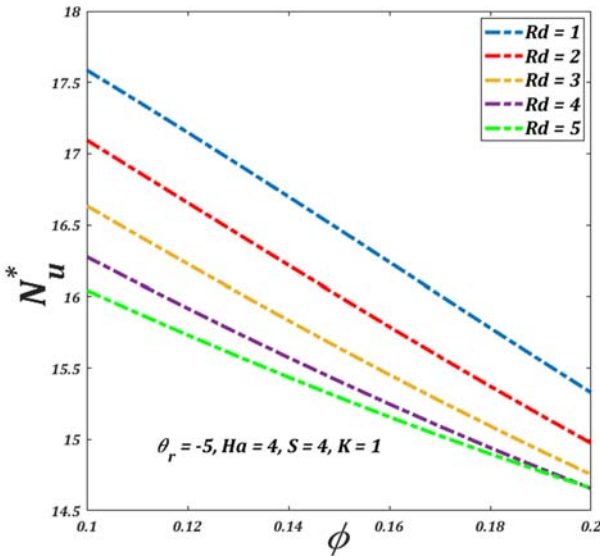


Figure 3.17 Nusselt number profile with Radiation parameter

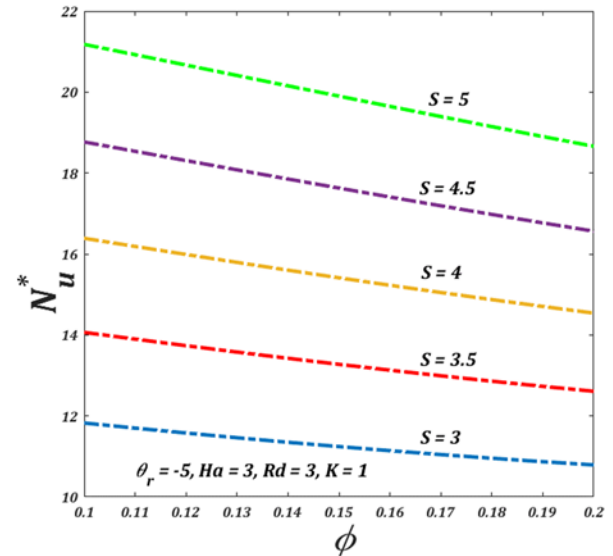


Figure 3.18 Nusselt number profile with Squeezing parameter

velocity profile angular velocity increases with rising values of the magnetic parameter while it decreases with values of micro-rotation and radiation parameter. Strength of viscosity and squeezing on the other hand work differently as it does with linear momentum.

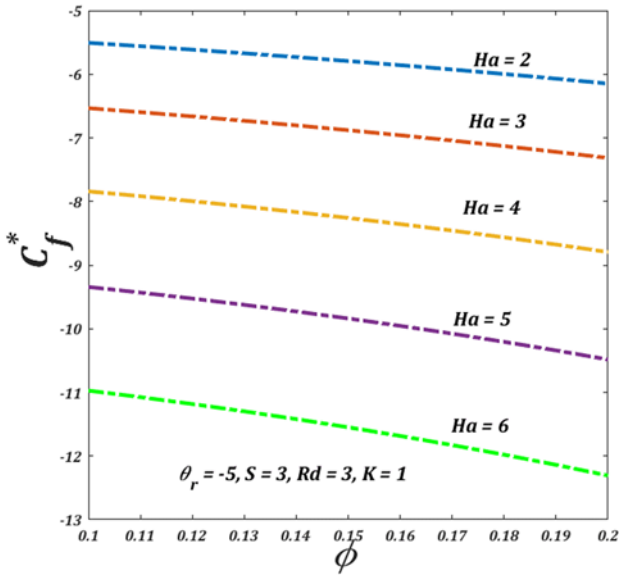


Figure 3.19 Skin friction versus
Magnetic parameter

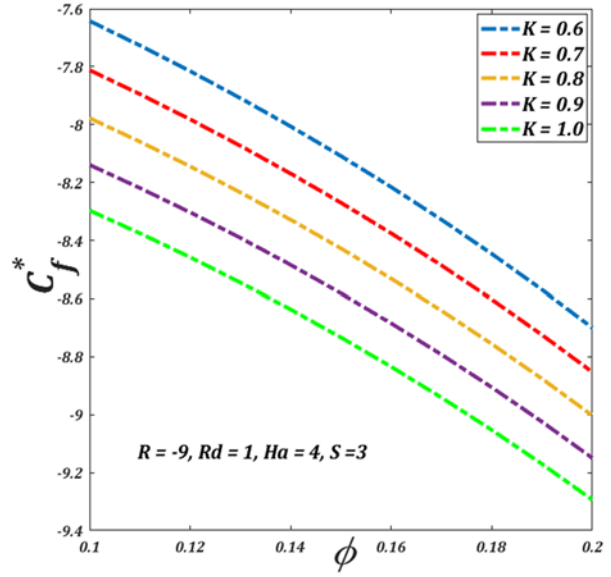


Figure 3.20 Skin friction versus
Micropolar parameter

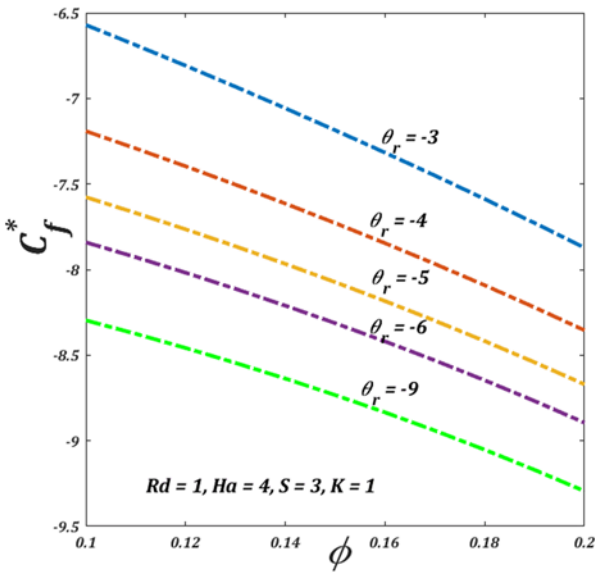


Figure 3.21 Skin friction versus variable
Viscosity parameter

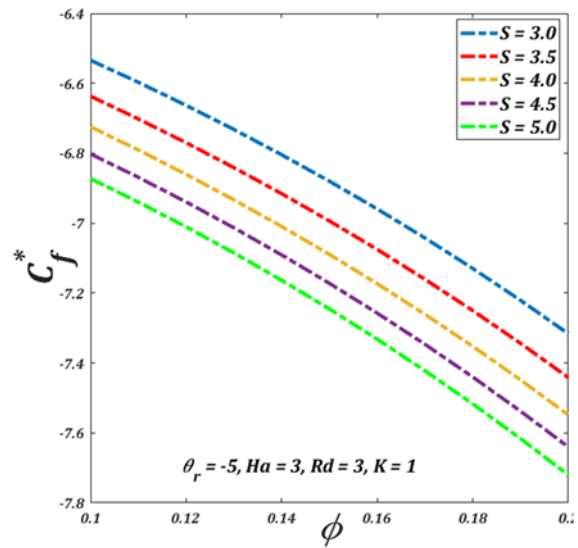


Figure 3.22 Skin friction versus
Magnetic parameter

Angular velocity profile increases with rising values of variable viscosity parameter whereas it decreases with values of squeezing parameter as can be seen in **Figure 3.13** and **Figure 3.15**. **Figures (3.16-3.18)** are graphical results of Nusselt number versus volume fraction with variation in magnetic parameter, radiation parameter and squeezing parameter. It can be seen that

temperature gradient very near to the solid boundary increases for increasing magnitude of magnetic and squeezing parameter whereas it decreases for radiation parameter. **Figures (3.19-3.22)** are graphical results of the Skin friction versus volume fraction parameter. Skin-friction coefficient drops in magnitude for rising values of Hartmann number, curvature parameter, variable viscosity parameter and squeezing parameter.

4 Carbon Nanotubes based nanofluid flow over a stretching Curved surface

4.1 Introduction

The impact of temperature dependent viscosity on the dynamics of pressure-driven nanofluid flow is examined in the present chapter. Consideration is provided for the application of uniform magnetic field along the direction radial to the curvilinear surface. The physical scenario is embedded successfully by the classical continuum model of Navier stoke's. For mathematical simplicity the governing set of equations are cut down in size by knocking out the terms of less significance. The process is known as boundary layer approximation. Appropriate transformations are incorporated on the differential equations that translate the system of partial differential equations into a similar set of ordinary differential equations. These are ordinary differential equations of extremely high non-linearity, which are worked out numerically by the implicit, second order finite difference method. Graphical and numerical results depict the impact of temperature-sensitive viscosity and other physical parameters on the flow of nanofluid. The parameter of viscosity apparently resists the flow velocity and increases nanofluid temperature distribution. The Skin friction near the boundary wall is also raised by the viscosity parameter.

4.2 Mathematical Description

Let us assume a two-dimensional flow of a nanofluid on a curvilinear solid surface with radius R . Nanofluid is asserted as incompressible and exhibiting steady flow. Flow is analyzed in coordinates r and s as set out in **Figure 4.1**. Surface stretched velocity is inferred as U_w along $s - direction$. A steady and invariable magnetic field acting on the fluid along $r - direction$ is taken with strength B_0 .

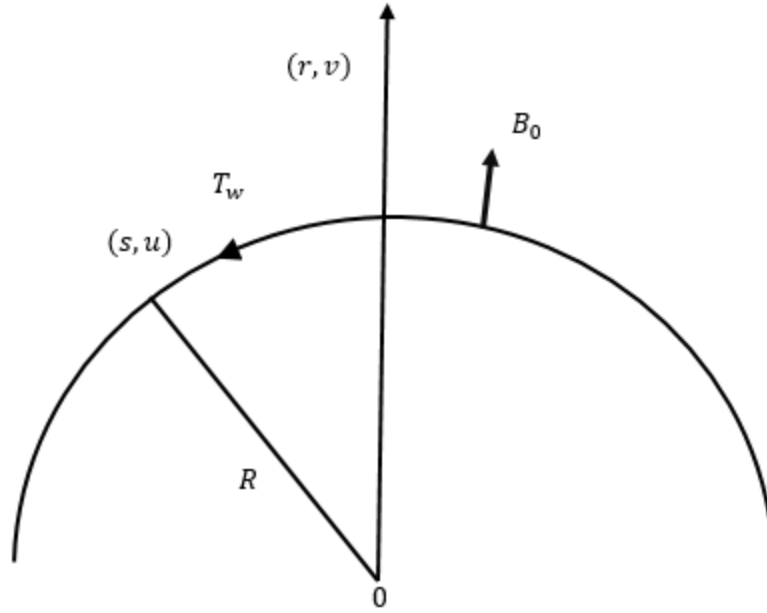


Figure 4.1 Functional diagram

The governing equations in curvilinear coordinates are given as:

$$R \frac{\partial u}{\partial s} + \frac{\partial}{\partial r} [(r + R)v] = 0, \quad (4.1)$$

$$\rho_{nf} \left(v \frac{\partial v}{\partial r} - \frac{u^2}{r+R} + u \left(\frac{R}{r+R} \right) \frac{\partial v}{\partial s} \right) = - \frac{\partial p}{\partial r} + \frac{1}{(r+R)} \frac{\partial}{\partial r} \left((r + R) \mu_{nf} \frac{\partial v}{\partial r} \right) + \quad (4.2)$$

$$\frac{R}{(r+R)} \frac{\partial}{\partial s} \left(\mu_{nf} \left(\frac{\partial u}{\partial r} + \frac{R}{(r+R)} \frac{\partial v}{\partial s} - \frac{u}{r+R} \right) \right) - \frac{1}{r+R} \mu_{nf} \left(\frac{\partial u}{\partial r} + \frac{R}{(r+R)} \frac{\partial v}{\partial s} - \frac{u}{r+R} \right),$$

$$\rho_{nf} \left(v \frac{\partial u}{\partial r} + u \left(\frac{R}{r+R} \right) \frac{\partial u}{\partial s} + \frac{uv}{r+R} \right) = - \frac{R}{(r+R)} \frac{\partial p}{\partial s} + \frac{1}{(r+R)} \frac{\partial}{\partial r} \left((r + R) \mu_{nf} \left(\frac{\partial u}{\partial r} + \frac{R}{(r+R)} \frac{\partial v}{\partial s} - \right. \right. \quad (4.3)$$

$$\left. \left. \frac{u}{r+R} \right) \right) + \frac{R}{(r+R)} \frac{\partial}{\partial s} \left(\mu_{nf} \left(\frac{R}{(r+R)} \frac{\partial u}{\partial s} + \frac{v}{r+R} \right) \right) - \sigma B^2 u,$$

$$v \frac{\partial T}{\partial r} + \frac{R}{(r+R)} \frac{\partial T}{\partial s} = \alpha_{nf} \left(\frac{\partial^2 T}{\partial r^2} + \frac{1}{(r+R)} \frac{\partial T}{\partial r} \right) \quad (4.4)$$

u represent the velocity along s while v shows the velocity of the fluid in $r - direction$. T is fluid temperature. The pressure distribution is depicted with the symbol p , which is not ignorable in the case of the curved surface. The effective density, viscosity and thermal conductivity for chosen materials are computed as it is taken in previous chapters.

We now intend to write the above equations into non-dimensional form by introducing some variables. i.e.: $s^* = \frac{s}{L}$, $R^* = \frac{R}{\delta}$, $r^* = \frac{r}{\delta}$, $P^* = \frac{p}{\rho_{nf} U_\infty^2}$, where L depicts the horizontal length scale, δ is the boundary layer stiffness at $x = L$, we obtained an estimate of it by taking $(\frac{\delta}{L}) = O(Re^{-1/2})$, where $Re = \frac{U_\infty L}{\nu_\infty}$, U_∞ is the uniform fluid velocity aligned in s-direction.

The incorporated boundary layer approximation reduces the governing nonlinear partial differential equations to the form given below for very large values of Reynold number.

$$\rho_{nf} \left(\frac{u^2}{r+R} \right) = \frac{\partial p}{\partial r} \quad (4.5)$$

$$\rho_{nf} \left(v \frac{\partial u}{\partial r} + u \left(\frac{R}{r+R} \right) \frac{\partial u}{\partial s} + \frac{uv}{r+R} \right) = -\rho_{nf} \frac{R}{(r+R)} \frac{\partial p}{\partial s} + \mu_{nf} \left(\frac{\partial^2 u}{\partial r^2} + \frac{1}{(r+R)} \frac{\partial u}{\partial r} - \frac{u}{(r+R)^2} \right) + \frac{\partial \mu_{nf}}{\partial r} \left(\frac{\partial u}{\partial r} - \frac{u}{(r+R)} \right) - \sigma B_0^2 u, \quad (4.6)$$

$$v \frac{\partial T}{\partial r} + \frac{R}{(r+R)} \frac{\partial T}{\partial s} = \alpha_{nf} \left(\frac{\partial^2 T}{\partial r^2} + \frac{1}{(r+R)} \frac{\partial T}{\partial r} \right) \quad (4.7)$$

The relevant boundary conditions:

$$\left. \begin{array}{l} u = \lambda as, \quad v = 0, \quad T = T_w \quad \text{at} \quad r = 0, \\ u \rightarrow 0, \quad \frac{\partial u}{\partial r} \rightarrow 0 \quad T = T_\infty \quad \text{at} \quad r \rightarrow \infty. \end{array} \right\} \quad (4.8)$$

Choosing suitable similarity transformations and introducing dimensionless functions f , θ , and similarity variable η

$$u = asf'(\eta), v = -\frac{R}{r+R} \sqrt{av_\infty} f(\eta), \theta = \frac{T - T_\infty}{T_w - T_\infty}, \eta = \sqrt{\frac{a}{\nu_\infty}} r, p = \rho_{nf} a^2 s^2 P(\eta) \quad (4.9)$$

The associated momentum and the energy equations given in *Eqs*(4.5 – 4.7) are transformed to the following partial differential equation given below by applying suitable similarity transformations above:

$$\frac{\partial P}{\partial \eta} = \frac{f'^2}{\eta + \kappa} \quad (4.10)$$

$$\frac{2\kappa}{(\eta+\kappa)}P(\eta) = \frac{1}{A_1} \left(\frac{f'''}{(1-\frac{\theta}{\theta_r})} - \frac{1}{(\eta+\kappa)} \frac{f'\theta'}{\theta_r(1-\frac{\theta}{\theta_r})^2} + \frac{f'\theta'}{\theta_r(1-\frac{\theta}{\theta_r})^2} + \frac{1}{(\eta+\kappa)} \frac{f'}{\theta_r(1-\frac{\theta}{\theta_r})} - \right. \quad (4.11)$$

$$\left. \frac{1}{(\eta+\kappa)^2} \frac{f'}{(1-\frac{\theta}{\theta_r})} - M_1 f' \right) + \frac{\kappa}{(\eta+\kappa)} (ff'' - f'^2 + \frac{1}{(\eta+\kappa)} ff')$$

$$\theta'' + \frac{1}{(\eta+\kappa)} \theta' + Pr \frac{\epsilon_2}{\epsilon_1} \frac{\kappa}{(\eta+\kappa)} f\theta' = 0 \quad (4.12)$$

Using (4.10) into (4.11) we get

$$\begin{aligned} & \frac{1}{A_1} \left(\frac{(\eta+\kappa)f^{iv}}{(1-\frac{\theta}{\theta_r})} + \frac{2f'''}{(1-\frac{\theta}{\theta_r})} + \frac{2(\eta+\kappa)f'''\theta'}{\theta_r(1-\frac{\theta}{\theta_r})^2} + \frac{f''\theta'}{\theta_r(1-\frac{\theta}{\theta_r})^2} - \frac{f'\theta'}{\theta_r(1-\frac{\theta}{\theta_r})^2} - \frac{2f'\theta'}{\theta_r^2(1-\frac{\theta}{\theta_r})^3} + \right. \\ & \frac{(\eta+\kappa)f''\theta'}{\theta_r(1-\frac{\theta}{\theta_r})^2} + \frac{2(\eta+\kappa)f''\theta'}{\theta_r^2(1-\frac{\theta}{\theta_r})^3} - \frac{1}{(\eta+\kappa)} \frac{f''}{(1-\frac{\theta}{\theta_r})} + \frac{1}{(\eta+\kappa)^2} \frac{f'}{(1-\frac{\theta}{\theta_r})} - \frac{1}{(\eta+\kappa)} \frac{f'\theta'}{\theta_r(1-\frac{\theta}{\theta_r})^2} - M_1 (f' + \\ & \left. (\eta + \kappa)f'' \right) - \kappa (f'f'' - ff''') + \frac{\kappa}{(\eta+\kappa)} \left(ff'' - \frac{1}{(\eta+\kappa)} ff' - f'^2 \right) = 0 \end{aligned} \quad (4.13)$$

$$\theta'' + \frac{1}{(\eta+\kappa)} \theta' + Pr \frac{\epsilon_2}{\epsilon_1} \frac{\kappa}{(\eta+\kappa)} f\theta' = 0 \quad (4.14)$$

The transformed boundary conditions are given as:

$$f = 0, f' = \lambda, \theta = 1 \text{ at } \eta = 0$$

$$f' \rightarrow 0, f'' \rightarrow 0, \theta \rightarrow 0 \text{ as } \eta \rightarrow \infty$$

We are also interested in finding the skin friction coefficient C_f near the boundaries which can be written as $C_f = \frac{\tau_w}{\rho f_\infty U_w^2}$, where $\tau_w = \mu_{nf} \left(\frac{\partial u}{\partial r} + \frac{u}{r+R} \right) |_{r=0}$, Using the above relations we have

$$C_f Re_s^{1/2} = \frac{1}{(1-\phi)^{2.5} \left(1 - \frac{1}{\theta_r} \right)} \left(f''(0) + \frac{1}{K} \right), \text{ where } Re_s = \frac{as^2}{\nu f_\infty} \text{ is the local Reynolds number.}$$

4.3 Solution Technique

Navier-Stokes' classical model is embedded in the considered physical situation. The terms with relatively no impact are then drop out using boundary layer approximation. The governing

equations are highly non-linear coupled partial differential equations. These mathematical assertions are written in dimensionless form at first stage and then converted into a set of ordinary differential equations by inducing a few new variables into the system. We now are interested to solve these similar equations with an implicit finite difference numerical technique. The obtained regular, nonlinear differential equations are transformed into a series of ordinary differential equations of the first order. The system then is discretized with a central difference scheme followed by linearization by Newton's linearization method. This linearized system is then set into a tridiagonal matrix form. Matrix algebra following the Block elimination technique is programmed in MATLAB to execute the very last step. The method we have incorporated on our problem is well known as the Keller box scheme. The present problem is also evident in scheme effectivity on complex situations since governing equations are highly non-linear and can merely be solved with conventional techniques. Keller box executed the solution with very much freedom of choosing the desired values of involved parameters. A comparison study with previous literature is also presented to validate the solution obtained from the above mathematical technique. **Table 4.1** shows numeric obtained by the present scheme as well as by previous work of Rosca et al.[41]. Both of these results are in very good agreement with each other.

4.4 Results and Discussion

Graphical and Numerical results are determined in the presence of different physical parameters. The main theme of our work is to find the behavior in the presence of temperature-dependent viscosity.

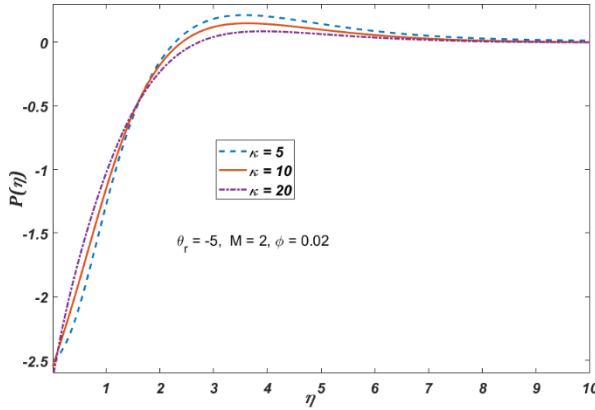


Figure 4.2 Pressure distribution versus Curvature parameter

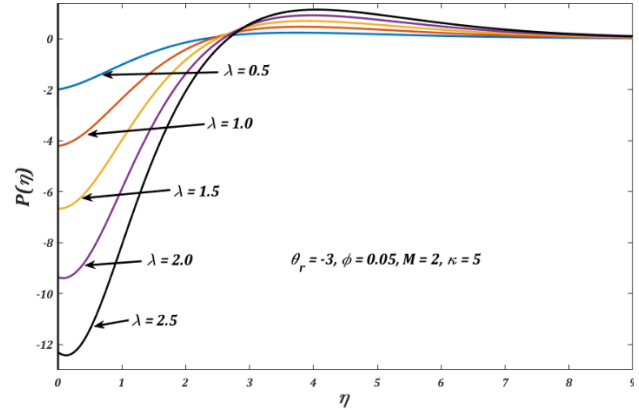


Figure 4.3 Pressure distribution versus Stretching parameter

Equation (4.11) can be solved to find dimensionless pressure readings. **Figure 4.2** and **Figure 4.3** shows plots of pressure variation with curvature and stretching parameter. A decrease in momenta is evident from the graphical results as the magnitude of the variable viscosity parameter is raised, while the magnetic parameter absorbs the opposite behavior as shown in **Figure 4.4** and **Figure 4.6**. Velocity variation with volume fraction of the curvature and carbon nanotubes can be seen respectively in **Figure 4.7** and **Figure 4.5**. From the results it is shown that the velocity profile decreases with an increase in curvature parameter, while an increase in velocity along s-direction is observed with the increase in volume fraction of carbon nanotubes.

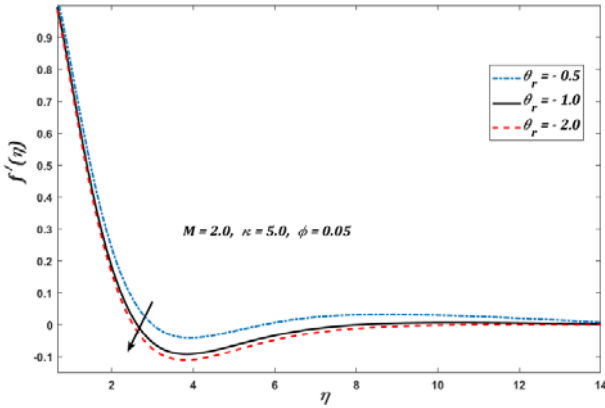


Figure 4.4 Velocity variations with variable Viscosity parameter

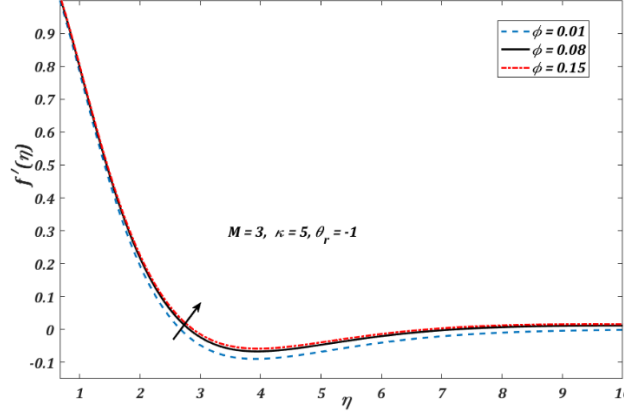


Figure 4.5 Velocity variations with Volume fraction parameter

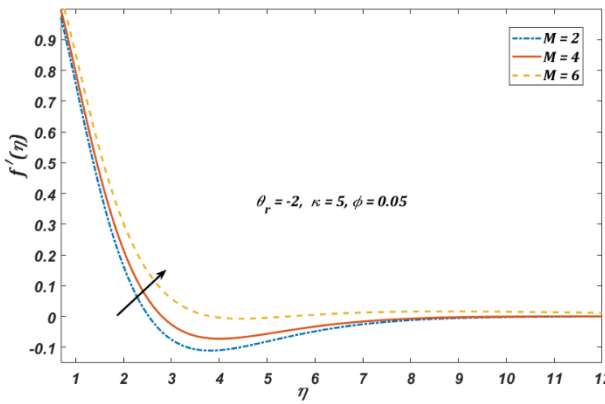


Figure 4.6 Velocity variations with Magnetic parameter

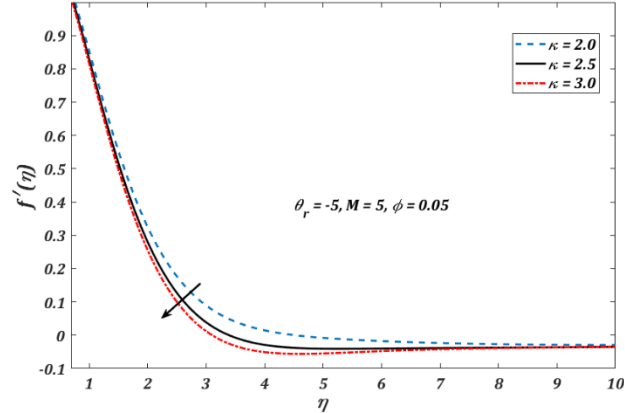


Figure 4.7 Velocity variations with Curvature parameter

Figures (4.8-4.11) show a variation in Temperature with various parameters including viscosity parameter, curvature, volume fraction and magnetic parameter.

In Figure 4.8 it is shown that the fluid temperature rises for ascending values viscosity parameter. As the abundance of solid particles increases the thermal conductivity of the nanofluid also rises, it can be validated from Figure 4.9 that a rise in the volume fraction of carbon nanotubes increase the distribution of temperature in the fluid. Similarly, with the raising values of both magnetic and curvature parameters, the temperature distribution within the fluid increases as can be seen in Figure 4.10 and Figure 4.11,

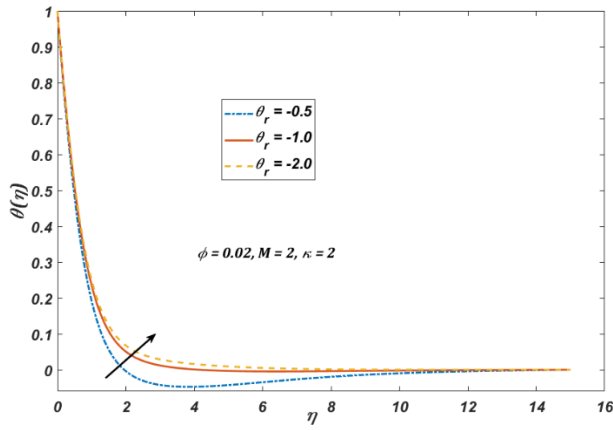


Figure 4.8 Temperature variations with variable Viscosity parameter

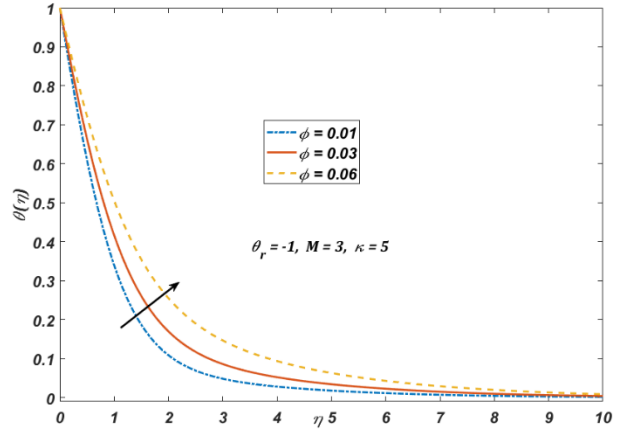


Figure 4.9 Temperature variations with Volume fraction parameter

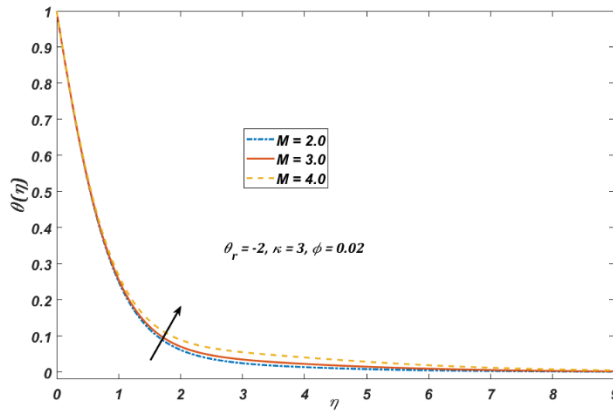


Figure 4.10 Temperature variations with Magnetic parameter

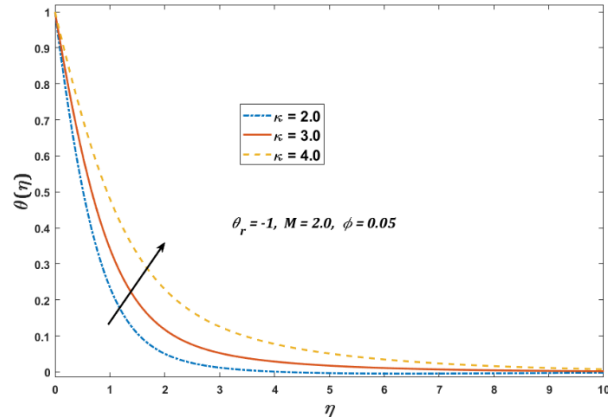


Figure 4.11 Temperature variations with Curvature parameter

Figure 4.12 and **Figure 4.13** shows the variation of velocity gradient with curvature and stretching parameter.

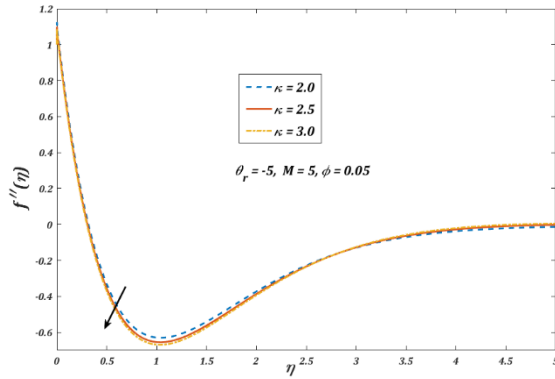


Figure 4.12 Velocity gradient with Curvature parameter

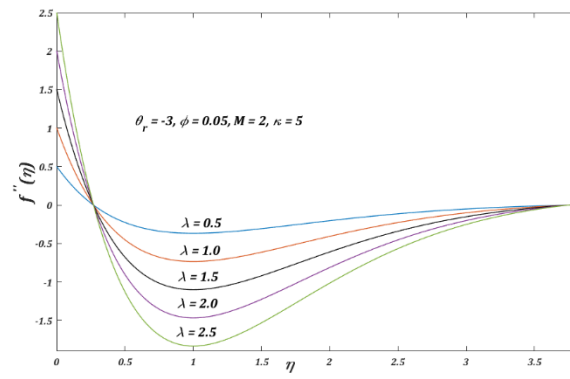


Figure 4.13 Velocity gradient with Stretching parameter

Table 4.2 gives numeric for values of dimensionless shear stress near the wall. Readings indicate that skin friction increases both for the growing degree of curvature parameter and with the .increased weight of the viscosity parameter

Table 4.1 Comparison Table for $-C_f Re_s^{1/2}$ with different values of the curvature parameter.

$$\lambda = 1, M = 0, \phi = 0.0, \theta_r \rightarrow \infty$$

| κ | Roşca et al.[41] | Present results |
|----------|------------------|-----------------|
| 5 | 1.15076 | 1.20000 |
| 10 | 1.07172 | 1.10000 |
| 20 | 1.03501 | 1.05001 |
| 30 | 1.02315 | 1.03331 |
| 40 | 1.01729 | 1.02503 |
| 50 | 1.01380 | 1.02001 |
| 100 | 1.00687 | 1.01002 |
| 200 | 1.00342 | 1.00504 |

| | | |
|----------|---------|---------|
| 1000 | 1.00068 | 1.00100 |
| ∞ | 1.00000 | 1.00000 |

Table 4.2 Numerical values of $-C_f Re_s^{-1/2}$ with different values of curvature and variable viscosity parameters.
 $\lambda = 1, M = 2, \phi = 0$

| κ | $\theta_r = -3$ | $\theta_r = -5$ | $\theta_r = -10$ | $\theta_r = -15$ |
|----------|-----------------|-----------------|------------------|------------------|
| 5 | 1.02312 | 1.13681 | 1.24017 | 1.27892 |
| 10 | 0.93787 | 1.04208 | 1.13682 | 1.17234 |
| 20 | 0.89524 | 0.99472 | 1.08514 | 1.11906 |
| 50 | 0.86966 | 0.96630 | 1.05414 | 1.08708 |
| 100 | 0.86114 | 0.95682 | 1.04381 | 1.07642 |
| 500 | 0.85432 | 0.94924 | 1.03554 | 1.06789 |
| 1000 | 0.85347 | 0.94830 | 1.03450 | 1.06683 |

5 Unsteady flow of a CNT based nanofluid over a porous shrinking curved surface

5.1 Introduction

This chapter represents the study of a carbon nanotubes based nanofluid flowing over a curved shrinking surface. The surface is considered to be permeable. An unsteady magnetic field acting along the radial direction is also considered. Navier-Stokes model for viscous fluids is used to embed the physical situation. Curvilinear coordinates r and s are introduced to model the problem. The dependence of viscosity on temperature makes the proposed model highly non-linear and coupled with the energy equation. Consequently, the resulting non-linear partial differential equations are first reformed by proper transformations into a set of ordinary differential equations, and then numerically addressed by the Keller box method. This study reveals the existence of dual solutions. Graphical, as well as numerical results, are obtained for both the solutions. It has been observed that there exists a point called a critical point for certain parameters about which either a single or dual solution exists. On this very specific point, however, no solution exists. Graphical results are obtained to study the variation of these critical points with respect to different involved parameters.

5.2 Mathematical description

The radius R of the curved shrink surface depends on $R(t) = R_0\sqrt{1 - \alpha t}$, where R_0 is a positive constant, as shown in Figure 1. For accelerated sheet $\alpha > 0$ whereas for decelerated sheet $\alpha < 0$. The sheet is shrinking with the velocity $U_w(s, t)$ in s -direction at $t = 0$. The fluid is electrically conducting. An unsteady external magnetic field $B(t) = B_0(1 - \alpha t)^{1/2}$ is applied along r - *direction* while the induced magnetic field is negligible. The surface is assumed to be permeable with mass flux velocity $V_w(r, t)$ which corresponds to the suction/injection of the fluid.

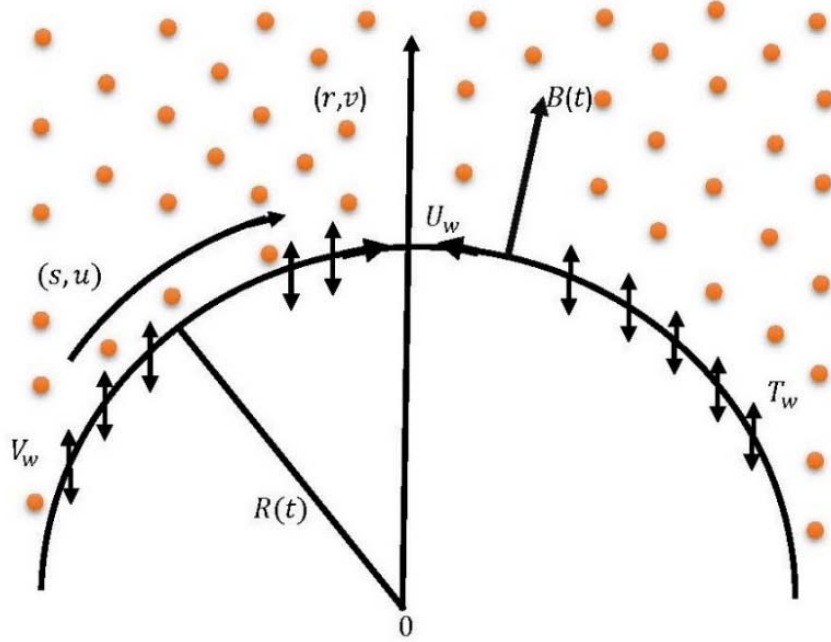


Figure 5.1 Flow diagram

The governing equations can be articulated as:

$$\frac{\partial}{\partial r} [v(r + R)] + R \frac{\partial u}{\partial s} = 0, \quad (5.1)$$

$$\rho_{nf} \left(\frac{\partial v}{\partial t} - \frac{u^2}{r+R} + v \frac{\partial v}{\partial r} + u \frac{\partial v}{\partial s} \left(\frac{R}{r+R} \right) \right) = -\frac{\partial p}{\partial r} + \frac{1}{(r+R)} \frac{\partial}{\partial r} \left(\mu_{nf} (r + R) \frac{\partial v}{\partial r} \right) + \quad (5.2)$$

$$\frac{R}{(r+R)} \frac{\partial}{\partial s} \left(\mu_{nf} \left(\frac{\partial u}{\partial r} - \frac{u}{r+R} + \frac{R}{(r+R)} \frac{\partial v}{\partial s} \right) \right) - \frac{1}{r+R} \mu_{nf} \left(\frac{\partial u}{\partial r} - \frac{u}{r+R} + \frac{R}{(r+R)} \frac{\partial v}{\partial s} \right),$$

$$\rho_{nf} \left(\frac{\partial u}{\partial t} + \frac{uv}{r+R} + v \frac{\partial u}{\partial r} + u \left(\frac{R}{r+R} \right) \frac{\partial u}{\partial s} \right) = -\frac{R}{(r+R)} \frac{\partial p}{\partial s} + \frac{1}{(r+R)} \frac{\partial}{\partial r} \left((r + R) \mu_{nf} \left(\frac{\partial u}{\partial r} - \frac{u}{r+R} + \right. \right. \quad (5.3)$$

$$\left. \left. \frac{R}{(r+R)} \frac{\partial v}{\partial s} \right) \right) + \frac{R}{(r+R)} \frac{\partial}{\partial s} \left(\mu_{nf} \left(\frac{v}{r+R} + \frac{R}{(r+R)} \frac{\partial u}{\partial s} \right) \right) - \sigma B^2 u,$$

$$\frac{\partial T}{\partial t} + v \frac{\partial T}{\partial r} + \frac{R}{(r+R)} \frac{\partial T}{\partial s} = \alpha_{nf} \left(\frac{\partial^2 T}{\partial r^2} + \frac{1}{(r+R)} \frac{\partial T}{\partial r} \right). \quad (5.4)$$

$$\left. \begin{aligned} u &= \lambda \frac{U_w}{(1-\alpha t)}, & v &= V_w(s, t), & T &= T_w, & \text{at } r &= 0, \\ u &= 0, & \frac{\partial u}{\partial r} &= 0, & T &= T_\infty, & \text{at } r &\rightarrow \infty. \end{aligned} \right\} \quad (5.5)$$

$\lambda > 0$, represent stretching and $\lambda < 0$ is the shrinking parameter. The stretching/shrinking velocity is given as: $U_w = as$, in which a is positive constant. Also, $V_w = -\sqrt{\frac{av_\infty}{(1-\alpha t)}}S$, represents mass transfer through the surface, for the suction $S > 0$ and for the injection $S < 0$.

For large Reynolds number, Eqs. (1) to (5), are reduced to the following

$$\rho_{nf} \left(\frac{u^2}{r+R} \right) = \frac{\partial p}{\partial r}, \quad (5.6)$$

$$\rho_{nf} \left(\frac{\partial u}{\partial t} + \frac{uv}{r+R} + v \frac{\partial u}{\partial r} + u \left(\frac{R}{r+R} \right) \frac{\partial u}{\partial s} \right) = -\rho_{nf} \frac{R}{(r+R)} \frac{\partial p}{\partial s} + \mu_{nf} \left(\frac{\partial^2 u}{\partial r^2} + \frac{1}{(r+R)} \frac{\partial u}{\partial r} - \frac{u}{(r+R)^2} \right) + \frac{\partial \mu_{nf}}{\partial r} \left(\frac{\partial u}{\partial r} - \frac{u}{(r+R)} \right) - \sigma B^2 u, \quad (5.7)$$

$$\frac{\partial T}{\partial t} + v \frac{\partial T}{\partial r} + \frac{R}{(r+R)} \frac{\partial T}{\partial s} = \alpha_{nf} \left(\frac{\partial^2 T}{\partial r^2} + \frac{1}{(r+R)} \frac{\partial T}{\partial r} \right), \quad (5.8)$$

$$\left. \begin{aligned} u &= \lambda \frac{as}{(1-\alpha t)}, & v &= -\sqrt{\frac{av_\infty}{(1-\alpha t)}}S, & T &= T_w & \text{at } r &= 0, \\ u &= 0, & \frac{\partial u}{\partial r} &= 0, & T &= T_\infty & \text{at } r &\rightarrow \infty. \end{aligned} \right\} \quad (5.9)$$

By using the following transformation

$$\left. \begin{aligned} u &= \frac{as}{(1-\alpha t)} f'(\eta), & v &= -\frac{R}{r+R} \sqrt{\frac{av_\infty}{(1-\alpha t)}} f(\eta), & \theta &= \frac{T - T_\infty}{T_w - T_\infty} \\ \eta &= \sqrt{\frac{a}{v_\infty(1-\alpha t)}} r, & p &= \frac{\rho_{nf} a^2 s^2}{(1-\alpha t)^2} P(\eta) \end{aligned} \right\} \quad (5.10)$$

Equations (5.6 – 5.8) are transformed into

$$\frac{\partial P}{\partial \eta} = \frac{f'^2}{\eta + \kappa}, \quad (5.11)$$

$$\begin{aligned} \frac{2\kappa}{(\eta + \kappa)} P(\eta) = & \frac{1}{A_1} \left(\frac{f'''}{(1-\frac{\theta}{\theta_r})} - \frac{1}{(\eta + \kappa)} \frac{f'\theta'}{\theta_r(1-\frac{\theta}{\theta_r})^2} + \frac{f''\theta'}{\theta_r(1-\frac{\theta}{\theta_r})^2} + \frac{1}{(\eta + \kappa)} \frac{f''}{(1-\frac{\theta}{\theta_r})} - \frac{1}{(\eta + \kappa)^2} \frac{f'}{(1-\frac{\theta}{\theta_r})} - \right. \\ & \left. M_1 f' \right) - \beta \left(\frac{1}{2} \eta f'' + f' \right) + \frac{\kappa}{(\eta + \kappa)} (f f'' - f'^2 + \frac{1}{(\eta + \kappa)} f f'), \end{aligned} \quad (5.12)$$

From Eqs. (5.11) and (5.12), it follows that

$$\begin{aligned} \frac{1}{A_1} \left(\frac{(\eta + \kappa) f^{iv}}{(1-\frac{\theta}{\theta_r})} + \frac{2f'''}{(1-\frac{\theta}{\theta_r})} + \frac{2(\eta + \kappa) f'''\theta'}{\theta_r(1-\frac{\theta}{\theta_r})^2} + \frac{f''\theta'}{\theta_r(1-\frac{\theta}{\theta_r})^2} - \frac{f'\theta''}{\theta_r(1-\frac{\theta}{\theta_r})^2} - \frac{2f'\theta'}{\theta_r^2(1-\frac{\theta}{\theta_r})^3} + \frac{(\eta + \kappa) f''\theta''}{\theta_r(1-\frac{\theta}{\theta_r})^2} + \right. \\ \left. \frac{2(\eta + \kappa) f''\theta'}{\theta_r^2(1-\frac{\theta}{\theta_r})^3} - \frac{f''}{(1-\frac{\theta}{\theta_r})(\eta + \kappa)} + \frac{f'}{(1-\frac{\theta}{\theta_r})(\eta + \kappa)^2} - \frac{f'\theta'}{(\eta + \kappa)\theta_r(1-\frac{\theta}{\theta_r})^2} - M_1 (f' + (\eta + \kappa) f'') \right) - \\ \beta \left(\frac{3}{2} (\eta + \kappa) f'' + \frac{1}{2} \eta f'' + \frac{1}{2} \eta (\eta + \kappa) f''' + f' \right) - \kappa (f' f'' - f f''') + \frac{\kappa}{(\eta + \kappa)} (f f'' - \frac{1}{(\eta + \kappa)} f f' - f'^2) = 0, \end{aligned} \quad (5.13)$$

$$\theta'' + \frac{1}{(\eta + \kappa)} \theta' + Pr \left(\frac{\epsilon_2}{\epsilon_1} \right) \frac{\kappa}{(\eta + \kappa)} f \theta' - Pr \left(\frac{\epsilon_2}{\epsilon_1} \right) \frac{\beta}{2} \eta \theta' = 0, \quad 5.14$$

$$\left. \begin{aligned} f = S, \quad f' = \lambda, \quad \theta = 1 \quad \text{at } \eta = 0, \\ f' \rightarrow 0, \quad f'' \rightarrow 0, \quad \theta \rightarrow 0 \quad \text{as } \eta \rightarrow \infty. \end{aligned} \right\} \quad 5.15$$

Where $M_1 = (1 - \phi)^{2.5} M^2$. The coefficient of Skin friction is defined as $C_f = \frac{\tau_w}{\rho_{f\infty} U_w^2}$, in which

$\tau_w = \mu_{nf} \left(\frac{\partial u}{\partial r} - \frac{u}{r+R} \right) |_{r=0}$, that consequently lead to $C_f Re_s^{1/2} = \frac{1}{(1-\phi)^{2.5} (1-\frac{1}{\theta_r})} (f''(0) - \frac{1}{\kappa})$. The

local Reynolds number is given by $Re_s = \frac{as^2}{\nu_{f\infty}}$. The properties of involved physical parameters

have been presented in **Table 2.1**.

5.3 Solution procedure

In the innovative Keller Box method, four new dependent variables namely u, v, w and m are familiarized to reduce the Eqs. (5.13) and (5.14) along with allied conditions given in Eq. (5.15) beneath as:

$$f' = u, \quad (5.16)$$

$$u' = v, \quad (5.17)$$

$$v' = w, \quad (5.18)$$

$$\theta' = m, \quad (5.19)$$

$$\frac{1}{A_1} \left(\frac{(\eta+\kappa)w'}{(1-\frac{\theta}{\theta_r})} + \frac{2w}{(1-\frac{\theta}{\theta_r})} + \frac{2(\eta+\kappa)wm}{\theta_r(1-\frac{\theta}{\theta_r})^2} + \frac{vm}{\theta_r(1-\frac{\theta}{\theta_r})^2} - \frac{um'}{\theta_r(1-\frac{\theta}{\theta_r})^2} - \frac{2um}{\theta_r^2(1-\frac{\theta}{\theta_r})^3} + \frac{(\eta+\kappa)vm'}{\theta_r(1-\frac{\theta}{\theta_r})^2} + \right. \\ \left. \frac{2(\eta+\kappa)vm}{\theta_r^2(1-\frac{\theta}{\theta_r})^3} - \frac{v}{(1-\frac{\theta}{\theta_r})(\eta+\kappa)} + \frac{u}{(1-\frac{\theta}{\theta_r})(\eta+\kappa)^2} - \frac{um}{(\eta+\kappa)\theta_r(1-\frac{\theta}{\theta_r})^2} - M_1(u + (\eta + \kappa)v) \right) - \quad (5.20)$$

$$\beta \left(\frac{3}{2}(\eta + \kappa)v + \frac{1}{2}\eta v + \frac{1}{2}\eta(\eta + \kappa)w + u \right) + \kappa(fw - uv) + \frac{\kappa}{(\eta+\kappa)}(fv - u^2 - \frac{1}{(\eta+\kappa)}fu) = 0,$$

$$m' + \frac{1}{(\eta+\kappa)}m + Pr \frac{\epsilon_2}{\epsilon_1} \frac{\kappa}{(\eta+\kappa)} fm - Pr \frac{\epsilon_2}{\epsilon_1} \frac{\beta}{2} \eta m = 0, \quad (5.21)$$

$$\left. \begin{aligned} f &= S, & u &= \lambda, & \theta &= 1 & \text{at } \eta &= 0, \\ u &\rightarrow 0, & v &\rightarrow 0, & \theta &\rightarrow 0 & \text{as } \eta &\rightarrow \infty. \end{aligned} \right\} \quad (5.22)$$

The schematic structure of mesh points in a rectangular plan is already shown in **Figure 2.2**. The coordinate's position is indicated by the numbers i and j . The finite-difference form of any point will be $(\)_{j-1/2}^i = \frac{1}{2}[(\)_{j-1}^i + (\)_j^i]$ and $(\)_j^{i-1/2} = \frac{1}{2}[(\)_j^{i-1} + (\)_j^i]$. Consequently, the first four equations are discretized by placing at $(x^i, \eta_{j-1/2})$ where the last two equations are discretized by fixing at $(x^{i-1/2}, \eta_{j-1/2})$.

$$f_j^i = f_{j-1}^i + \frac{h_j}{2}(u_{j-1}^i + u_j^i), \quad (5.23)$$

$$u_j^i = u_{j-1}^i + \frac{h_j}{2}(v_{j-1}^i + v_j^i), \quad (5.24)$$

$$v_j^i = v_{j-1}^i + \frac{h_j}{2}(w_{j-1}^i + w_j^i), \quad (5.25)$$

$$\theta_j^i = \theta_{j-1}^i + \frac{h_j}{2}(m_{j-1}^i + m_j^i). \quad (5.26)$$

The heat equation now can be written as

$$\left[\frac{(m_j - m_{j-1})}{h_j} + \frac{(m_j + m_{j-1})}{2(\eta + \kappa)} + Pr \frac{\epsilon_2}{\epsilon_1} \frac{\kappa}{(\eta + \kappa)} \frac{(f_j + f_{j-1})}{2} \frac{(m_j + m_{j-1})}{2} - Pr \frac{\beta \eta \epsilon_2}{2\epsilon_1} \eta \frac{(m_j + m_{j-1})}{2} \right]^i = \quad (5.27)$$

$$N_{j-1/2},$$

$$\text{Where } N_{j-1/2} = - \left[\frac{\partial m}{\partial \eta} + \frac{1}{(\eta + \kappa)} m_{j-1/2} + Pr \frac{\epsilon_2}{\epsilon_1} \frac{\kappa}{(\eta + \kappa)} (fm)_{j-1/2} - Pr \frac{\epsilon_2 \beta}{\epsilon_1} \eta m_{j-1/2} \right]^{i-1}, \quad (5.28)$$

where $M_{j-1/2}$ is the sum of known terms of the linear momentum equation. Similarly, the momentum equation is discretized as done in the preceding case.

In view of Newton's linearization method. f, u, v, w, θ and m respectively by taking $f + \delta f, u + \delta u, v + \delta v, w + \delta w, \theta + \delta \theta$ and $m + \delta m$ lead to the following:

$$\delta f_j - \delta f_{j-1} - \frac{h_j}{2}(\delta u_j + \delta u_{j-1}) = (r_1)_j, \quad (5.29)$$

$$\delta u_j - \delta u_{j-1} - \frac{h_j}{2}(\delta v_j + \delta v_{j-1}) = (r_2)_j, \quad (5.30)$$

$$\delta v_j - \delta v_{j-1} - \frac{h_j}{2}(\delta w_j + \delta w_{j-1}) = (r_3)_j, \quad (5.31)$$

$$\delta \theta_j - \delta \theta_{j-1} - \frac{h_j}{2}(\delta m_j + \delta m_{j-1}) = (r_4)_j, \quad (5.32)$$

$$\begin{aligned}
&(a_1)_j \delta v_j + (a_2)_j \delta v_{j-1} + (a_3)_j \delta u_j + (a_4)_j \delta u_{j-1} + (a_5)_j \delta f_j + (a_6)_j \delta f_{j-1} + \\
&(a_7)_j \delta w_j + (a_8)_j \delta w_{j-1} + (a_9)_j \delta \theta_j + (a_{10})_j \delta \theta_{j-1} + (a_{11})_j \delta m_j + (a_{12})_j \delta m_{j-1} = \\
&(r_5)_j,
\end{aligned} \tag{5.33}$$

$$\begin{aligned}
&(b_1)_j \delta v_j + (b_2)_j \delta v_{j-1} + (b_3)_j \delta u_j + (b_4)_j \delta u_{j-1} + (b_5)_j \delta f_j + (b_6)_j \delta f_{j-1} + \\
&(b_7)_j \delta w_j + (b_8)_j \delta w_{j-1} + (b_9)_j \delta \theta_j + (b_{10})_j \delta \theta_{j-1} + (b_{11})_j \delta m_j + (b_{12})_j \delta m_{j-1} = \\
&(r_6)_j.
\end{aligned} \tag{5.34}$$

In matrix-vector form:

$$A\varphi = R. \tag{5.35}$$

If A is a block tri-diagonal matrix system, then

$$A = \begin{bmatrix} [A_1] & [C_1] & & & & & \\ [B_1] & [A_2] & \ddots & & & & \\ & \ddots & \ddots & & & & \\ & & & \ddots & & & \\ & & & & [B_{j-1}] & [A_{j-1}] & [C_{j-1}] \\ & & & & & [B_j] & [A_j] \end{bmatrix}, \quad \varphi = \begin{bmatrix} [\delta_1] \\ [\delta_2] \\ \vdots \\ [\delta_j] \end{bmatrix}, \tag{5.36}$$

$$[R_j] = \begin{bmatrix} (r_1)_j \\ (r_2)_j \\ \vdots \\ (r_6)_j \end{bmatrix}, \text{ where } [\delta_1] = \begin{bmatrix} \delta w_0 \\ \delta m_0 \\ \delta f_1 \\ \delta v_1 \\ \delta w_1 \\ \delta m_1 \end{bmatrix}, [\delta_j] = \begin{bmatrix} \delta u_{j-1} \\ \delta \theta_{j-1} \\ \delta f_j \\ \delta v_j \\ \delta w_j \\ \delta m_j \end{bmatrix}, R = \begin{bmatrix} [R_1] \\ [R_2] \\ \vdots \\ [R_j] \end{bmatrix}, \quad 2 \leq j \leq J. \tag{5.38}$$

This MATLAB based block elimination technique is employed to vet the presented results as a second check and found an excellent agreement.

For the computational purpose, the step size of $\Delta\eta = 0.001$ is considered and the results are obtained by setting the error tolerance to the order 10^{-6} in all the cases. Choosing the values of involved parameters is critical when it affects the computational time. Another inevitable source of error is the unbounded domain that must be finite for computational purposes. For numerical

simulations the step size or boundary layer edge which would sufficient enough to attain the boundary conditions asymptotically for all values of physical parameters is castoff, $\eta = 16$. The validation of results will be discussed in Table 5.1, which shows clearly that both the upper and lower solutions branches agree excellently with [41]. In addition, we now also have checked for the grid-independence of our solution. For the purpose, we increase the grid resolution by reducing the step size by half and compared the numerical results with the previous one. These two results are identical. Hence, we can regard our solution as a grid-independent.

Table 5.1 Comparison of $f''(0)$ for existing analytical and our numerical solutions

$$\kappa \rightarrow \infty, \beta = 0, S = 2, \phi = 0, M = 0,$$

| λ | Roşca and Pop [41] | | Current study | |
|-----------|--------------------|--------------|---------------|--------------|
| | Upper branch | Lower branch | Upper branch | Lower branch |
| -0.5 | 0.85355 | 0.14644 | 0.85355 | 0.14644 |
| -0.6 | 0.97947 | 0.22052 | 0.97947 | 0.22052 |
| -0.7 | 1.08340 | 0.31659 | 1.08340 | 0.31659 |
| -0.8 | 1.15777 | 0.44222 | 1.15777 | 0.44222 |
| -0.9 | 1.18460 | 0.61539 | 1.18460 | 0.61539 |
| -0.99 | 1.089 | 0.891 | 1.08900 | 0.89100 |

5.4 Results and Analysis

Graphical results of different physical quantities like velocity, pressure, temperature and skin friction profiles are executed in the below section using MATLAB software. **Figures 5.3** and **5.4** represents pressure distribution in fluid with shrinking and suction parameter respectively. It can be observed that pressure profile increases for raising the magnitude of shrinking and suction parameters.

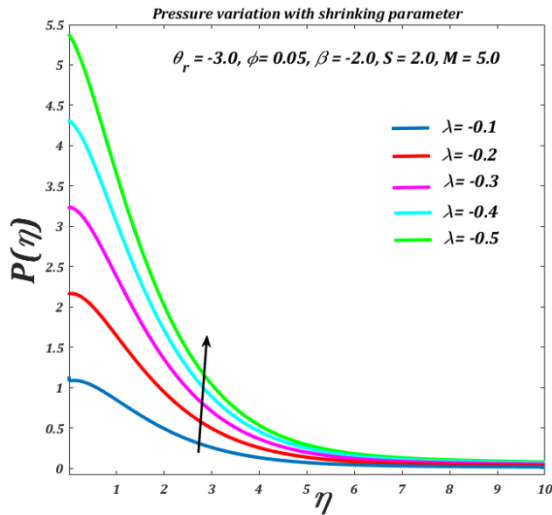


Figure 5.2 Pressure variations with Shrinking parameter

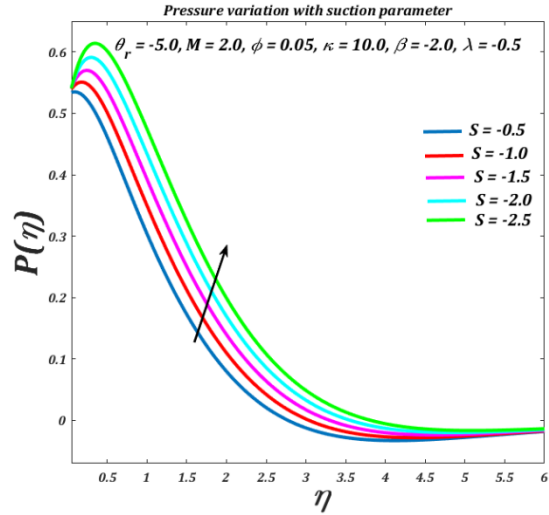


Figure 5.3 Pressure variations with Suction parameter

Figures (5.5-5.7) show skin friction plots opposite to the shrinking parameter. Graphic data shows that the coefficient of skin friction decreases for the increasing curvature parameter and escalates for the variable viscosity parameters both for the upper and lower solutions. For the suction parameter, the lower and the upper solution skin friction profiles are in opposite conduct as can be verified in Figure 5.7 Since the skin friction profile increases in the case of the upper solution branch, whereas, it decreases in the case of lower solution branch. It is learnt that the critical value of the shrinking parameter increases in the negative direction with the rising magnitude of the suction parameter as shown in Figure 5.7. On the other hand, these critical values remain the same for increasing curvature parameter and variable viscosity parameter as seen in Figures 5.5 and 5.6.

Figures (5.8-5.10) offer skin friction graphs opposite to that of the suction parameter. It was revealed that skin friction profile decreases when increase in curvature parameter values occur, whereas it increases with variable viscosity parameter. For the shrinking parameter, the coefficient of skin friction increases for both the upper and lower branches of the solution. Although the critical values, in this case, vary, as input for the shrinking parameter is changed. It is obvious and can be seen from Figure 5.9 that when the extent of the shrinking parameter is increased the critical value of the suction parameter also increased, whereas in the case of curvature and variable viscosity parameter the critical points are invariant as noticed in Figures 5.8 and 5.10.

Both the velocity and velocity gradient graphs with various parameters are plotted in **Figures (5.11-5.14)** for two different solutions. The velocity distribution decreases in magnitude for increasing values of shrinking parameter, while the velocity gradient also increases with higher values of the shrinking parameter as shown in **Figures 5.11 and 5.12** for both upper and lower branch solutions. The two solutions exhibit the opposite trend for the suction parameter in the velocity profile. The lower branch velocity profile lessens in magnitude with the growing suction parameter values while increasing for the upper branch of the solution as shown in **Figures 5.13 and 5.14**. For both upper and lower cases, the magnetic parameter weakens the velocity distribution along r-direction as evident from **Figure 5.15** as well as along s-direction as can be seen in **Figure 5.16**.

The plots of **Figures (5.17-5.20)** represent temperature variation with different physical parameters. It can be realized in **Figure 5.17** that temperature rises as the curvature parameter increases. The same is the case for CNT's volume fraction as revealed in **Figure 5.18**. However, the suction parameter reduces the temperature as noticed in **Figure 5.19**. From **Figure 5.20**, it can be concluded that a rise in the variable viscosity increases the fluid temperature.

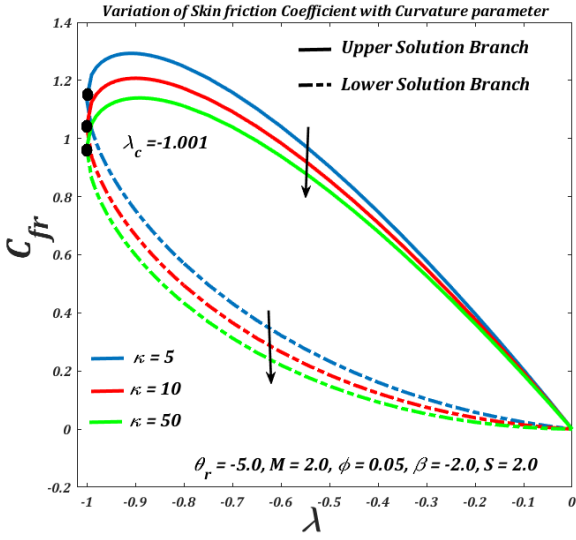


Figure 5.4 Skin friction versus Curvature parameter

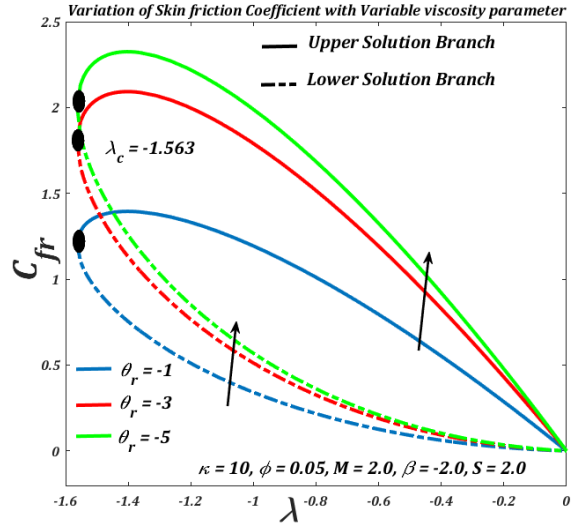


Figure 5.5 Skin friction versus variable Viscosity parameter

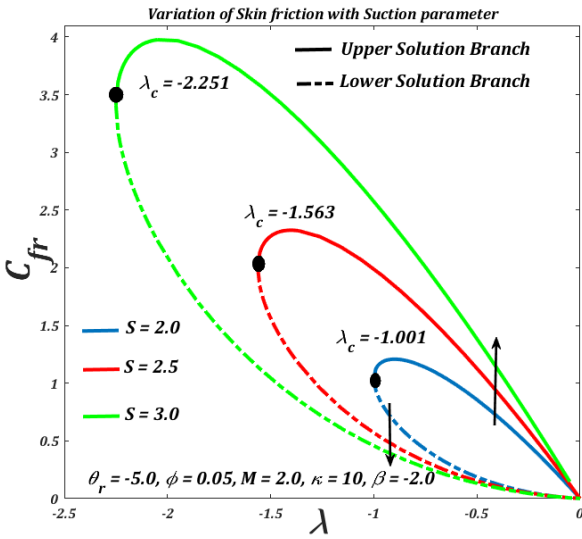


Figure 5.6 Skin friction versus Porosity parameter

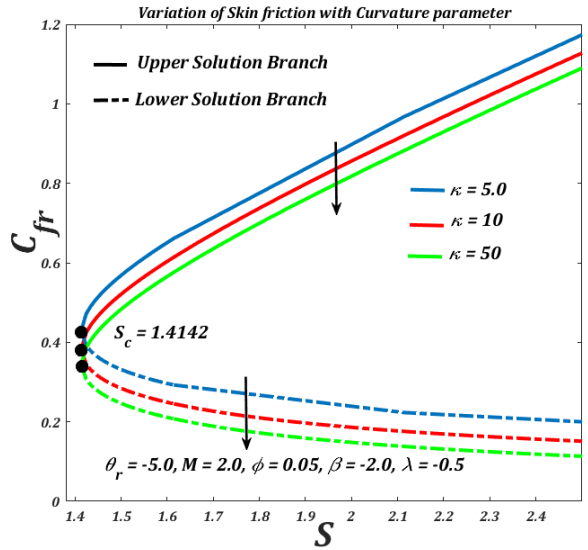


Figure 5.7 Skin friction versus Curvature and Suction parameter

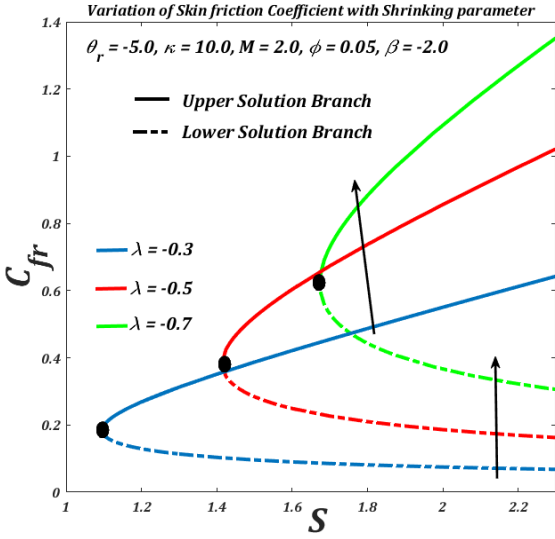


Figure 5.8 Skin friction versus Shrinking parameter

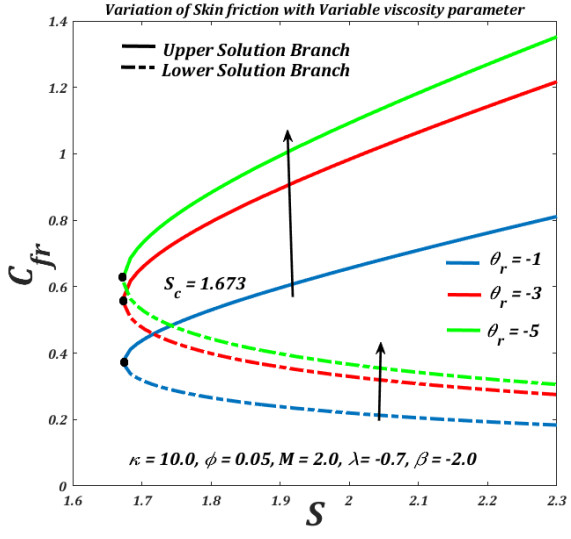


Figure 5.9 Skin friction versus variable Viscosity parameter

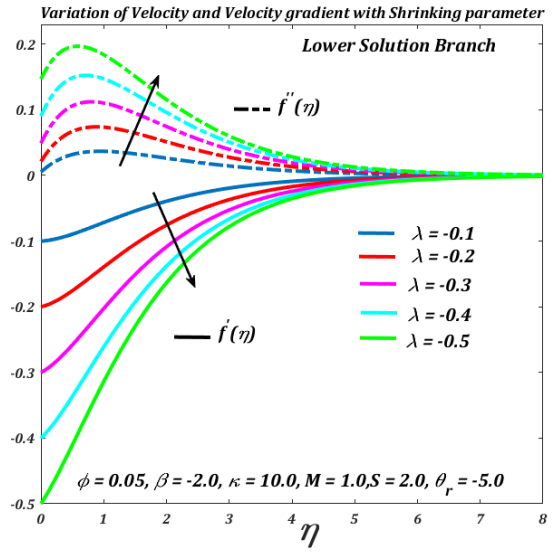


Figure 5.10 Velocity and Velocity gradient with Shrinking parameter (Lower Solution)

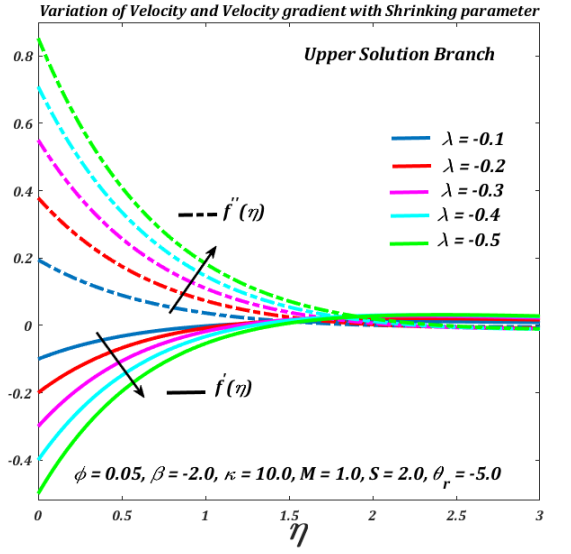


Figure 5.11 Velocity and Velocity gradient with Shrinking parameter (Upper Solution)

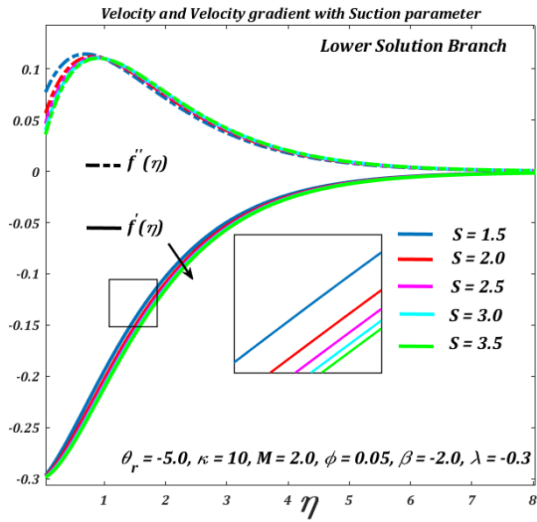


Figure 5.12 Velocity and Velocity gradient versus Suction parameter (Lower Solution)

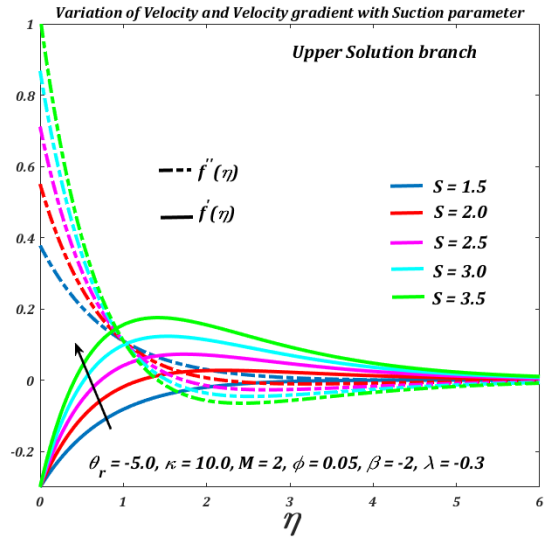


Figure 5.13 Velocity and Velocity gradient versus Suction parameter (Upper Solution)

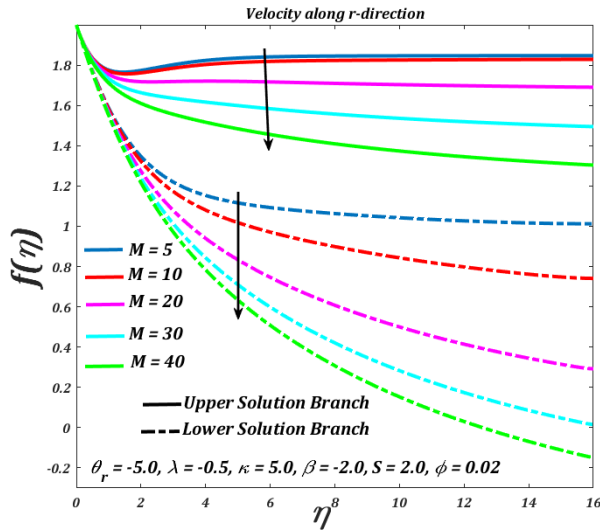


Figure 5.14 Velocity along r-direction

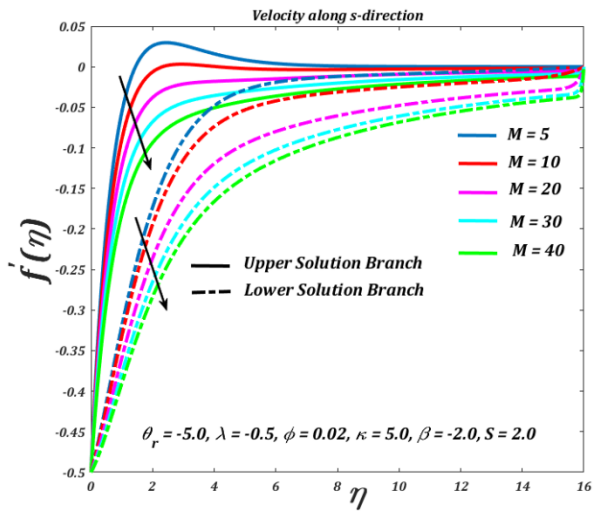


Figure 5.15 Velocity along s-direction

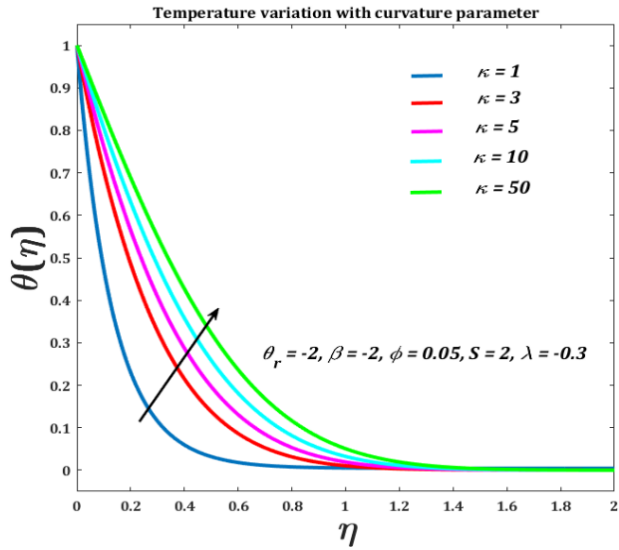


Figure 5.16 Temperature variation versus Curvature parameter

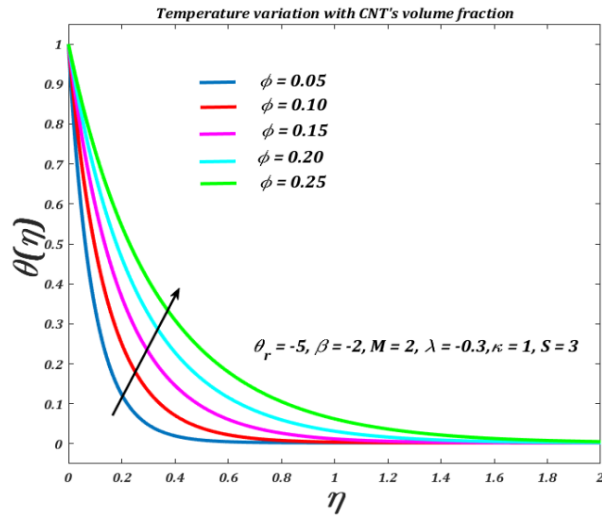


Figure 5.17 Temperature variation versus CNT volume fraction

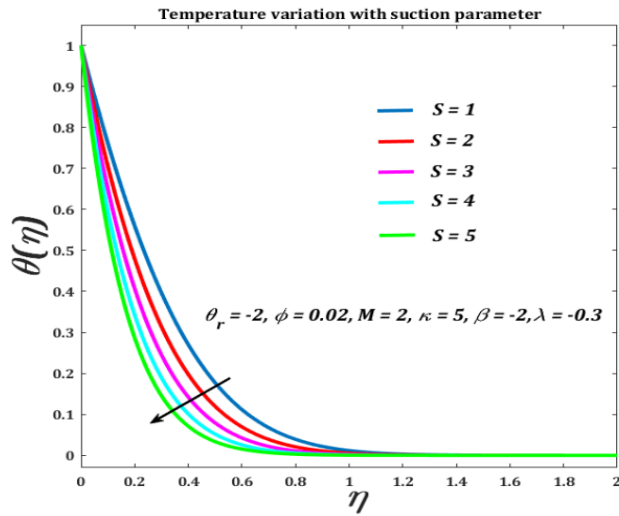


Figure 5.18 Temperature variation versus Suction parameter

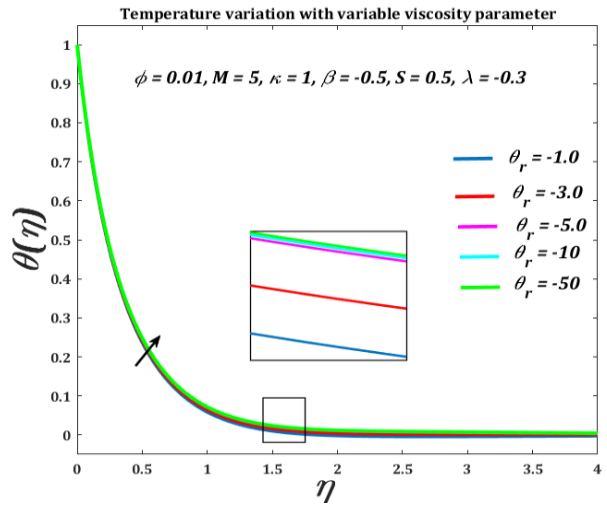


Figure 5.19 Temperature variation versus variable Viscosity parameter

6 Computational study of CNT nanofluid flow on a curved surface with micro-rotational inertia

6.1 Introduction

This chapter provides a computational study of the nanofluid flow on the curvilinear surface in the presence of the magnetic field. Carbon nanotubes are considered to be the solid constituent. The fluid is viscous with viscosity depending inversely on the temperature of the fluid. Micro-rotations and spin motions are also taken into considerations. Eringen micropolar fluids theory is used to model the problem in the curvilinear coordinates system. The set of equations depicting the above situations are non-linear coupled partial differential equations, which are first converted to a system of ordinary differential equations and then numerically addressed using an affective finite differential technique. Numerical and graphical results of quantities of physical significance are presented and discussed, such as Nusselt number, skin friction, and couple stress.

6.2 Mathematical description

Let us consider a steady incompressible nanofluid flow on a curved surface as shown in **Figure 5.1** Single-walled carbon nanotubes are taken as the solid part of the nanofluid with the viscosity varying as an inverse function of temperature. U_w is the velocity with which the surface is stretched while V_w represents the mass transfer velocity through the permeable surface. Though for electrically conducting fluid the induced magnetic field is neglected, there exists an applied uniform magnetic field acting along the r -direction. The fluid particles are assumed to possess rotational as well as spin inertia. The equations below are derived using the Eringen theory of micro fluids that can be regarded as a generalized form of classical Navier-Stokes theory.

The overruling equations in curvilinear coordinates are:

$$R \frac{\partial u}{\partial s} + \frac{\partial}{\partial r} [(r + R)v] = 0, \quad (6.1)$$

$$\begin{aligned}
\rho_{nf} \left(v \frac{\partial v}{\partial r} - \frac{u^2}{r+R} + u \left(\frac{R}{r+R} \right) \frac{\partial v}{\partial s} \right) \\
= -\frac{\partial p}{\partial r} + \frac{R}{(r+R)} \frac{\partial}{\partial s} \left(\mu_{nf} \left(\frac{\partial u}{\partial r} + \frac{R}{(r+R)} \frac{\partial v}{\partial s} - \frac{u}{r+R} \right) \right) \\
+ \frac{1}{(r+R)} \frac{\partial}{\partial r} \left((r+R) \mu_{nf} \frac{\partial v}{\partial r} \right) - \frac{1}{r+R} \mu_{nf} \left(\frac{\partial u}{\partial r} + \frac{R}{(r+R)} \frac{\partial v}{\partial s} - \frac{u}{r+R} \right),
\end{aligned} \tag{6.2}$$

$$\begin{aligned}
\rho_{nf} \left(v \frac{\partial u}{\partial r} + \frac{uv}{r+R} + u \left(\frac{R}{r+R} \right) \frac{\partial u}{\partial s} \right) \\
= -\frac{R}{(r+R)} \frac{\partial p}{\partial s} + \frac{\partial}{\partial r} \left((\mu_{nf} + K_1) \left(\frac{\partial u}{\partial r} - \frac{u}{r+R} \right) \right) - K_1 \frac{\partial N}{\partial r} - \sigma B^2 u,
\end{aligned} \tag{6.3}$$

$$\begin{aligned}
\rho_{nf} j \left(u \left(\frac{R}{r+R} \right) \frac{\partial N}{\partial s} + v \frac{\partial N}{\partial r} \right) \\
= -\frac{1}{(r+R)} \frac{\partial}{\partial r} \left(\gamma^* (r+R) \frac{\partial N}{\partial r} \right) - K_1 \left(2N + \frac{\partial u}{\partial r} + \frac{u}{(r+R)} \right)
\end{aligned} \tag{6.4}$$

$$\frac{R}{(r+R)} \frac{\partial T}{\partial s} + v \frac{\partial T}{\partial r} = \alpha_{nf} \left(\frac{1}{(r+R)} \frac{\partial T}{\partial r} + \frac{\partial^2 T}{\partial r^2} \right) \tag{6.5}$$

The relevant boundary conditions are:

$$\left. \begin{aligned}
u &= \lambda U_w(s) & v &= V_w(s, t) & T &= T_w & \text{at} & r = 0 \\
u &\rightarrow 0, & \frac{\partial u}{\partial r} &\rightarrow 0 & T &= T_\infty & \text{at} & r \rightarrow \infty
\end{aligned} \right\} \tag{6.6}$$

N is the angular velocity of the fluid element, K_1 represent the micro-rotation viscosity of the fluid whereas $\gamma^* = j(\mu_{nf} + \frac{K_1}{2})$ is the spin gradient viscosity of the fluid. j is the micro-inertial density. $U_w(s)$ is the surface stretching velocity, which is taken as $U_w(s) = as$, a is a dimensionless positive constant. λ is a dimensionless constant known as a stretching parameter. For stretching we only put $\lambda > 0$ Also we have taken $V_w = -\sqrt{av_\infty}S$, where S is a constant parameter that represents mass transfer through the surface. Since we have considered the suction phenomena throughout the study. For suction, we have $S > 0$.

Incorporating boundary layer approximation for very large Reynolds number values, the nonlinear partial differential equations described above are reduced to the form given below.

$$\rho_{nf} \left(\frac{u^2}{r+R} \right) = \frac{\partial p}{\partial r} \tag{6.7}$$

$$\rho_{nf} \left(v \frac{\partial u}{\partial r} + u \left(\frac{R}{r+R} \right) \frac{\partial u}{\partial s} + \frac{uv}{r+R} \right) = - \frac{R}{(r+R)} \frac{\partial p}{\partial s} + (\mu_{nf} + K_1) \frac{\partial^2 u}{\partial r^2} - \frac{\partial \mu_{nf}}{\partial r} \frac{u}{(r+R)} + \frac{\partial \mu_{nf}}{\partial r} \frac{\partial u}{\partial r} - K_1 \frac{\partial N}{\partial r} - \sigma B^2 u, \quad (6.8)$$

$$\begin{aligned} \rho_{nf} j \left(u \left(\frac{R}{r+R} \right) \frac{\partial N}{\partial s} + v \frac{\partial N}{\partial r} \right) \\ = - \frac{1}{(r+R)} \frac{\partial}{\partial r} \left(\gamma^*(r+R) \frac{\partial N}{\partial r} \right) - K_1 \left(2N + \frac{u}{(r+R)} + \frac{\partial u}{\partial r} \right) \end{aligned} \quad (6.9)$$

$$v \frac{\partial T}{\partial r} + \frac{R}{(r+R)} \frac{\partial T}{\partial s} = \alpha_{nf} \left(\frac{\partial^2 T}{\partial r^2} + \frac{1}{(r+R)} \frac{\partial T}{\partial r} \right) \quad (6.9)$$

The boundary conditions now are:

$$\left. \begin{aligned} u = \lambda as, \quad v = -\sqrt{av_\infty} S, \quad T = T_w \quad \text{at} \quad r = 0, \\ u \rightarrow 0, \quad \frac{\partial u}{\partial r} \rightarrow 0 \quad T = T_\infty \quad \text{at} \quad r \rightarrow \infty. \end{aligned} \right\} \quad (6.10)$$

Choosing suitable similarity transformations and introducing dimensionless functions f , θ , and similarity variable η

$$\begin{aligned} u = asf'(\eta), \quad v = -\frac{R}{r+R} \sqrt{av_\infty} f(\eta), \quad \theta = \frac{T - T_\infty}{T_w - T_\infty}, \\ \eta = \sqrt{\frac{a}{v_\infty}} r, \quad p = \rho_{nf} a^2 s^2 P(\eta) \end{aligned} \quad (6.11)$$

The momentum and energy equations are transformed into the following system of non-linear Ordinary Differential Equations by applying the similarity transformations above:

$$\frac{\partial P}{\partial \eta} = \frac{f'^2}{\eta + \kappa} \quad (6.12)$$

$$\begin{aligned} \frac{2\kappa}{(\eta + \kappa)} P(\eta) = \frac{1}{A_1} \left((1 + K(1 - \phi)^{2.5}) \left(\frac{f'''}{(1 - \frac{\theta}{\theta_r})} + \frac{1}{(\eta + \kappa)} \frac{f''}{(1 - \frac{\theta}{\theta_r})} - \frac{1}{(\eta + \kappa)^2} \frac{f'}{(1 - \frac{\theta}{\theta_r})} \right) - \right. \\ \left. \frac{1}{(\eta + \kappa)} \frac{f' \theta'}{\theta_r (1 - \frac{\theta}{\theta_r})^2} + \frac{f'' \theta'}{\theta_r (1 - \frac{\theta}{\theta_r})^2} - M_1 f' \right) + \frac{\kappa}{(\eta + \kappa)} \left(f f'' - f'^2 + \frac{1}{(\eta + \kappa)} f f' \right) - \frac{K(1 - \phi)^{2.5}}{A_1} g' \end{aligned} \quad (6.13)$$

$$\left(\frac{1}{\left(1 - \frac{\theta}{\theta_r}\right)} + \frac{K(1 - \phi)^{2.5}}{2} \right) \left(g'' + \frac{g'}{(\eta + \kappa)} + \frac{g'\theta'}{\theta_r \left(1 - \frac{\theta}{\theta_r}\right)^2} \right) - K(1 - \phi)^{2.5} \left(2g + f'' + \frac{f'}{(\eta + \kappa)} \right) + A_1 \frac{\kappa}{(\eta + \kappa)} (fg' - f'g) = 0 \quad (6.14)$$

$$\theta'' + \frac{1}{(\eta + \kappa)} \theta' + Pr \frac{\epsilon_2}{\epsilon_1} \frac{\kappa}{(\eta + \kappa)} f \theta' = 0 \quad (6.15)$$

Using Equation 6.12 into 6.13 we get

$$\begin{aligned} & (1 + K(1 - \phi)^{2.5}) \left(\frac{(\eta + \kappa)f^{iv}}{\left(1 - \frac{\theta}{\theta_r}\right)} + \frac{2f'''}{\left(1 - \frac{\theta}{\theta_r}\right)} - \frac{1}{(\eta + \kappa)} \frac{f''}{\left(1 - \frac{\theta}{\theta_r}\right)} + \frac{1}{(\eta + \kappa)^2} \frac{f'}{\left(1 - \frac{\theta}{\theta_r}\right)} \right) + \frac{2(\eta + \kappa)f'''\theta'}{\theta_r \left(1 - \frac{\theta}{\theta_r}\right)^2} + \\ & \frac{f''\theta'}{\theta_r \left(1 - \frac{\theta}{\theta_r}\right)^2} - \frac{f'\theta''}{\theta_r \left(1 - \frac{\theta}{\theta_r}\right)^2} - \frac{2f'\theta'}{\theta_r^2 \left(1 - \frac{\theta}{\theta_r}\right)^3} + \frac{(\eta + \kappa)f''\theta''}{\theta_r \left(1 - \frac{\theta}{\theta_r}\right)^2} + \frac{2(\eta + \kappa)f''\theta'}{\theta_r^2 \left(1 - \frac{\theta}{\theta_r}\right)^3} - \frac{1}{(\eta + \kappa)} \frac{f'\theta'}{\theta_r \left(1 - \frac{\theta}{\theta_r}\right)^2} - \\ & M_1(f' + (\eta + \kappa)f'') + \kappa A_1(ff'' - f'f''') + \frac{\kappa}{(\eta + \kappa)} A_1 \left(ff'' - f'^2 - \frac{1}{(\eta + \kappa)} ff' \right) - \\ & K(1 - \phi)^{2.5} \left(\frac{(\eta + \kappa)g''}{\left(1 - \frac{\theta}{\theta_r}\right)} + \frac{g'}{\left(1 - \frac{\theta}{\theta_r}\right)} \right) = 0 \end{aligned} \quad (6.16)$$

$$\left(\frac{1}{\left(1 - \frac{\theta}{\theta_r}\right)} + \frac{K(1 - \phi)^{2.5}}{2} \right) \left(g'' + \frac{g'}{(\eta + \kappa)} + \frac{g'\theta'}{\theta_r \left(1 - \frac{\theta}{\theta_r}\right)^2} \right) - K(1 - \phi)^{2.5} \left(2g + f'' + \frac{f'}{(\eta + \kappa)} \right) + A_1 \frac{\kappa}{(\eta + \kappa)} (fg' - f'g) = 0 \quad (6.17)$$

$$\theta'' + \frac{1}{(\eta + \kappa)} \theta' + Pr \frac{\epsilon_2}{\epsilon_1} \frac{\kappa}{(\eta + \kappa)} f \theta' = 0 \quad (6.18)$$

Now the boundary conditions in the dimensionless form are:

$$f = S, \quad f' = \lambda, \quad \theta = 1 \quad \text{at } \eta = 0$$

$$f' \rightarrow 0, \quad f'' \rightarrow 0, \quad \theta \rightarrow 0 \quad \text{as } \eta \rightarrow \infty$$

We are also interested in finding the skin friction coefficient (C_{fr}), Couple stress (C_{mr}) and Nusselt number (Nu) near the boundaries, which can be written as $C_{fr} Re_s^{1/2} =$

$$\frac{1}{(1-\phi)^{2.5}\left(1-\frac{1}{\theta_r}\right)}(1+K)\left(f''(0)-\frac{1}{\kappa}\right), C_{mr}Re_s^{1/2} = \frac{1}{(1-\phi)^{2.5}\left(1-\frac{1}{\theta_r}\right)}\left(1+\frac{K}{2}\right)\left(g'(0)-N_0\frac{f''(0)}{\kappa}\right) \text{ and}$$

$$NuRe_s^{1/2} = -\epsilon_1\theta'(0), \text{ where } Re_s = \frac{as^2}{\nu_{f\infty}} \text{ is the local Reynolds number.}$$

6.3 Solution procedure:

Eringen theory of micropolar fluid is used to model the assumed problem. The governing set of equations is a Set of five non-linear partial differential equations in curvilinear coordinates. Boundary layer approximation is incorporate on the system of equations to avoid the terms of negligible effects. Suitable similarity transformations are implemented in the system. The reduced model is now a series of ordinary differential equations which are strongly nonlinear in nature. The entity of temperature-dependent viscosity molds the momentum equations highly non-linear. A powerful finite difference method “Keller box” is incorporated to work out the solution of the governing set of coupled non-linear differential equations. This technique is composed of four distinct procedures. The very first step is the transformation of governing equations into a series of differential equations of the first order. In the second phase, these equations are discretized using a central difference scheme, followed by linearization with Newton’s linearization. The very last step is to write the linearized set of algebraic equations into block tri-diagonal form and solve them by matrix algebra. Numerical and graphical results are obtained by programming this very last step into MATLAB. The simplest case of the problem is matched with a previously published test for solution authentication purposes. As can be seen, in *Table. 4.1.* the data appear to be in very good agreement with the reported results. Tecplot 360 is also utilized to plot streamlines and isotherms. $\eta_{\infty} = 16$ is set as the edge of the boundary layer. A very fine Step size of $\Delta \eta = 0.005$ is taken for the calculations. Error tolerance is set at 10^{-6} .

6.4 Results and Analysis

Equations (6.16 – 6.18) are governing non-linear ordinary differential equations. The above system of simultaneous equations is solved numerically with a powerful finite difference scheme with the help of MATLAB software. Numerical results obtained are then represented graphically with the help of MATLAB and Tecplot graphic utility. **Figure 6.1** and **Figure 6.2** show streamline patterns and pressure variation respectively.

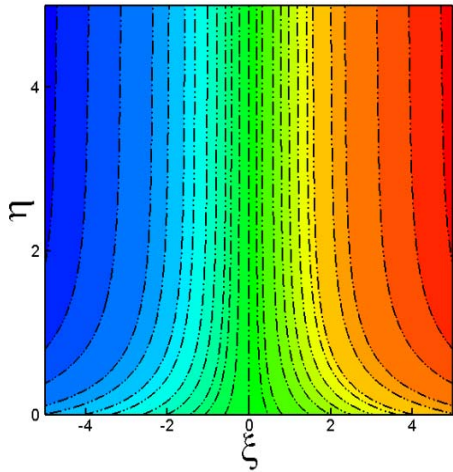


Figure 6.1 Streamlines patterns

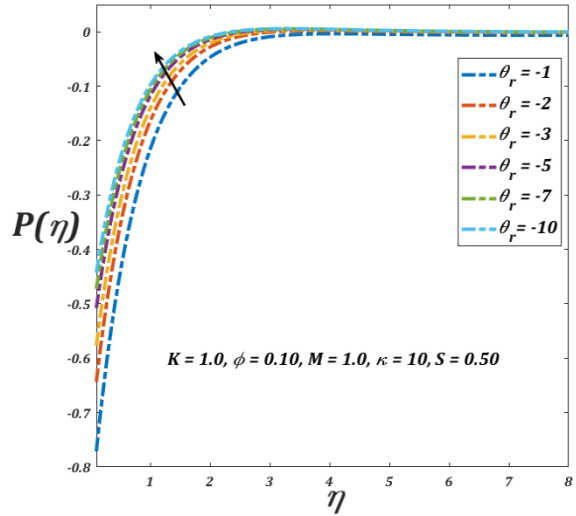


Figure 6.2 Pressure distribution with variable Viscosity parameter

Figures (6.3-6.11) are the isotherm plots executed with different physical parameters. It can be concluded from the results that temperature distribution within the fluid rises with an increase in the curvature parameter as well as with the solid fractions of single-walled carbon nanotubes. Suction, on the other hand, lowers the temperature distribution within the fluid as can be seen in Figures (6.9-6.11).

Velocity profile along s-direction is represented in Figures (6.12-6.15) with respect to different physical parameters. It can be seen that flow is opposed by suction as well as the curvature parameter. The flow of the fluid rises for increasing the values of the Hartmann parameter.

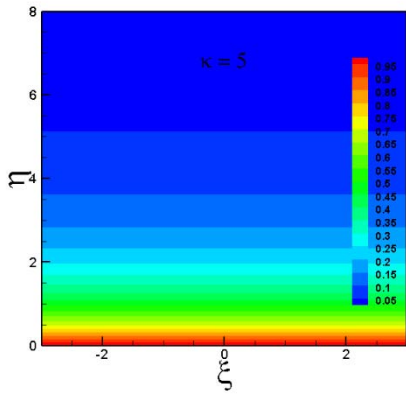


Figure 6.3 Isotherm with $k = 5$

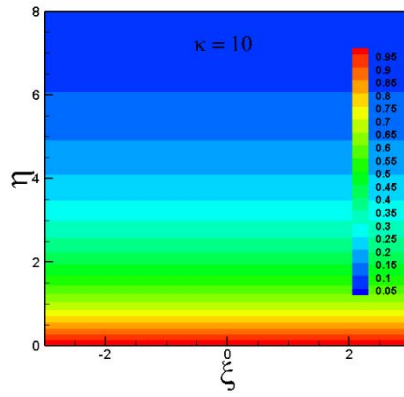


Figure 6.4 Isotherm with $k = 10$

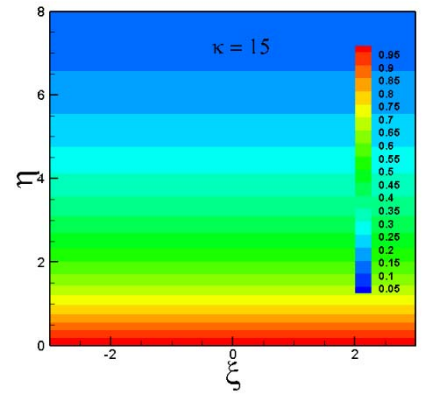


Figure 6.5 Isotherm with $k = 15$

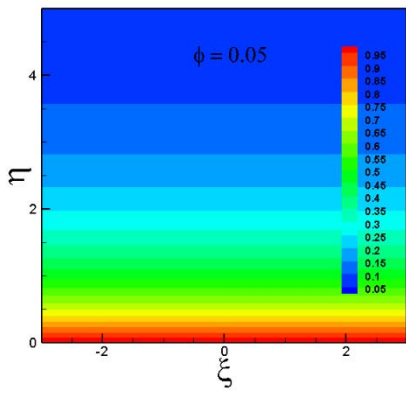


Figure 6.6 Isotherm with $\phi = 0.05$

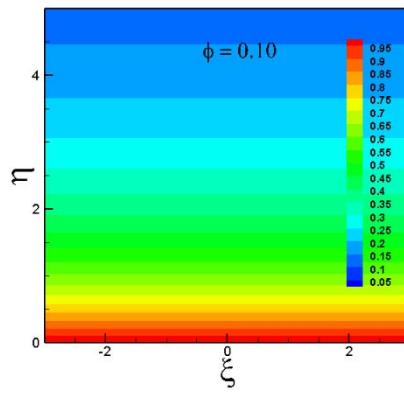


Figure 6.7 Isotherm with $\phi = 0.10$

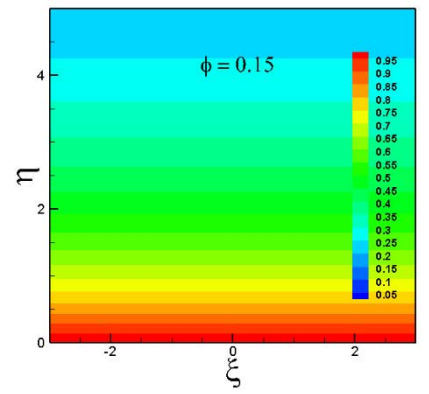


Figure 6.8 Isotherm with $\phi = 0.15$

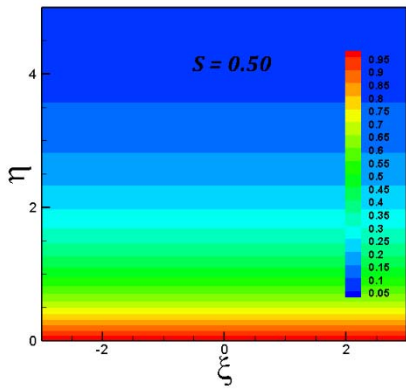


Figure 6.9 Isotherm with $S = 0.50$

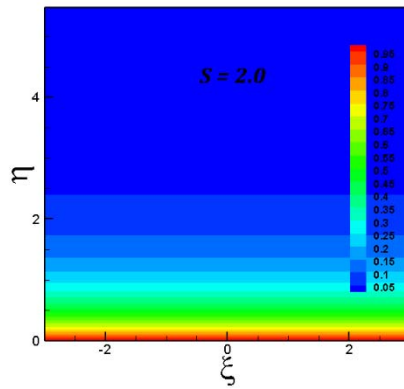


Figure 6.10 Isotherm with $S = 2.0$

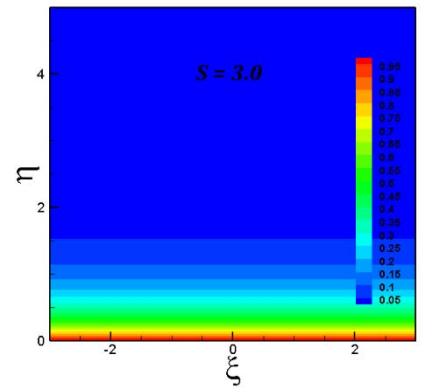


Figure 6.11 Isotherm with $S = 3.0$

Figures (6.16-6.19) depict variations in the skin friction coefficient near the boundaries, where Figures (6.19-6.23) are a couple stress plots near the curved surface. Graphical results show that both the skin friction and couple stress parameter decrease for the micropolar parameter, variable viscosity parameter, and suction parameter.

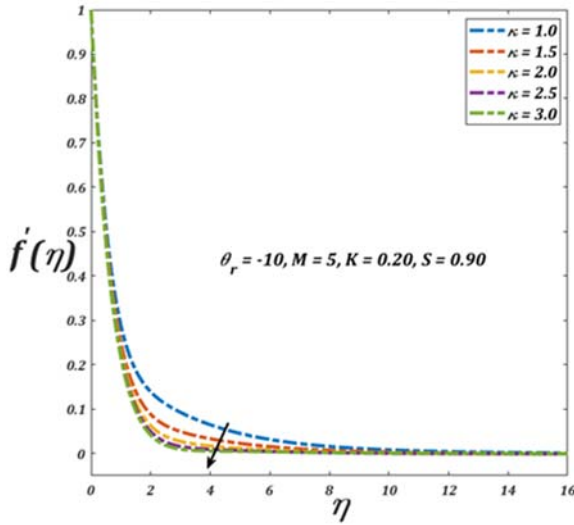


Figure 6.12 Velocity variations versus Curvature parameter

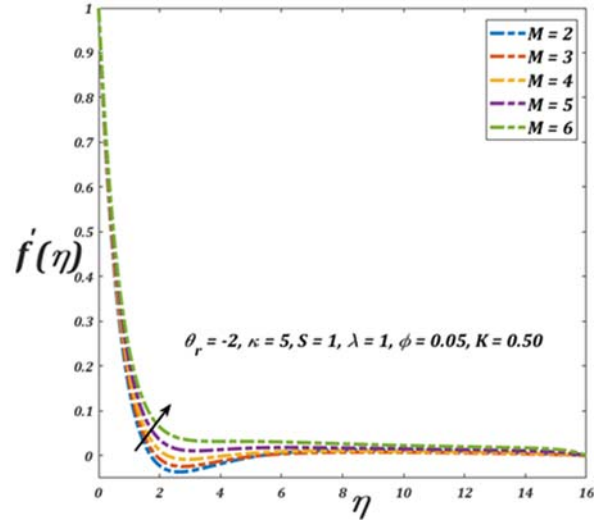


Figure 6.13 Velocity variations versus Magnetic parameter

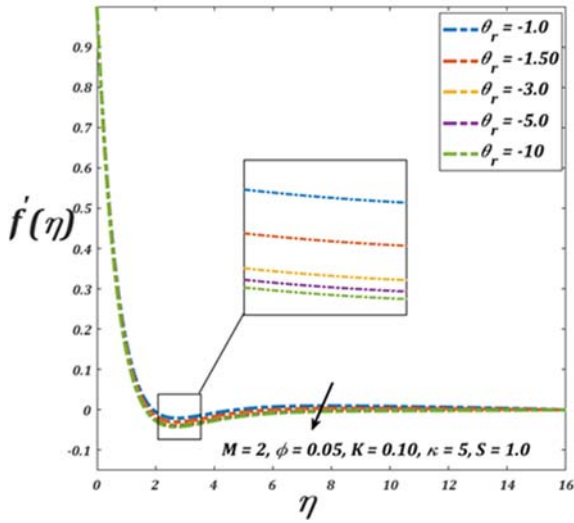


Figure 6.14 Velocity variations versus variable viscosity parameter

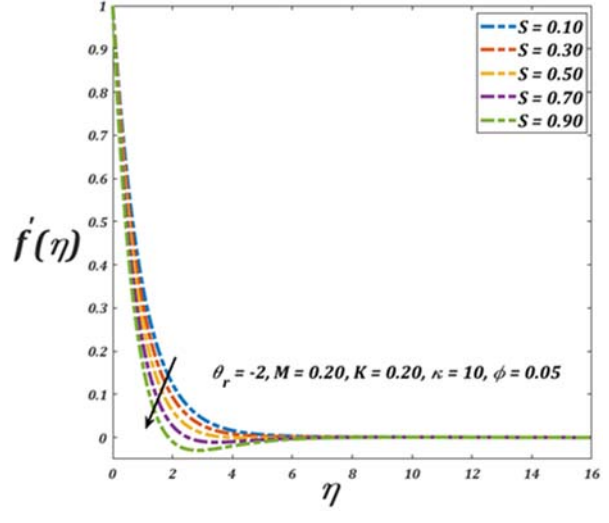


Figure 6.15 Velocity variations versus Porosity parameter

Besides that, a decrease in couple stress with rising values of the magnetic parameter can be noticed in **Figure 6.23**. For the ascending magnitude of the curvature parameter, it is evident from the study that the skin friction profile increases whereas the couple stress decreases.

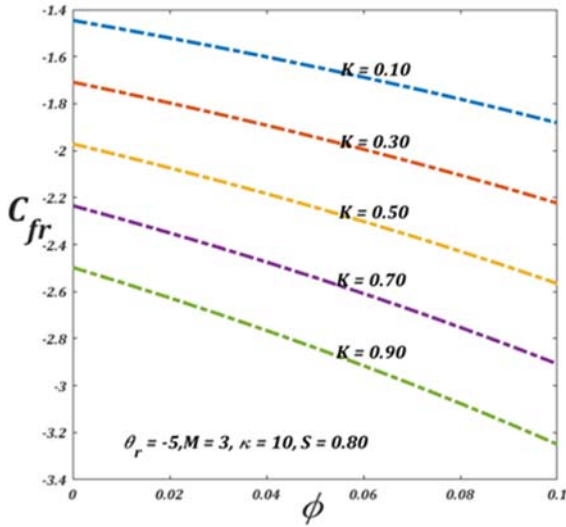


Figure 6.16 Skin friction versus Micropolar parameter

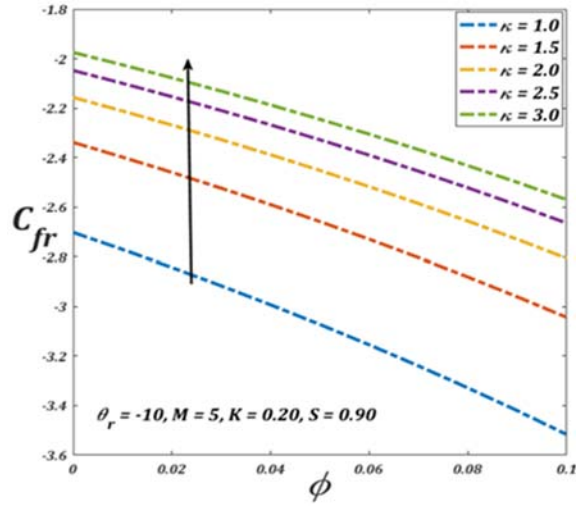


Figure 6.17 Skin friction versus Curvature parameter

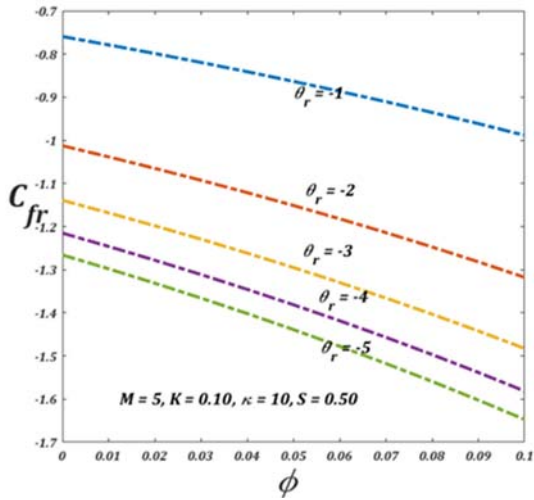


Figure 6.18 Skin friction versus Variable viscosity parameter

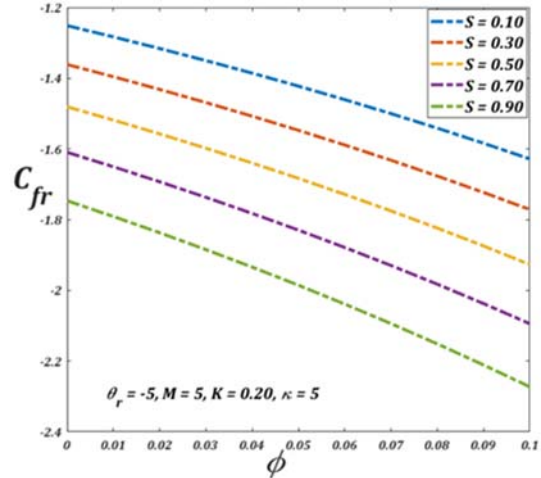


Figure 6.19 Skin friction versus Porosity parameter

The behavior of temperature gradient near the surface can be understood with the help of Nusselt number versus solid fraction graphs mentioned as **Figures (6.24-6.27)**. Heat transfer

near walls for both multi-walled and single-walled carbon nanotubes is compared in **Figure 6.24** for increasing Prandtl number.

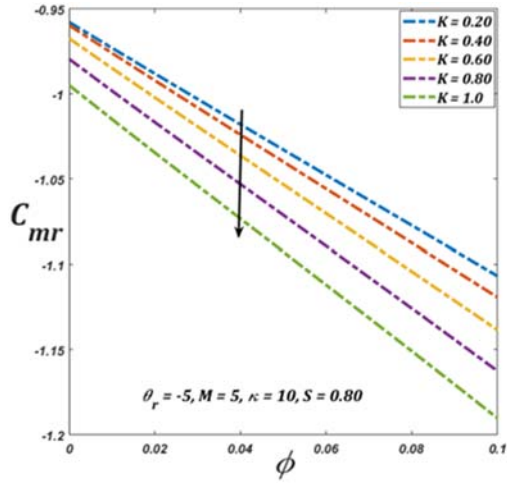


Figure 6.20 Couple stress variations with Micropolar parameter

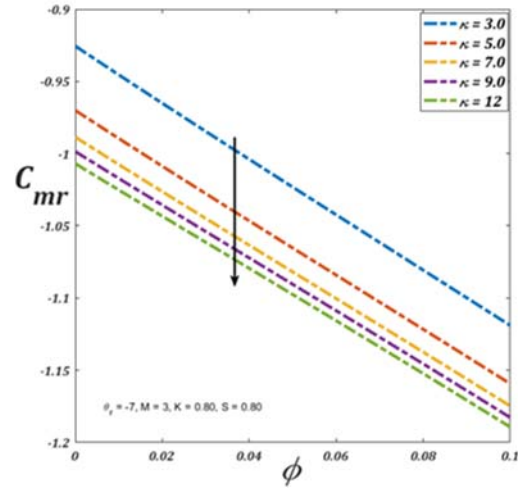


Figure 6.21 Couple stress variations with Curvature parameter

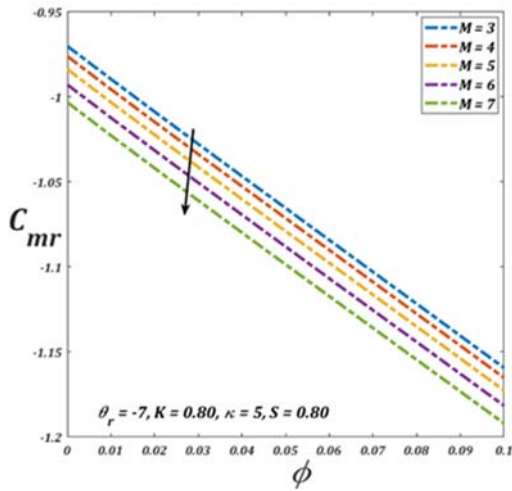


Figure 6.22 Couple stress variations with Magnetic parameter

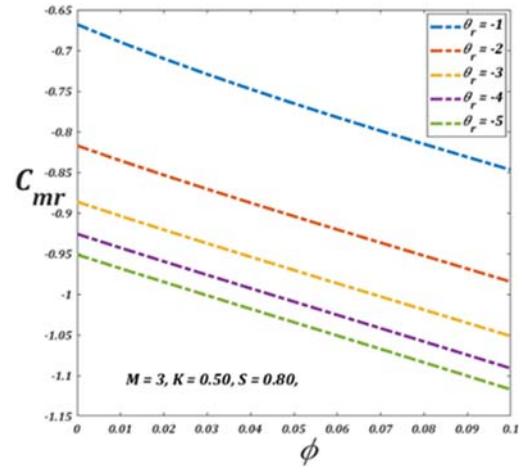


Figure 6.23 Couple stress variations with variable Viscosity parameters

It is concluded that both SWCNT and MWCNT exhibit similar behavior for changing values of Prandtl number. i.e. In both of the cases, Nusselt number increases in magnitude, however SWCNT as solid constituent always enhances the heat transfer capability of the fluid as can be seen. **Figure 6.26** and **Figure 6.27** show a decrease in Nusselt number with growing parameters of curvature and variable viscosity, whereas **Figure 6.28** validates an increment in the temperature gradient near the wall with increasing values of the suction parameter.

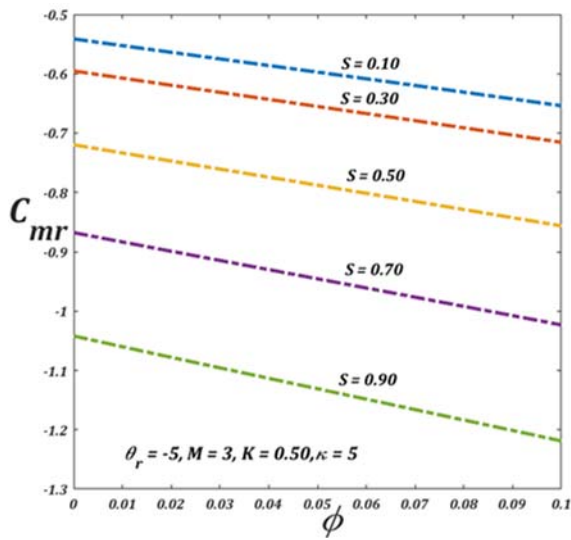


Figure 6.24 Couple stress variations with Porosity parameter

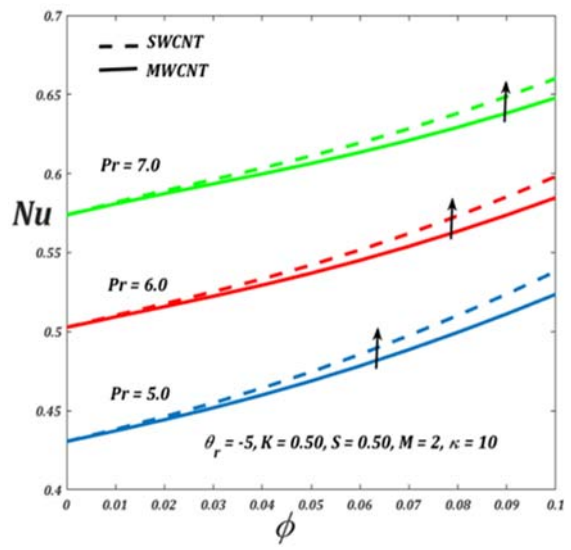


Figure 6.25 Nusselt number variations with Prandtl number for SWCNT and MWCNT

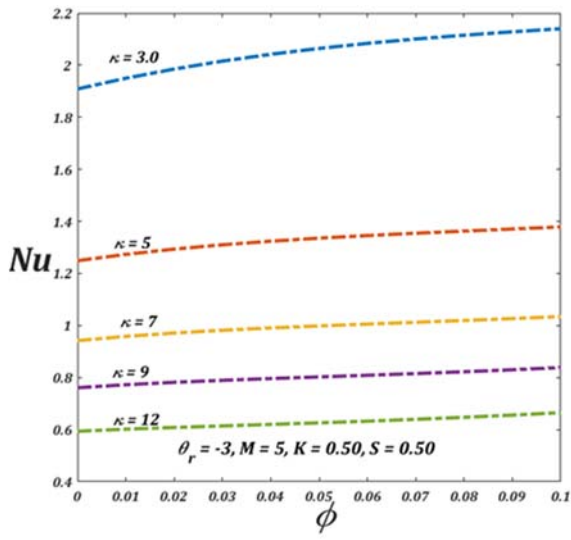


Figure 6.26 Nusselt number variations with Curvature parameter

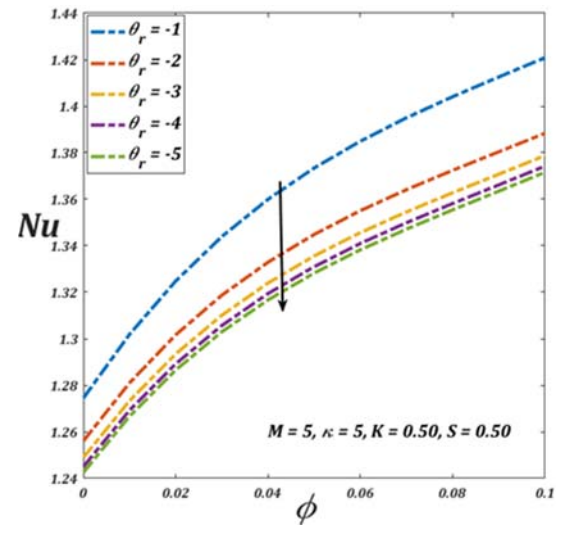


Figure 6.27 Nusselt number variations with variable viscosity parameters

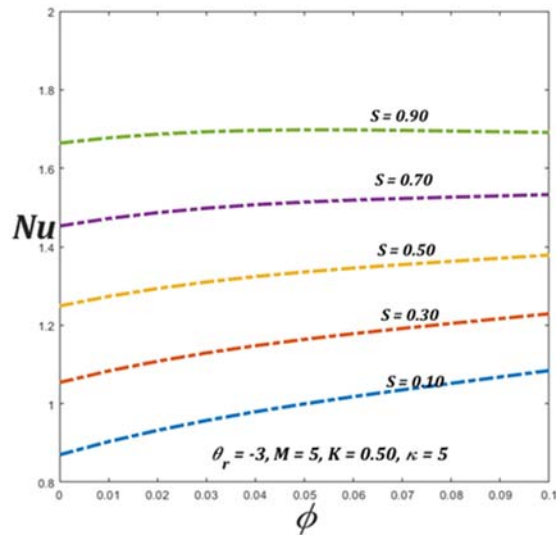


Figure 6.28 Nusselt number variations with Porosity parameter

7 Thesis Conclusion

This thesis represents the implications of powerful Numerical schemes on different fluid flow problems. Two major types of geometrical situations are examined. The channel flow between two plates and a semi-infinite boundary layer flow. Nanofluids are considered as the types of fluids possess the high potential of industrial application due to their efficient capabilities of heat transfer. Water is taken as a base-fluid, whereas carbon nanotubes are chosen as a solid constituent in this work, since they are among the nano-particles of exceptional properties, such as low density and high thermal heat capacity. In particular, single-walled carbon nanotubes are used as they work more effectively than that of multi-walled carbon nanotubes. A comparison of both multi-walled and single-walled carbon nanotubes is also presented. Fluids are considered viscous whose linear as well as rotational behavior in different geometrical situations are studied.

The second and third chapters represent the case of fluid flow between two plates at a finite distance from each other. These plates squeezed towards each other with a certain velocity. Numerical investigations are accomplished to analyzed the viscous flows through the squeezing channel. The equations which govern these physical situations are originally partial differential equations which are converted by appropriate transformations into ordinary differential equations. The solution of differential equations which have emerged are carried out numerically by finite difference schemes. Graphical and numerical results are obtained keeping dynamic viscosity variable. It is set to vary inversely with fluid temperature.

It can be concluded from the data obtained that linear flow momentum is enhanced by the magnitude of the unsteady magnetic field as well as with plates squeezing parameters, where the same decreases with the values of variable viscosity parameter and thermal radiation parameter. The study evidently concluded a fall in magnitude of linear momentum as the magnitude of the micro-rotations parameter is increased.

Temperature distribution across the flow channel depicts a fall with the squeezing parameter, whereas this temperature profile shows a rise in magnitude with the volume fraction of solid constituent of carbon nanotubes, variable viscosity parameter as well as with radiation parameter.

The angular velocity profile is found to be strengthened by the applied external magnetic field and viscosity parameter while it falls in strength along the channel with values of the micropolar parameter, thermal radiation as well as with squeezing parameter.

Data are also computed for both Nusselt number and Skin friction. It can be concluded that for the system with temperature-dependent viscosity, the skin friction coefficient increases for squeezing parameter as well as for the magnetic parameter. The magnitude of micro-rotation and variable viscosity parameters is observed to decrease the Skin friction near the walls. The heat transfer rate decline with radiation parameter while it increases for squeezing parameter.

Proceeding three chapters four, five and six represents the boundary layer flow of nanofluids over a curvilinear surface. The graphical and numerical data obtained in case of fluid injection through boundary and stretching of solid surface with certain velocity evidently concluded a rise in the magnitude of both velocity and temperature distribution across the boundary layer with ascending values of carbon nanotubes volume fraction and magnetic parameters. The temperature distribution decreases while the linear momentum profile increases for the rising magnitude of temperature-dependent viscosity parameter and dimensionless curvature parameter. Also for the same case of stretching velocity the skin friction near the solid surface increase with variable viscosity parameter whereas it decreases for curvature parameter. In the case of shrinking surface and suction of fluid through the solid wall, the problem is found to possess dual solutions. These two distinguished solutions are named as upper and lower solution branches. Some previous studies suggested that of these two solutions, only the upper solution can be regarded as a stable solution. Graphical and numerical results are executed for the said case keeping the viscosity of the nanofluid temperature-dependent. In the case of a shrinking surface, it is perceived that for both types of solution, the skin fraction increases by raising the magnitude of the viscosity parameter. It is also sound that the temperature of the fluid falls with the increasing values of the suction parameter while it augments for the viscosity parameter, curvature parameter, and the carbon nanotubes volume fractions parameter. The critical values are the points where the two solutions coincide. Graphical results of skin friction coefficient versus shrinking and suction parameter depict that these critical points achieved soon for smaller values of suction parameter and magnitude of the shrinking parameter.

Chapter six provides an extensive review of flow over the curvilinear surface with micro-rotation and spin motions. These reevaluation efforts are commendable enough to classify the enhancement in heat transfer and thermal conductivity of micropolar fluid with nanoparticle conductive properties. Dynamic viscosity is supposed to be an inverse function of fluid temperature. It is concluded that with variable dynamic viscosity, the velocity distribution of the fluid increases with the magnetic parameter, whereas an increase in the magnitude of variable viscosity parameter resists the fluid flow. Within the proposed circumstances of temperature-dependent viscosities, the magnitude of Skin friction drops with rising values of the micropolar parameter while it rises with the increasing magnitude of the curvature parameter. Also, The results show that when using single-walled carbon nanotubes, the heat transfer coefficient is improved in contrast to multi-walled nanotubes. The employed method comparison is revealed with already available results for the authentication of our technique.

References

- [1] S.U.S. Choi, J.A. Eastman, Enhancing thermal conductivity of fluids with nanoparticles, Argonne National Lab., IL (United States), 1995.
- [2] S.S. Ghadikolaie, K. Hosseinzadeh, M. Hatami, D.D. Ganji, MHD boundary layer analysis for micropolar dusty fluid containing Hybrid nanoparticles (Cu-Al₂O₃) over a porous medium, *J. Mol. Liq.* 268 (2018) 813–823.
- [3] S. Nadeem, N. Abbas, On both MHD and slip effect in Micropolar Hybrid nanofluid past a circular cylinder under stagnation point region, *Can. J. Phys.* (2018).
- [4] S.Z. Alamri, R. Ellahi, N. Shehzad, A. Zeeshan, Convective radiative plane Poiseuille flow of nanofluid through porous medium with slip: an application of Stefan blowing, *J. Mol. Liq.* 273 (2019) 292–304.
- [5] M. Hassan, M. Marin, A. Alsharif, R. Ellahi, Convective heat transfer flow of nanofluid in a porous medium over wavy surface, *Phys. Lett. A.* 382 (2018) 2749–2753.
- [6] A. Malvandi, S. Heysiattalab, A. Ghasemi, D.D. Ganji, I. Pop, Nanoparticle migration effects at film boiling of nanofluids over a vertical plate, *Int. J. Numer. Methods Heat Fluid Flow.* 27 (2017) 471–485.
- [7] S. Nadeem, S. Ijaz, Impulsion of nanoparticles as a drug carrier for the theoretical investigation of stenosed arteries with induced magnetic effects, *J. Magn. Magn. Mater.* 410 (2016) 230–241.
- [8] M. Sheikholeslami, Influence of magnetic field on Al₂O₃-H₂O nanofluid forced convection heat transfer in a porous lid driven cavity with hot sphere obstacle by means of LBM, *J. Mol. Liq.* (2018).
- [9] M. Sheikholeslami, M. Shamlooei, Fe₃O₄-H₂O nanofluid natural convection in presence of thermal radiation, *Int. J. Hydrogen Energy.* 42 (2017) 5708–5718.
- [10] T. Sheikhalipour, A. Abbassi, Numerical analysis of nanofluid flow inside a trapezoidal microchannel using different approaches, *Adv. Powder Technol.* (2018).
- [11] S. Nadeem, S. Ahmad, N. Muhammad, Computational study of Falkner-Skan problem for

- a static and moving wedge, *Sensors Actuators B Chem.* 263 (2018) 69–76.
- [12] T. Chakraborty, K. Das, P.K. Kundu, Framing the impact of external magnetic field on bioconvection of a nanofluid flow containing gyrotactic microorganisms with convective boundary conditions, *Alexandria Eng. J.* (2016).
- [13] H.D. Koca, S. Doganay, A. Turgut, I.H. Tavman, R. Saidur, I.M. Mahbubul, Effect of particle size on the viscosity of nanofluids: A review, *Renew. Sustain. Energy Rev.* (2017).
- [14] G. Diglio, C. Roselli, M. Sasso, U.J. Channabasappa, Borehole heat exchanger with nanofluids as heat carrier, *Geothermics.* 72 (2018) 112–123.
- [15] A. Bianco, K. Kostarelos, M. Prato, Applications of carbon nanotubes in drug delivery, *Curr. Opin. Chem. Biol.* 9 (2005) 674–679.
- [16] R. Li, R. Wu, L. Zhao, Z. Hu, S. Guo, X. Pan, H. Zou, Folate and iron difunctionalized multiwall carbon nanotubes as dual-targeted drug nanocarrier to cancer cells, *Carbon N. Y.* 49 (2011) 1797–1805.
- [17] S. Nadeem, A.U. Khan, S.T. Hussain, Model based study of SWCNT and MWCNT thermal conductivities effect on the heat transfer due to the oscillating wall conditions, *Int. J. Hydrogen Energy.* 42 (2017) 28945–28957.
- [18] N.S. Akbar, Z.H. Khan, Variable fluid properties analysis with water based CNT nanofluid over a sensor sheet: numerical solution, *J. Mol. Liq.* 232 (2017) 471–477.
- [19] S.T. Hussain, Z.H. Khan, S. Nadeem, Water driven flow of carbon nanotubes in a rotating channel, *J. Mol. Liq.* 214 (2016) 136–144.
- [20] I. Shahzadi, S. Nadeem, F. Rabiei, Simultaneous effects of single wall carbon nanotube and effective variable viscosity for peristaltic flow through annulus having permeable walls, *Results Phys.* 7 (2017) 667–676.
- [21] A.C. Eringen, Theory of thermomicrofluids, *J. Math. Anal. Appl.* 38 (1972) 480–496.
- [22] G. Lukaszewicz, *Micropolar fluids: theory and applications*, Springer Science & Business Media, 1999.

- [23] N. Abbas, S. Saleem, S. Nadeem, A.A. Alderremy, A.U. Khan, On stagnation point flow of a micro polar nanofluid past a circular cylinder with velocity and thermal slip, *Results Phys.* 9 (2018) 1224–1232.
- [24] M.S. Shadloo, A. Kimiaefar, D. Bagheri, Series solution for heat transfer of continuous stretching sheet immersed in a micropolar fluid in the existence of radiation, *Int. J. Numer. Methods Heat Fluid Flow.* 23 (2013) 289–304.
- [25] M. Subhani, S. Nadeem, Numerical analysis of 3D micropolar nanofluid flow induced by an exponentially stretching surface embedded in a porous medium, *Eur. Phys. J. Plus.* 132 (2017) 441.
- [26] N.S. Akbar, D. Tripathi, Z.H. Khan, O.A. Bég, Mathematical modelling of pressure-driven micropolar biological flow due to metachronal wave propulsion of beating cilia, *Math. Biosci.* 301 (2018) 121–128.
- [27] Y. Ma, R. Mohebbi, M.M. Rashidi, Z. Yang, M.A. Sheremet, Numerical study of MHD nanofluid natural convection in a baffled U-shaped enclosure, *Int. J. Heat Mass Transf.* 130 (2019) 123–134.
- [28] R.U. Haq, F.A. Soomro, T. Mekkaoui, Q.M. Al-Mdallal, MHD natural convection flow enclosure in a corrugated cavity filled with a porous medium, *Int. J. Heat Mass Transf.* 121 (2018) 1168–1178.
- [29] M. Rashidi, M. Bhatti, M. Abbas, M. Ali, Entropy generation on MHD blood flow of nanofluid due to peristaltic waves, *Entropy.* 18 (2016) 117.
- [30] R. Ellahi, The effects of MHD and temperature dependent viscosity on the flow of non-Newtonian nanofluid in a pipe: analytical solutions, *Appl. Math. Model.* 37 (2013) 1451–1467.
- [31] S. Xun, J. Zhao, L. Zheng, X. Zhang, Bioconvection in rotating system immersed in nanofluid with temperature dependent viscosity and thermal conductivity, *Int. J. Heat Mass Transf.* 111 (2017) 1001–1006.
- [32] P.B. Kharat, S.B. Somvanshi, J.S. Kounsalye, S.S. Deshmukh, P.P. Khirade, K.M. Jadhav, Temperature dependent viscosity of cobalt ferrite/ethylene glycol ferrofluids, in: *AIP*

- Conf. Proc., AIP Publishing, 2018: p. 50044.
- [33] M.J. Babu, N. Sandeep, M.E. Ali, A.O. Nuhait, Magnetohydrodynamic dissipative flow across the slendering stretching sheet with temperature dependent variable viscosity, *Results Phys.* 7 (2017) 1801–1807.
- [34] M.G. Sobamowo, A.T. Akinshilo, Analysis of flow, heat transfer and entropy generation in a pipe conveying fourth grade fluid with temperature dependent viscosities and internal heat generation, *J. Mol. Liq.* 241 (2017) 188–198.
- [35] Q.Z. Xue, Model for the effective thermal conductivity of carbon nanotube composites, *Nanotechnology.* 17 (2006) 1655.
- [36] Z. Ahmed, S. Nadeem, Flow of a Micropolar CNT based nanofluid across a squeezing channel, *Phys. Scr.* (2019).
- [37] S. Nadeem, Z. Ahmed, S. Saleem, Carbon nanotubes effects in magneto nanofluid flow over a curved stretching surface with variable viscosity, *Microsyst. Technol.* (n.d.) 1–8.
- [38] A. Zahid, Numerical study of unsteady flow and heat transfer CNT-based MHD nanofluid with variable viscosity over a permeable shrinking surface, *Int. J. Numer. Methods Heat & Fluid Flow.* ahead-of-print (2019). doi:10.1108/HFF-04-2019-0346.
- [39] Z. Ahmed, A. Al-Qahtani, S. Nadeem, S. Saleem, Computational Study of MHD Nanofluid Flow Possessing Micro-Rotational Inertia over a Curved Surface with Variable Thermophysical Properties, *Processes.* 7 (2019) 387.
- [40] C.Y. Wang, The squeezing of a fluid between two plates, *J. Appl. Mech.* 43 (1976) 579–583.
- [41] N.C. Roşca, I. Pop, Unsteady boundary layer flow over a permeable curved stretching/shrinking surface, *Eur. J. Mech.* 51 (2015) 61–67.